POLITECNICO DI MILANO

Scuola di Ingegneria Industriale e dell'Informazione

Corso di Laurea Magistrale in Ingegneria Elettrica

Optimization of Solid-state Sub-nanosecond Pulse Generator for Repetitive Ultra-wideband Electromagnetic Radiation

Relatore: Prof. Flavia Grassi

Tesi di Laurea Magistrale di:
Mingxiang Gao
Matr. 876507

Anno Accademico 2018-2019

INDICE

INDICE DELLE FIGURE

ABSTRACT

Abstract in Italian

I campi elettromagnetici a banda ultra larga (in inglese ultra-wideband, UWB) sono largamente utilizzati in diversi campi applicativi dalla compatibilità elettromagnetica, al bio-elettromagnetismo, al rilevamento tramite radar, alla comunicazione wireless ed altri, per via dei vantaggi apportati dall'ampia banda passante, dal veloce tempo di salita e dalla breve durata dell'impulso. Nell'ambito degli studi relativi alle interferenze elettromagnetiche (EMI) intenzionali, i campi elettromagnetici UWB possono essere efficacemente applicati a dispositivi elettronici di comunicazione, per causare degli effetti dovuti alle EMI specialmente quando la frequenza di ripetizione degli impulso è elevata. In questa ricerca, sono presentate nuove tecniche per l'ottimizzazione del funzionamento di un generatore di impulsi allo stato solido, *solid-state sub-nanosecond pulse generator (SNPG)*. In particolare, al fine di investigare gli effetti delle EMI in sistemi di comunicazione wireless, l'attività qui documentata riguarda anche lo studio e realizzazione di radiatori elettromagnetici a UWB.

La prima parte dell'analisi è dedicata allo studio del *travelling-wave Marx circuit* con linee di trasmissione intermedie, al fine di migliorare le prestazioni dello *SNPG* con transistor. Dai risultati delle simulazioni si evince che i principali fattori che influenzano la forma d'onda dell'impulso sono il tempo di ritardo e l'impedenza delle linee di trasmissioni intermedie. Nel dominio della frequenza, la struttura del circuito stampato (printed circuit board, PCB) del sistema Marx può essere semplificata seguendo una geometria simile a quella di un filtro microstrip passa-basso con impedenza a gradini. Il comportamento del circuito Marx di tipo filtro passa-basso è stato approfondito mediante esperimenti in laboratorio e simulazioni elettromagnetiche *full-wave*, al fine di ottimizzare la struttura del PCB mediante la selezione delle configurazioni topologiche adatte a fornire i migliori parametri in uscita dal generatore di impulsi. Partendo dal modello del *travelling-wave Marx circuit*, è stata analizzata la connessione in serie di più moduli del circuito Marx, configurazione che consente di modificare a piacere l'ampiezza dell'impulso e la struttura circuitale. Nella progettazione di un generatore d'impulsi ad alta frequenza di ripetizione,

al fine di garantire l'adattamento di impedenza del *Marx circuit*, la dissipazione del calore è garantita tramite un'ottimizzazione della struttura del dissipatore metallico e l'introduzione di un dissipatore non metallico posto al di sopra delle linee microstrip. Il prototipo di generatore d'impulso garantisce una tensione pari a 1.1 kV, tempo di salita di 160 ps e massima frequenza di ripetizione di 300 kHz durante la modalità stabile, e di 600 kHz durante la modalità burst.

Nella seconda parte del lavoro viene studiato un radiatore elettromagnetico portatile a UWB costituito da un *SNPG* con transistor, caratterizzato da una potenza massima pari a 1.4 MW, un tempo di salita inferiore a 150 ps ed una frequenza di ripetizione di 50 kHz. Al fine di generare degli impulsi di grande intensità, è utilizzato un circuito Marx a 100 stadi con degli anelli di ferrite isolati per poter ottenere sia impulsi con ampiezza maggiore sia tempi di ricarica più rapidi. La connessione in parallelo dei transistor permette di aumentare sia la corrente di picco per la generazione di impulsi sia la capacità di potenza per la generazione di impulsi ripetitivi. In seguito, è proposto un modello che mette in parallelo dei moduli composti da un transistor e una capacità, in quanto questa soluzione è in grado di distribuire equamente la corrente lungo i vari rami. Al fine di irradiare impulsi elettromagnetici UWB in modo direzionale, un sistema compatto di antenne è stato fabbricato e connesso con un generatore di impulsi attraverso un modulo di alimentazione coassiale. Questo ha consentito la generazione di impulsi elettromagnetici UWB di ampiezza fino a 10.5 kV con un intervallo di banda (-10 dB) tra i 173 MHz fino ai 2.32 GHz, e massima frequenza di ripetizione 50 kHz.

Infine, sono state effettuate delle prove sperimentali sugli effetti delle EMI dei sistemi di comunicazione wireless che fanno uso di radiatori elettromagnetici UWB, all'interno di ambienti con campi elettromagnetici ripetitivi a UWB. Il setup dei dispositivi prevede un sistema di comunicazione wireless che lavora a 915 MHz e che è immerso in radiazioni elettromagnetiche UWB. Le prove sperimentali sulle interferenze elettromagnetiche sono state condotte con tempo di irraggiamento e numero di impulsi fissati. I risultati degli esperimenti condotti stabiliscono che l'effetto dell'accumulo di energia può essere causato dall'aumento della frequenza di ripetitività degli impulsi, che può indurre, a sua volta, un aumento degli effetti delle EMI, come la mancata trasmissione di dati o l'interruzione della comunicazione.

Abstract in English

Ultra-wideband (UWB) electromagnetic environment is widely used in electromagnetic compatibility, biological electromagnetics, radar detection, wireless communication and other fields, due to the advantages of wide bandwidth, short rise time, and pulse duration. In the study of intentional electromagnetic interference (EMI), the UWB electromagnetic environment is efficient to couple with electronic communication equipment, which may cause EMI effects, especially for high pulse repetition rate. To meet the requirements of experimental research, new techniques are proposed to optimize the solid-state sub-nanosecond pulse generator, and the UWB electromagnetic radiators are developed for the experimental study on EMI effects with the wireless communication system.

Firstly, to improve the performance of the transistor-based sub-nanosecond pulse generator, the traveling-wave Marx circuit with inter-stage transmission lines is studied. Circuit simulation results indicate that the delay time and the impedance of inter-stage transmission lines are the main influencing factors of the pulse waveform. In the frequency domain, the printed circuit board (PCB) structure of Marx circuit can be simplified as a low-pass microstrip filter of the similar geometry with stepped impedance. Through simulations with PCB circuit model, the low-pass filtering effect of this type of Marx circuit is analyzed, which can be used to optimize PCB structure with suitable circuit configuration for better output parameters of the pulse generator. Based on the traveling-wave Marx circuit model, the series connection of modularized Marx circuits is proposed, which has the advantages of adjustable amplitude and bendable circuit layout. In the high-repetition-rate pulse generator design, to realize the impedance matching in the traveling-wave Marx circuit, an heat dissipation design is proposed through optimizing the layout of the metallic sinks and introduction of non-metallic heat-conducting sinks above the microstrip lines. A prototype of a pulse generator is developed with the maximum repetition rate of 300 kHz in stable mode and 600 kHz in burst mode, the amplitude of 1.1 kV and the rise time of 160 ps.

Secondly, a portable UWB electromagnetic radiator is developed based on a transistor-based sub-nanosecond pulse generator with the peak power of 1.4 MW, the rise time less than 150 ps, and the repetition rate of 50 kHz. In order to generate high-amplitude pulses, a 100-stage Marx circuit with isolation ferrite beads is proposed for both higher pulse

amplitude and faster charging rate. The parallel connection of transistors could increase the peak current for pulse forming and the power capacity for repetitive pulse generation. An effective sharing-current design of paralleled “transistor-capacitor unit” is proposed with uniform current distribution among the paralleled transistors. In order to directionally radiate UWB electromagnetic pulse, a compact combined antenna array is fabricated and connected with the pulse generator via a coaxial feeding module. The effective potential of the UWB electromagnetic radiator reaches 10.5 kV with the band range (-10 dB) from 173 MHz to 2.32 GHz, and its maximum pulse repetition rate is up to 50 kHz also.

Finally, based on the developed UWB electromagnetic radiator, the experimental study on the EMI effects of the wireless communication system is carried out in the repetitive UWB electromagnetic environment. In the experimental setup, a wireless communication system operating at 915 MHz is introduced in the UWB electromagnetic radiation environment. In the experimental procedure, the EMI experiments are carried out under the conditions of fixed radiation time and fixed pulse number, respectively. Finally, the experimental results suggest that the energy accumulation effect can be determined by increasing pulse repetition rate, which can increase the probability of EMI effect, e.g. data missing and communication interruption.

1 INTRODUCTION

1.1 Research Background

With the development of electromagnetic environment research, ultra-wideband (UWB) electromagnetic pulse with higher peak power and wider bandwidth has been paid more and more attention from the 1980s. Generally, typical artificial electromagnetic environment can be divided into several types according to spectral distributions, such as narrowband, wideband, and ultra-wideband, etc. [1-7], as shown in Figure 1. Since there is no clear boundary between wideband and UWB, the UWB electromagnetic environment has multiple definitions: UWB defined by the Federal Communications Commission (FCC) is the percentage bandwidth (PBW) greater than 25% or the total bandwidth exceeding 1.5 GHz; in the field of high-power electromagnetics, UWB electromagnetic environment is commonly defined as PBW>163.4% or the bandwidth ratio (BR) greater than 10.

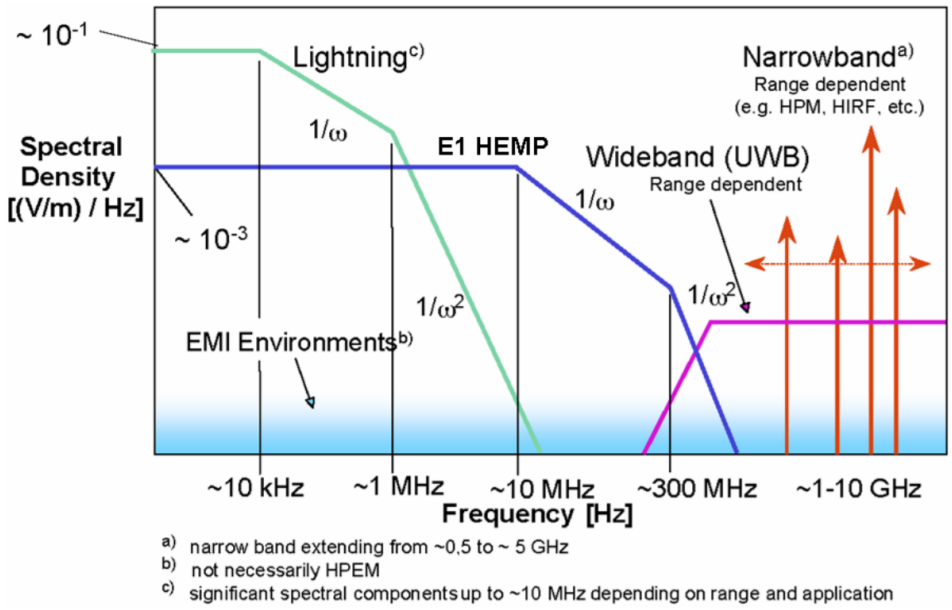

Figure 1. Spectrum of typical artificial electromagnetic environments[6].

Despite the different definitions, UWB electromagnetic environment, as a fast transient electromagnetic environment, has the following characteristics compared with the

continuous wave electromagnetic environment. In the time domain, UWB electromagnetic environment behaves as an UWB electromagnetic pulse with the pulse rise time and duration time in the order of nanosecond or even sub-nanosecond. In the frequency domain, UWB electromagnetic environment has wide spectrum range and flat distribution, and the upper limit frequency can reach the order of GHz. Due to these excellent characteristics, UWB electromagnetic environment is widely used in electromagnetic compatibility (EMC), biological electromagnetics, pulse radar, time domain measurement, UWB communication and other fields[8-19]. According to the difference in peak power and applications, the communication based on UWB signals is called UWB technology in a narrow sense, and the UWB electromagnetic environment research with high peak power is usually called high-power UWB electromagnetic pulse technology, which is also the research topic in this thesis.

In the study of EMC, high-power UWB electromagnetic environment can interfere with electronic communication devices operating at different frequencies due to the characters of high peak power and wide bandwidth. On the one hand, high-power UWB electromagnetic pulse technology can carry out non-contact strikes on targets in applications, such as non-contact forced landing of drones and forced stop of vehicles. On the other hand, once high-power UWB electromagnetic pulses are used by criminals, the radiation sources using this technology may pose a threat to the safe operation of the infrastructure. Therefore, it is necessary to study the electromagnetic interference (EMI) effect caused by UWB electromagnetic environment and its protection technology. With this background, the development of UWB electromagnetic radiators is required to set up the experimental platform for related research, such as the EMI effect mechanism caused by repetitive UWB electromagnetic radiation environment.

Due to the broad application prospects of the UWB electromagnetic environment, especially the research needs of its EMI effect, it is necessary to carry out research on the experimental simulation of UWB electromagnetic environment in laboratory. This will help to further explore the EMI effect mechanism caused by UWB electromagnetic environment, and promote the technological advancement of related applications.

1.2 Related Research Status

1.2.1 Research status of high-repetition-rate sub-nanosecond pulse generator

In order to establish UWB electromagnetic simulation environment for experimental research, the sub-nanosecond pulse generator is the most critical device. A sub-nanosecond pulse generator using the gas switches could produce sub-nanosecond pulse with high amplitude, but it is difficult to generate pulses with high pulse repetition rate due to the limitation of long switch recovery time. The solid-state pulse generator using the semiconductor switches has the characteristics of high pulse repetition rate, easy to control, and good waveform stability. The high-repetiton-rate sub-nanosecond pulse generators usually use the fast ionization dynistors (FID), the delayed breakdown diodes (DBD), and the avalanche transistors as the switching devices[20].

Among these devices, avalanche transistor is a commercial switching device commonly used in nanosecond or sub-nanosecond pulse generators. Due to its fast switching speed (above 15 kV/ns), high breakdown voltage (in the order of 100 V), strong peak current capability (in the order of 10 A), low jitter and easy control, avalanche transistor is an ideal switching device for medium or low power sub-nanosecond pulse generator [21-23]. Since the invention of bipolar transistors, many institutes and universities have carried out research on nanosecond or sub-nanosecond pulse generators based on the avalanche transistors, which have been widely used in ground penetrating radar, high-power electromagnetics, and etc.

Research on transistor-based pulse generators began in the 1980s. Some representative works are summarized as follows[24-29]. In 1981, J. Jethwa et al. developed a nanosecond pulse generator based on 11 transistor in series[24], with the pulse amplitude of 2 kV, the pulse rise time of 25 ns, and the repetition rate of 100 Hz. In 1990, R. J. Baker developed a nanosecond pulse generator by using transistors and the Marx circuit, in which the pulse amplitude is 2 kV and the rise time is approximately 1 ns[25]. In 1994, a 5-stage Marx circuit pulser was developed by V. N. Rai et al. with a 4 kV amplitude, 1 ns rise time and 1 kHz repetition rate[26]. In 2007, P. Krishnaswamy et al. designed a sub-nanosecond pulse generator by switching a chain of avalanche transistors configured as a tapered transmission line from high voltage to ground[27], as shown in Figure 2. The generator is capable of producing a 0.8 ns rise time, 1.3 ns wide, 1.1 kV pulse into a 50 Ω load at a maximum repetition rate of 200 kHz. In 2010, X. Yuan et al. developed a sub-nanosecond pulse generator using four Marx circuits connected in parallel[29], as shown in Figure 3,

which could generate pulses with the rise time of less than 200 ps, the pulse amplitude of 4.5 kV, and the repetition rate of 30 kHz.

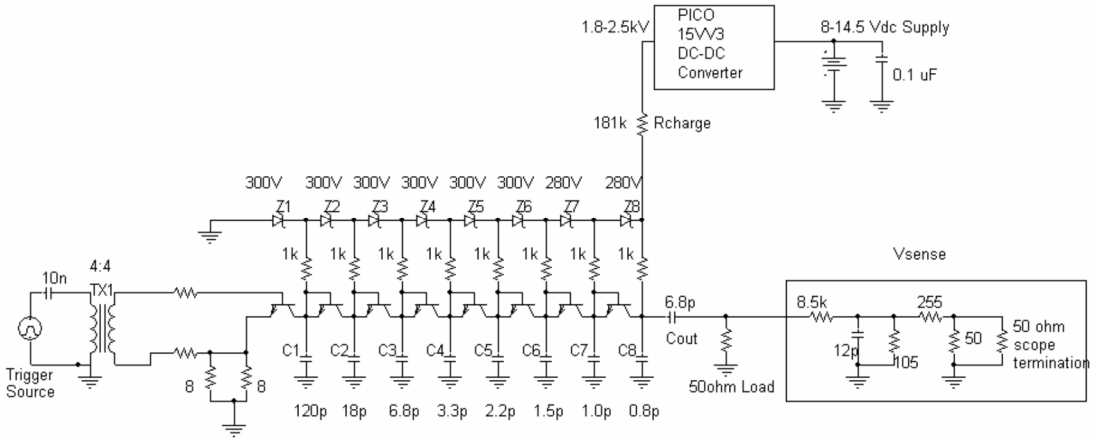

Figure 2. Pulse generator circuit with a chain of transistors configured as a tapered transmission line[27].

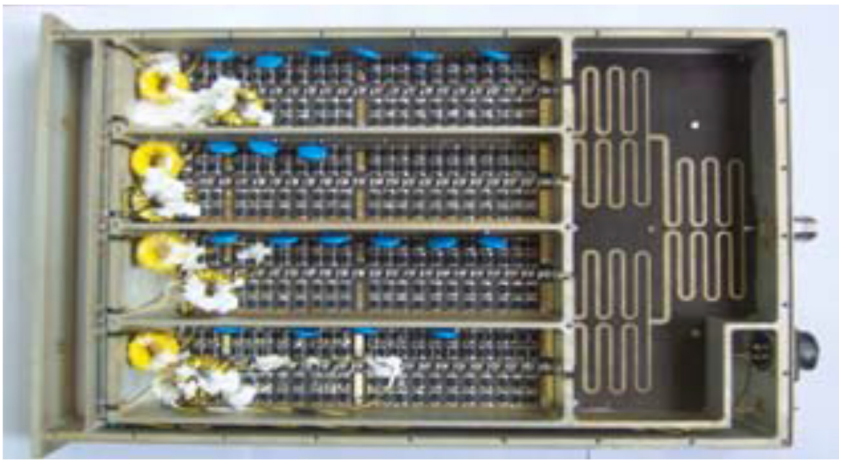

Figure 3. Photo of sub-nanosecond pulse generator with four Marx circuits connected in parallel[29].

In recent years, research on transistor-based sub-nanosecond pulse generator mainly aims to improve the pulse amplitude and reduce the pulse rise time. The commonly used technical methods include adjusting the connection mode of transistors and applying power synthesis of multiple circuit modules. There are still some problems in the current research: the analysis of the pulse generator working process, especially the pulse forming process is not deep enough; the pulse repetition rate need to be further improved according to related applications, while there are few studies on the pulse repetition rate characteristic of such pulse generators; the commonly used power synthesis design can improve the pulse amplitude, but this method has the disadvantages of difficult synchronization of pulse generator and low circuit efficiency.

1.2.2 Research status of UWB electromagnetic radiator and its EMI effects

The UWB electromagnetic radiator is commonly composed of the sub-nanosecond pulse generator, the UWB radiating antenna (or antenna array) and related power feeding modules, which can be used for directional radiation of UWB electromagnetic pulses and simulation of UWB electromagnetic environment. In the field of high-power electromagneticsy, the electromagnetic environment with the peak electric field strength of more than 100 V/m is called the high-power electromagnetic environment.

The development of UWB electromagnetic radiator is the key technology in high-power UWB electromagnetic pulse technology. Related research began in the late 1950s and was originally used for ground penetrating radar study. With the in-depth development of electromagnetic pulse technology, a series of electromagnetic pulse simulators and radiators have been developed[30, 31]. UWB electromagnetic pulses with short rise time, high peak power and excellent radiation characteristics have gradually become an important research branch in high-power electromagnetics research.

In recent decades, numerous research institutions have developed UWB electromagnetic radiators. Since the 1980s, research institutes in US have developed a series of high-power UWB electromagnetic radiators[32-34]. For example, the Phillips Laboratory has developed a series of “H” UWB electromagnetic radiators based on high-pressure hydrogen switches; the Air Force Research Laboratory has developed the “JOLT” UWB electromagnetic radiator with the far-field effective potential of 5.3 MV, in which the radiating antenna uses impulse radiating antennas (IRA) with the semi-parabolic reflector, as shown in Figure 4.

Figure 4. Photo of the “JOLT” UWB electromagnetic radiator[33].

Since the same period, research institutions in the Soviet Union have also developed multiple types of UWB electromagnetic radiators for high-power radiation[33-40]. Up to now, the Institute of High Current Electronics and the Institute of Electrophysics of the Russian Academy of Sciences have led the research work in this field. The Institute of High Current Electronics has developed a series of UWB electromagnetic radiators, which usually use the bipolar sub-nanosecond pulse generator based on gas switches and the combined antenna array for directional radiation. As shown in Figure 5, this type of UWB electromagnetic radiator has the pulse repetition rate of 100 Hz and the effective potential of 4.3 MV. The Institute of Electronphysics mainly focuses on the development of sub-nanosecond pulse generators, including the pulse compression techniques such as nonlinear transmission lines [52], which can produce sub-nanosecond pulses with amplitudes of several hundred kilovolts.

Figure 5. Photo of the UWB electromagnetic radiator with combined antenna array[40].

In addition, in recent years, a number of small or medium-sized UWB electromagnetic radiators have been developed in European countries. For example, research institutes in Switzerland, Netherlands and other countries have developed several medium-sized UWB electromagnetic radiators with IRA antennas[41, 42], with the effective potentials up to tens of kV and pulse repetition frequencies of hundreds Hz. In 2016, some French universities developed a portable high-repetition-rate UWB electromagnetic radiator based on the photoconductive semiconductor switches and the combined antenna[43]. The radiator structure and the radiation field waveform are shown in Figure 6, in which the effective

potential is about 3 kV and the maximum pulse repetition rate of 33 MHz with 20 pulses in total.

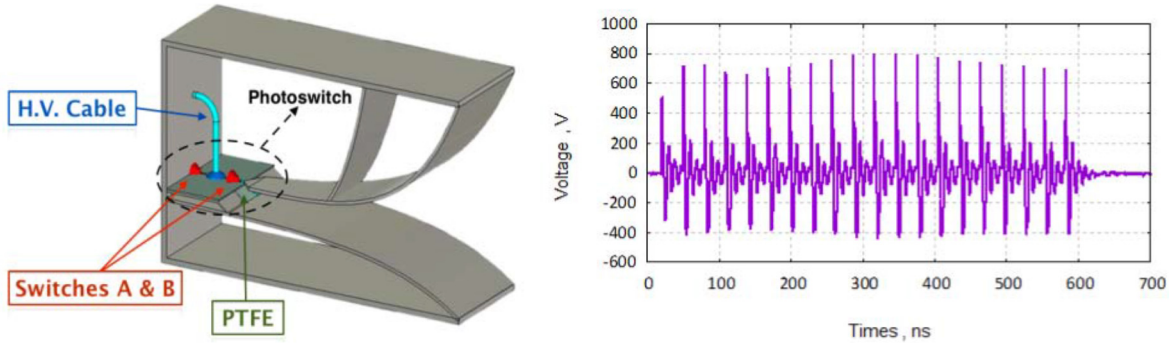

(a) (b)

Figure 6. (a) Diagram of the combined antenna with integrated photoswitches. (b) Output voltage from the integrated photoswitch antenna[43].

The early development of UWB electromagnetic radiators was mainly used as electromagnetic weapons. In order to generate high-power UWB electromagnetic pulses, it is necessary to develop high-power sub-nanosecond pulse generators and large-scale radiating antennas. In recent years, with the advancement of UWB electromagnetic environment in other fields such as EMC, biological electromagnetics, and etc., the design of UWB electromagnetic radiators tend to have the characteristics of high repetitive rate and compact size. Therefore, based on the design method of conventional high-power UWB electromagnetic radiators, the development of portable UWB electromagnetic radiator could meet the application requirements in EMC and other fields. In addition, with the advancement of solid-state pulse generator technology, the pulse repetition rate can be significantly improved. Based on this, the UWB electromagnetic pulses with higher pulse repetition rate can also be generated in novel radiators. For high-power UWB electromagnetic pulses, when the pulse repetition rate is greater than or equal to 1 kHz, it is usually called the high repetition rate pulses. Furthermore, when the pulse repetition rate is greater than or equal to 100 kHz, it can be called the ultra-high repetition rate pulses. For experimental study on EMI effects, the increase of the pulse repetition rate could not only enhance the probability of EMI effects in unit time, but also stimulate the interference effect phenomenon form data missing to continuous interruptions or even damages through the energy accumulation effect.

With the development of electromagnetic environment simulators (such as UWB electromagnetic radiator), related institutes have also studied the mechanism of EMI effects and its protection technology. In recent years, with the advancement of modern electronic communication technology, more and more electronic communication system or equipments equipped with electronic devices could be threatened by high-power electromagnetic environment. Considering that the mechanism of EMI effects may involve a variety of complex internal processes, e.g. communication error, electrical breakdown or thermal damage, etc., it is necessary to perform EMC tests under simulated electromagnetic environment conditions according to different equipments and electromagnetic environments. On this basis, the research mainly focuses on the classification of EMI effects according to experimental results, the analysis of the possible interference mechanisms of different effects, and the modeling of EMI effects mechanism combined with statistical analysis[44-47]. The analysis of the electromagnetic susceptibility of the EUT (equipment under test) in different electromagnetic environments can provide technical supports for the subsequent electromagnetic protection work like EMI protection.

1.3 Research Contents of this Thesis

In summary, UWB electromagnetic environment has important research significance in EMI, bioelectromagnetics and other related fields. Under this background, this thesis mainly focus on the optimization of sub-nanosecond solid-state pulse generator, and its application in UWB electromagnetic radiator for EMI effects. The thesis consists of six chapters. In this chapter, the relevant research background, research status and main contents of this thesis are introduced. For the other chapters, their main contents are summarized as follows.

In chapter 2, the principles of transistor-based sub-nanosecond pulse generator are introduced in detail, including the avalanche breakdown mechanisms in transistors, the principle of Marx circuit for high amplitude pulse generation, the design technique of microwave circuit for sub-nanosecond pulse generation and several sub-nanosecond pulse shaping methods.

In chapter 3, the inter-stage transmission lines are introduced into the Marx circuit to simulate the traveling-wave phenomenon in the sub-nanosecond pulse froming process, which is called the traveling-wave Marx circuit. The microstrip filter effect caused by

inter-stage transmission lines is analyzed in simulation and measurement. And several applications of the traveling-wave Marx circuit is proposed for better performance, such as short pulse rise time, compact circuit layout, and circuit heat dissipation.

In chapter 4, the UWB electromagnetic radiator based on high-amplitude sub-nanosecond pulse generator is developed, in which several new techniques are proposed for high pulse amplitude. According to the design theory of combined antenna array for high power UWB electromagnetic radiation, a compact UWB electromagnetic radiator with a 2×2 combined antenna array is developed. Finally, a prototype of compact UWB electromagnetic radiator is fabricated and tested.

In chapter 5, by using the UWB electromagnetic radiator, the EMI effects caused by repetitive UWB radiation is studied in experiments. The experimental setup includes the UWB electromagnetic radiators, a wireless communication system operating at 915 MHz, and a logic analyzer for data recording. In order to analyze the EMI effects caused by high pulse repetition rate, two experiments are carried out with fixed radiation time and fixed pulse number.

Chapter 6 summarizes the main research conlusions of this work. The bibliography and related publications are listed at the end of this thesis.

2 PRINCIPLES OF SUB-NANOSECOND PULSE GENERATOR BASED ON TRANSISTOR

This chapter mainly introduces the working principles of the sub-nanosecond solid-state pulse generator based on avalanche transistor, which will help to understand the working process of such kind of pulse generator and introduce optimization studies in subsequent chapters.

2.1 Avalanche Breakdown in Transistor

Transistor is a commonly used semiconductor device used to control current and amplify small signals[48-50]. When the base current is negative (I_B<0), an NPN type bipolar transistor enters the cut-off region with its base-emitter junction reversed. If the collector voltage continues to increase, the transistor will turn into the avalanche region. The test circuit used to analyze the single transistor avalanche breakdown process is shown in Figure 7. The positive voltage +E_c is used to provide the bias voltage U_{CE} which is closed to V_{CBO}, so the transistor can keep in a critical avalanche state. The negative voltage -E_b is used to establish the reverse bias voltage of the base-emitter junction during the steady-state.

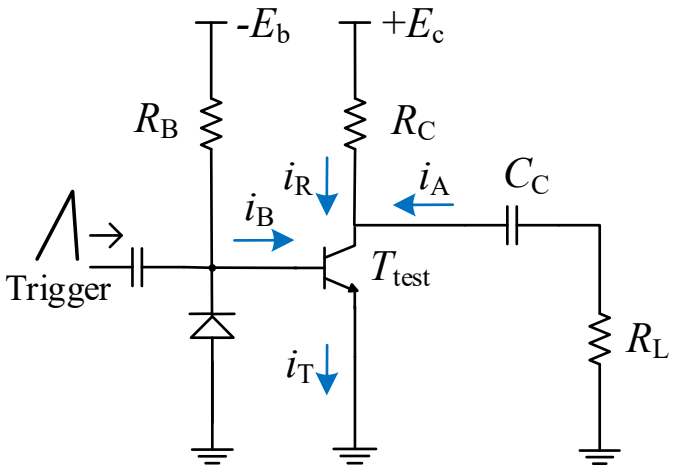

Figure 7. The test circuit used to analyze the single transistor avalanche breakdown process.

When the circuit is in a stable state, the transistor in the off state can be regarded as a circuit node. Then, the following set of equations can be obtained

$$\begin{cases} i_{\mathrm{T}} = i_{\mathrm{R}} + i_{\mathrm{A}} + i_{\mathrm{B}} \\ i_{\mathrm{B}} \cong 0 \\ U_{\mathrm{CE}} = E_{\mathrm{c}} - i_{\mathrm{R}} \cdot R_{\mathrm{C}} \\ U_{\mathrm{CE}} = U_{\mathrm{C}}(0) - \dfrac{1}{C_{\mathrm{p}}} \int_0^{t_{\mathrm{A}}} i_{\mathrm{A}} dt - i_{\mathrm{A}} \cdot R_{\mathrm{L}} \end{cases} \tag{2.1}$$

In the equations above, $U_{\mathrm{C}}(0)$ is the charging voltage for capacitor C_{C} in the beginning of the avalanche breakdown. t_{A} is the time to complete the avalanche discharge process. When the circuit is static, we can get that

$$i_{\mathrm{A}} = i_{\mathrm{B}} = 0 \tag{2.2}$$

Thus, the transistor collector current I_{C} meets that

$$I_{\mathrm{C}} = i_{\mathrm{T}} = i_{\mathrm{R}} = \frac{E_{\mathrm{c}} - U_{\mathrm{CE}}}{R_{\mathrm{C}}} \tag{2.3}$$

The formula (2.3) is the load line function of the transistor under static conditions, and the load line is marked as I. When the circuit is in a dynamic avalanche breakdown process, it satisfies

$$U_{\mathrm{CE}} = U_{\mathrm{C}}(0) - \frac{1}{C_{\mathrm{p}}} \int_0^{t_{\mathrm{A}}} \left(i_{\mathrm{T}} + \frac{U_{\mathrm{CE}} - E_{\mathrm{c}}}{R_{\mathrm{C}}} \right) dt - \left(i_{\mathrm{T}} + \frac{U_{\mathrm{CE}} - E_{\mathrm{c}}}{R_{\mathrm{C}}} \right) \cdot R_{\mathrm{L}} \tag{2.4}$$

Considering

$$i_{\mathrm{T}} >> \frac{E_{\mathrm{c}} - U_{\mathrm{CE}}}{R_{\mathrm{C}}} = i_{\mathrm{R}} \tag{2.5}$$

Therefore, the transistor collector current I_{C} satisfies

$$I_{\mathrm{C}} = i_{\mathrm{T}} \approx i_{\mathrm{A}} \tag{2.6}$$

$$U_{\mathrm{CE}} \approx U_{\mathrm{C}}(0) - \frac{1}{C_{\mathrm{p}}} \int_0^{t_{\mathrm{A}}} i_{\mathrm{T}} dt - i_{\mathrm{T}} \cdot R_{\mathrm{L}} = U_{\mathrm{C}}(0) - \frac{1}{C_{\mathrm{p}}} \int_0^{t_{\mathrm{A}}} I_{\mathrm{C}} dt - I_{\mathrm{C}} \cdot R_{\mathrm{L}} \tag{2.7}$$

$$I_C \approx \frac{U_C(0) - \frac{1}{C_p}\int_0^{t_A} I_C dt - U_{CE}}{R_L} \tag{2.8}$$

The above equation (2.8) is the approximate load line function of a triode under dynamic conditions. It can be further simplified neglecting of capacitive voltage drop during avalanche process t_A

$$I_C \approx \frac{U_C(0) - U_{CE}}{R_L} \tag{2.9}$$

Obviously, this load line function represents the extreme condition of avalanche effect, and its corresponding load line is marked as II.

The working state of the transistor in the avalanche breakdown process can be described by the U_{CE}-I_C characteristic curves, as shown in Figure 8. Different base injection currents I_B correspond to different characteristic curves.

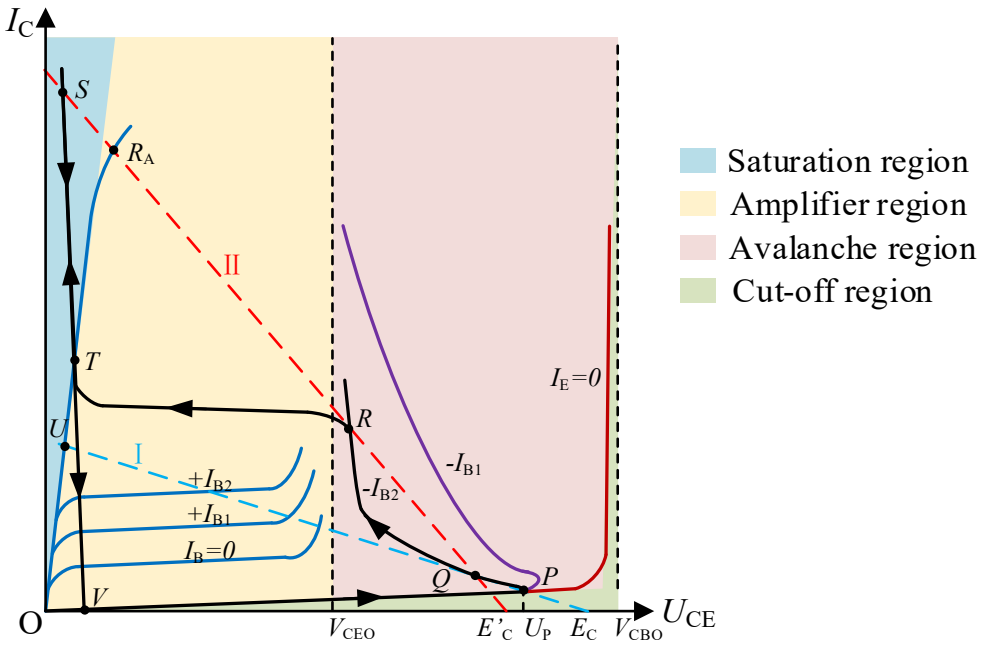

Figure 8. The characteristic curve of avalanche breakdown process in the NPN type bipolar transistor.

When the base emitter is reverse offset and the base maintains the reverse injection current -I_{B1}, the transistor is in a static condition. The working point P, the intersection of the load line I and characteristic curve -I_{B1} in the positive resistance region, is the steady-state point

with maximum U_{CE}. If the U_{CE} is further increased, the transistor will enter the negative resistance zone along the characteristic curve $-I_{B1}$, which is called the overvoltage trigger.

Another accurate avalanche triggering mode is the base trigger. When the base is injected with a positive trigger signal, the base injection current $-I_{B1}$ will change to $-I_{B2}$ ($I_{B1}>I_{B2}$). Since then, the working point reaches to an instability point Q through the load line I, which is in the negative resistance area of the characteristic curve $-I_{B2}$. The avalanche transistor begins to enter the avalanche working state and forms a strong positive feedback. The first avalanche breakdown process will end if the trigger signal is no longer injected at point R, which is the first intersection of the curve $-I_{B2}$ and the load line II.

If the reverse injection current is still kept as $-I_{B2}$, the avalanche transistor is likely to begin the secondary avalanche breakdown process. Some studies interpreted this as the collector current exceeding the maximum collector operating current I_H, which is the operating current at point R. During this process, the avalanche breakdown process will be further enhanced until point S. The total avalanche process from point Q to point S can be as short as sub-nanosecond. It is worth emphasizing that the transistor cannot shut down immediately because of residual charge in PN junction. During this period, the transistor can maintain the conduction mode. The closing process finally reaches the point V through the point T, and this process is much longer than the avalanche process. After the transistor completely shutting off, the external voltage $+E_c$ begins to charge the collector via the R_C, and the U_{CE} is gradually restored to U_P.

In the time domain, the avalanche breakdown process described above can be displayed by the t-U_{CE} curve, as shown in Figure 9. The main working points and working areas in this figure are consistent with the Figure 8. The avalanche breakdown process of the transistor is periodic and restorable used in the pulse formation. The complete period of this pulse forming process is called total avalanche process time, and this concept will be further discussed later.

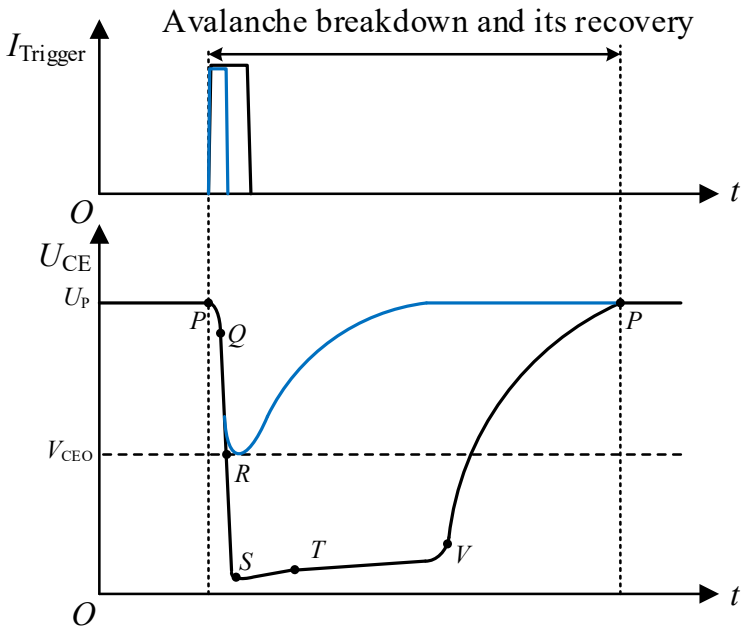

Figure 9. The dynamic curve of avalanche breakdown process for transistor in time domain.

2.2 Theory of Marx Circuit

Marx circuit, proposed by Erwin Marx in 1923, is the most popular pulse-generating circuit for generating pulse with short rise time and high amplitude[52]. According to different application requirements, specific topology of Marx circuit can be designed, such as number of circuit stage, topology of isolation circuit network, etc. Depending on the different applications, the rise time of the pulses generated by Marx circuits can range from microseconds to tens of nanoseconds or even picoseconds, and the circuit equivalent load may be capacitive, small resistive, large resistive, etc.

In order to generate pulses with high repetition rate, the parallel charging Marx circuit proposed by Carl E. Baum is widely used in application[51], as shown in Figure 10. In this circuit, parallel connection of isolation components is applied in each stage, with the advantage of fast charging rate compared to the traditional one. The main working process of the parallel charging Marx circuit can be described as following: firstly, during the charging process, capacitors are charged by the currents flowing along the blue lines. Then, during the pulse forming process, with the switches closed, all capacitors are connected in series and discharges energy into the load with current flowing along the yellow line. As a result, it is necessary to get a large enough discharge time constant between the isolation component and the charging capacitor compared to that of the main discharge circuit to

achieve good enough isolation characteristic of the generated pulse. The characteristic of parallel charging Marx circuit is that the charging time of all stages of capacitors is almost the same, but the isolation characteristic of the circuit is slightly worse than that of the traditional Marx circuit using the same resistors. Therefore, it is suitable for generating pulses with high pulse repletion rate but relatively lower amplitude. In this thesis, the sub-nanosecond pulse generator is mainly used for electromagnetic radiation, which means that its equivalent load R_L is usually 50 Ω.

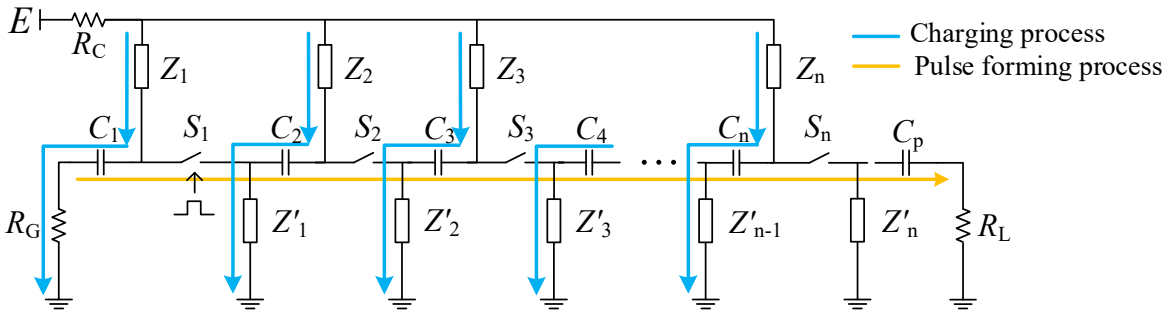

Figure 10. Typical circuit topology of parallel charging Marx circuit.

It should be noted that in general analysis, Marx circuit and its equivalent circuit are lumped parameter circuits. For most Marx circuits, they can be regarded as electrically small circuits. That is to say, the transmission length of the pulse rise time or the wavelength of the high-frequency component of the pulse is much longer than the physical length of the Marx circuit. Therefore, it is often believed that all capacitors are involved in the discharge process with the switches closed at the same time. The consistency of the switches' closing process is called synchronization in Marx circuit. The ideal Marx circuit often requires good enough synchronization of the switches, which can ensure continuous output pulse waveform and high output efficiency.

The Marx circuit with the transistors as the switch devices has the following features in practical design. On the one hand, for capacitor in each stage, although a large enough capacitor can ensure a higher pulse amplitude, an excessive capacitance will cause the increase of pulse width also. This will result in a reduction in transistor life due to its limited current capability and heat capacity. In order to generate a narrow pulse with sub-nanosecond rise time and high amplitude, an under-charge design is usually used in this kind of Marx circuit, that is, a relatively small capacitor value is selected in each stage. Although the contribution of each capacitor to the pulse amplitude is reduced, it can

effectively improve the stability of the pulse generator and contribute to the generation of narrow pulses with high pulse repetition rate. On the other hand, for most stable Marx circuit, the number of circuit stages is approximately proportional to the pulse amplitude. However, in order to generate high amplitude pulse, the stage number is required to be as large as possible. The increase of circuit stage number can cause several new problems, such as the maximum current limit of the single transistor, the circuit insulation for high amplitude pulse, and the synchronization requirement of the switches.

2.3 Design Methods of Microwave Circuit

Marx circuits using avalanche transistors as switching devices typically use printed circuit board (PCB) in the manufacturing process. Since the pulse rise time is only in the order of sub-nanosecond and the corresponding bandwidth of pulse is up to GHz, it is necessary to introduce the microwave circuit design method to improve the characteristics of the pulse generator[53], especially for optimizing key parameters like pulse rise time and pulse amplitude. In the design of the PCB of Marx circuit, design of microstrip line and selection of devices and materials are two main problems that need to be considered generally.

For transmission line structures on PCBs of microwave circuit, microstrip lines or strip lines are always applied for impedance matching and continuity in signal transmission process. In order to arrange the circuit configuration in a limited space, Marx circuits often use microstrip lines as transmission line structures on PCBs. In the microstrip line, a conductor strip with the width of w and the thickness of t is usually designed on the one side of the circuit dielectric substrate with the thickness of h and the relative dielectric constant of ε_r, and the other side of the circuit dielectric substrate is designed with a conductor ground plane. Assume that the thickness of the conductor strip of the conductor strip is approximately zero (i.e. t=0), and its characteristic impedance can be calculated as[89]

$$Z_c = \begin{cases} \dfrac{60}{\sqrt{\varepsilon_r'}} \ln\left(\dfrac{8h}{w} + \dfrac{w}{4h}\right), & \dfrac{w}{h} \le 1 \\ \dfrac{120\pi}{\sqrt{\varepsilon_r'}\left[\dfrac{w}{h} + 2.42 - 0.44\dfrac{h}{w} + \left(1 - \dfrac{h}{w}\right)^6\right]^{-1}}, & \dfrac{w}{h} \ge 1 \end{cases} \tag{2.10}$$

For this formula, the calculation accuracy is within ±0.25%. ε_r' is the effective relative dielectric constant used for simplifying the air and dielectric medium between the conductor strip and the conductor ground plane, which is equivalent to the same uniform medium with an effective relative dielectric constant as the medium. By calculating the equivalent distributed capacitance in microstrip line structure, we can get

$$\varepsilon_r' = \frac{\varepsilon_r + 1}{2} + \frac{\varepsilon_r - 1}{2} \frac{1}{\sqrt{1 + 10h/w}} \tag{2.11}$$

The selection of devices and materials in the PCB should meet the requirements form high frequency characteristics and transient high power characteristics in the high amplitude sub-nanosecond pulse forming process. For the generation and transmission of sub-nanosecond pulses, the circuit dielectric substrate should maintain stable electrical parameters in wide bandwidth. Under the condition that the pulse generator circuit meets the insulation requirements, the parameters of circuit dielectric substrate should help to reduce the influence of the distribution parameters, that is, reduce the unit length capacitance and the unit length inductance on the microstrip line in PCB. For the circuit devices in Marx circuit, the surface mounted device (SMD) components with high frequency characteristics should be selected as a priority on the premise of satisfying the high power (or sometimes high voltage) requirement, and their package size should be matched with the microstrip line in PCB as much as possible. In addition, for pulse generator operating with high pulse repetition rate, the devices and materials in the PCB should have the characteristics of large power capacity or good heat dissipation capability, which is suitable for introducing additional circuit heat dissipation design.

2.4 Techniques of Sub-nanosecond Pulse Shaping

For pulse generated by transistor-based sub-nanosecond pulse generator, its rise time can be less than 200 ps and its amplitude can up to several kilovolts. However, the operating characteristics of the Marx circuit determine that the generated pulses are always unipolar pulses. In practical application, it is necessary to adjust the generated pulse waveform, such as pulse dual polarization, pulse polarity reversal, etc., to meet the needs of electromagnetic radiation or other applications. Since the sub-nanosecond pulse has high requirements on the high-frequency characteristics of the Marx circuit, it is necessary to

pay attention to the wide-band characteristics of the circuit during the pulse shaping process to avoid distortion or attenuation phenomenon after pulse shaping. Several sub-nanosecond pulse shaping techniques for solid-state pulse generator will be briefly introduced in the following according to engineering experience.

2.4.1 Techniques for dual polarization of sub-nanosecond pulse

For applications such as UWB electromagnetic radiation, bipolar pulses have the characteristics of small low-frequency components and concentrated high-frequency components, which is an ideal excitation pulse waveform for radiating antenna. Commonly designed pulse generators can only generate unipolar pulses, so it is necessary to specifically design a dual polarization shaping circuit or a pulse synthesis circuit to convert unipolar pulses into bipolar pulses. For solid-state sub-nanosecond pulse generators, the commonly used pulsed dual polarization methods mainly include short-circuit line method and pulse synthesis method [90, 91].

2.4.1.1 Short-circuit line method

When the traveling wave is short-circuited at the end of the transmission line, a reflected pulse with opposite polarity can be generated. The short-circuit line method uses this principle to convert a unipolar pulse into a bipolar pulse by designing a circuit module. Specifically, after a short-circuited transmission line connected in parallel with the output of the sub-nanosecond pulse generator, the output pulse will be split into two paths when transmitted to the parallel node. One pulse continues to transmit forward and the polarity is unchanged; the other pulse enters the short-circuit transmission line and then totally reflects at the end, which means that the pulse polarity is reversed and there is a time delay with the previous pulse. When the pulse with reversed polarity returns to the parallel node, the pulse is divided into two paths again, one of which continues to transmit forward and can be superimposed with the previous pulse. If the total delay between the two pulses is close to or slightly smaller than the pulse width, the superposition will result as an ideal bipolar pulse. As shown in Figure 11 (a), the short-circuit line circuit module is designed by using microstrip line. In the experiment, by connecting the circuit module in series with the output of the pulse generator, the sub-nanosecond unipolar pulse with the amplitude of 3.8 kV can be converted into a sub-nanosecond bipolar pulse with a peak-to-peak amplitude of about 2.5 kV, as shown in Figure 11 (b). The experimental results show that the short-circuit line method can realize the dual polarization of the pulse under the

condition that the pulse rise time is nearly not affected. As a result, this method is simple in structure, high in efficiency, stable and reliable, but requires the output unipolar pulse duration time should be as short as possible.

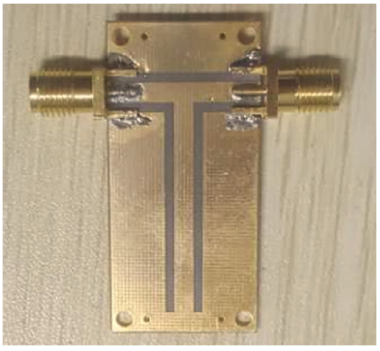

(a)

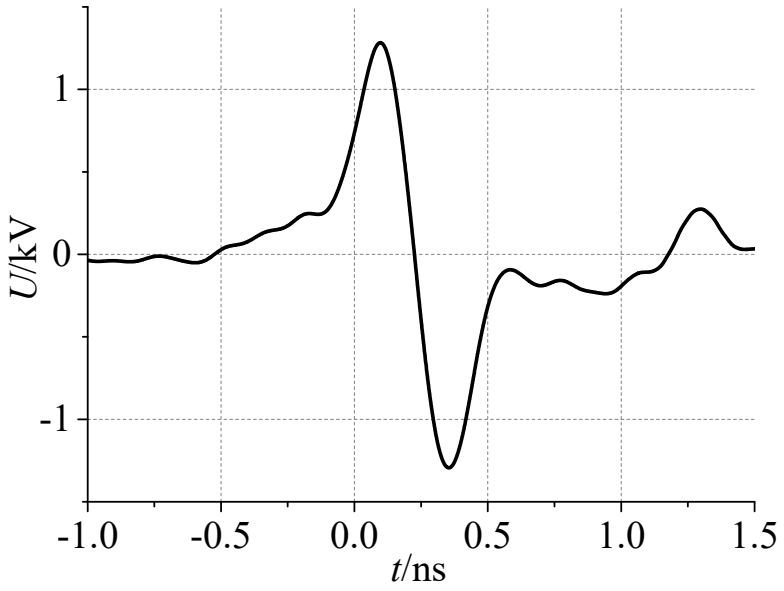

(b)

Figure 11. (a) Short-circuit line circuit module. (b) Output bipolar pulse using short-circuit line method.

2.4.1.2 Pulse synthesis method

The principle of the pulse synthesis method is to directly synthesize a positive unipolar pulse and a negative unipolar pulse with time delay through a wideband power combiner to form a bipolar pulse, as shown in Figure 12. For the solid-state sub-nanosecond pulse generator, the polarity of output pulse can be reversed by adjusting the polarity of the transistor in circuit design, and the time delay between positive and negative pulses can be adjusted by controlling the timing of the trigger signal or adjusting the length of the delay

line. The principle of pulse synthesis is simple and straightforward; but in practical application, the delay jitter between positive and negative pulses may cause distortion and instability of the synthesized bipolar pulse waveform. The delay jitter can usually be reduced by increasing the amplitude of the trigger signal and reducing the rise time of the trigger signal. As shown in Figure 13, a bipolar pulse is obtained by pulse synthesis method, in which the peak-to-peak value of the converted bipolar pulse is about 450 V and the amplitudes of the original positive and negative sub-nanosecond pulse are 800 V and -800V respectively. The experimental results show that the pulse synthesis method can realize the flexible control of bipolar pulses. However, the delay control of the two pulse generators is required in the development process; the efficiency of the pulse synthesis process is also limited by the characteristics of the wideband power combiner.

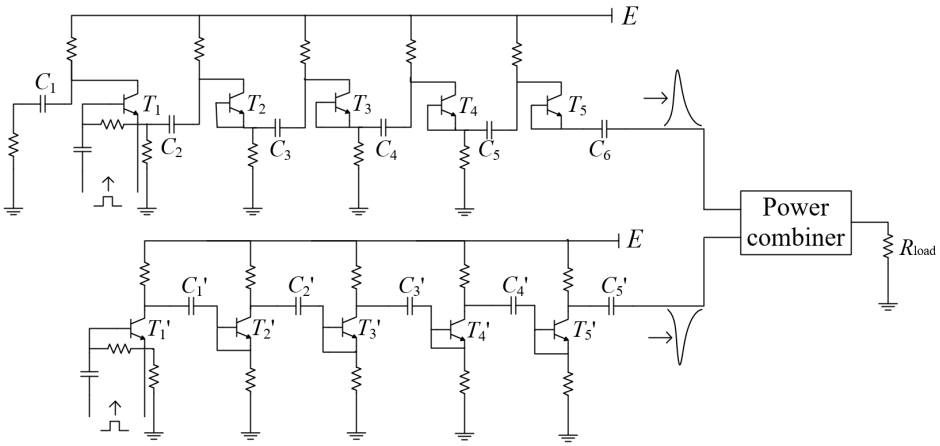

Figure 12. Circuit diagram of the developed bipolar pulse source.

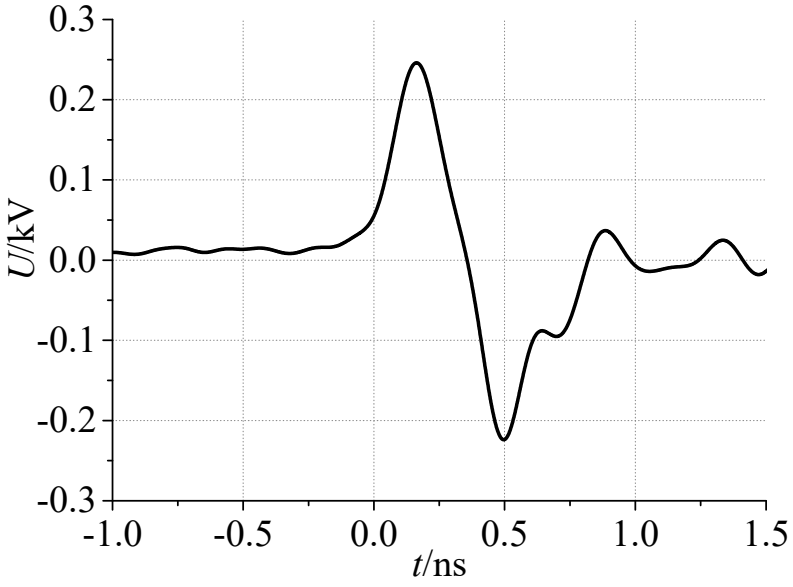

Figure 13. Output sub-nanosecond bipolar pulse using pulse synthesis method.

2.4.2 Techniques for polarity reversal of sub-nanosecond pulse

For some practical applications of sub-nanosecond pulse generators, sometimes different pulse polarities may produce different effect phenomena. In addition to redesigning the Marx circuit to reverse the polarity of the transistor and generate the pulse with reversed polarity, this thesis also proposes a pulse polarity reversal module based on transmission line transformer (TLT), which can change the polarity of sub-nanosecond pulse more conveniently and efficiently[54].

Conventional transformers generally have poor high-frequency characteristics. Due to the influence of distributed capacitance and leakage inductance, it is difficult to effectively increase the upper limit operating frequency even if the magnetic core material having a wide frequency band and high magnetic permeability characteristics. On this basis, the transmission line transformer combines the theory of both transformer and transmission line to achieve better wide bandwidth characteristic. The magnetic core material with high permeability and low loss is used to form a toroidal core, which is wound by parallel wires or coaxial lines with transmission line structure. And its equivalent circuit finally constitutes an *L*-*C* circuit network similar to the equivalent circuit of lossless transmission line. The equivalent impedance of the circuit is related to the core structure, material and wires' winding structure [92]. Under high frequency condition, the transmission line transformer mainly works in the transmission line mode, and its upper limiting frequency is limited by the equivalent length of the transmission line; under low frequency condition, the transmission line transformer works mainly in the transformer mode, and its low frequency characteristic is mainly affected by the excitation current of the magnetic core.

The pulse polarity reversal module based on the transmission line transformer is shown in Figure 14 (a). Its main principle is to exchange the winding wires on one side of the transmission line transformer, i.e. the original grounding wire is connected to the core wire of output port and the original core wire is connected to the ground of output port , and finally realize pulse polarity reversal by this method. In the design of the module, it is necessary to pay attention to selecting a wideband transmission line transformer to ensure that the operating frequency band covers the main frequency components of the sub-nanosecond pulse. A PCB-based pulse polarity reversal module is fabricated by using the wideband transmission line transformer produced by Mini-Circuits, as shown in Figure 14 (b). By using this circuit module, the positive polarity sub-nanosecond pulse with

amplitude of 3.5 kV can be converted into the negative polarity pulse with the same amplitude absolute value, as shown in Figure 14 (c).

The experimental results show that the pulse polarity is reversed after connecting the pulse polarity reversal module, and the parameters such as the pulse rise time and the absolute value of the pulse amplitude are almost unchanged. It is considered that this module has the characteristics of stable operation, wide bandwidth and low loss. In addition, since the wideband transmission line transformer packaging is quite small and the distance between the wires is very close, it is necessary to reinforce the insulation of transmission line transformer winding and its packaging when used for higher amplitude pulse polarity conversion.

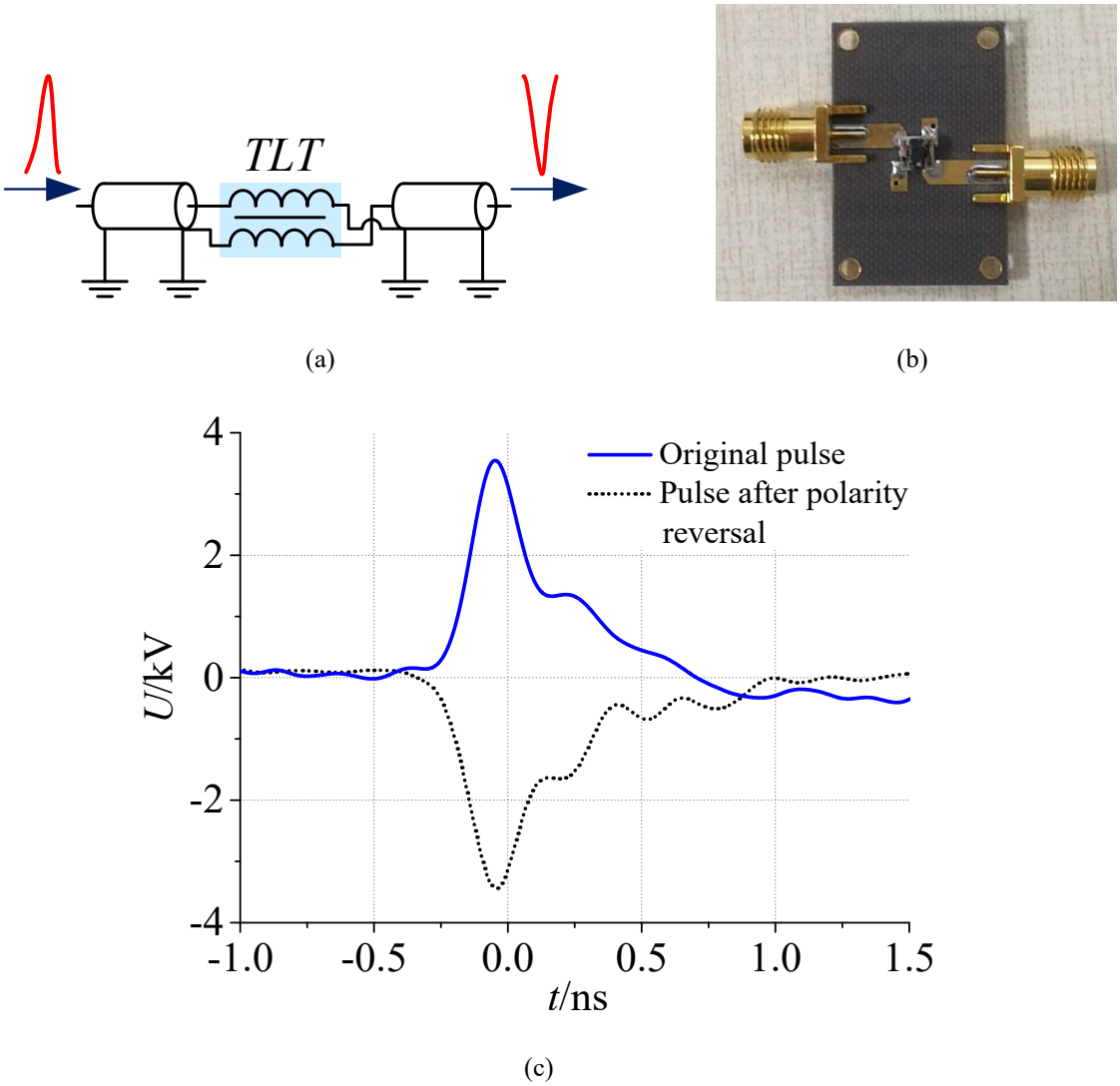

Figure 14. (a) Pulse polarity reversal module. (b) Fabricated circuit of pulse polarity reversal module. (c) Output sub-nanosecond pulse using pulse polarity reversal module.

3 TRAVELING-WAVE MARX CIRCUIT MODEL

This chapter mainly introduces the modeling of the traveling-wave Marx circuit. In-depth circuit analysis has been developed to study the influence of inter-stage transmission lines on sub-nanosecond pulse waveform. According to the analysis results, some applications, such as modularized Marx circuits in series and novel heat dissipation design, are proposed.

3.1 Modeling of the Traveling-wave Marx Circuit

Usually, Marx circuit can generate pulses with rise time ranging from nanosecond to microsecond. The lumped parameter Marx circuit based on the avalanche transistor is shown in Figure 15, in which the parallel charging Marx circuit is adopted. In this *n*-stage Marx circuit, the paralleled isolation resistors R_{1i} and R_{2i} (i=1, 2, … , n) are used in each stage, which have the advantages of fast and consistent charging time compared to the serial isolation resistors in the traditional one. Its main working process can be described as follows: in the charging process, capacitors are charged by the currents flowing through isolation resistors. Then, during the pulse forming process, with the avalanche breakdown of the transistors, all capacitors are connected in series and discharged on the load.

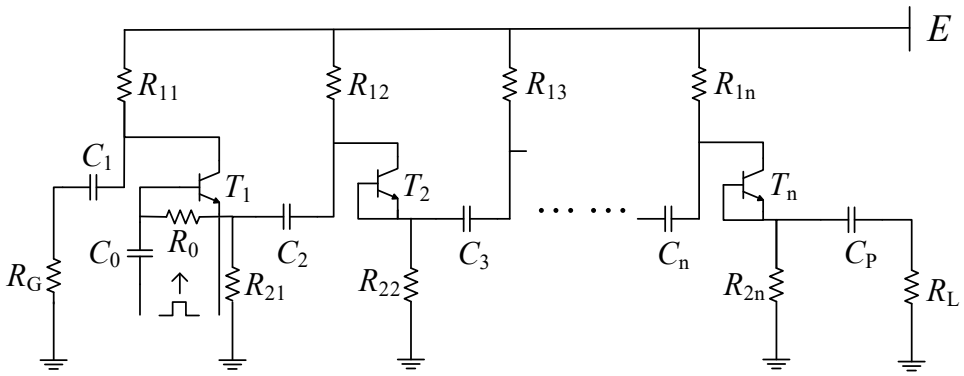

Figure 15. Lumped parameter Marx circuit based on avalanche transistor.

However, when the pulse rise time is reduced to the order of sub-nanosecond, the effects of distribution parameters and traveling-wave processes cannot be ignored in the circuit analysis and modeling. To optimize the output parameters in circuit design, researchers

have adopted the distributed capacitor and inductor in each stage of the Marx circuit model[23]. Nevertheless, the time delay effect of the distributed *L*-*C* circuit is limited and neglected. In order to analyze the switch-closure propagate process in fast pulse-power systems, the traveling-wave Marx generator was proposed by Carl E. Baum[55]. In that study, the refraction and reflection phenomena of the pulse traveling-wave at the switch nodes were introduced to the pulse forming process. Therefore, to optimize the performance of the sub-nanosecond pulse generator, in-depth study on the traveling-wave Marx circuit is necessary.

For the Marx circuit generating sub-nanosecond pulse, its circuit model should be regarded as an electrically large circuit and the traveling-wave transients in the pulse forming process cannot be ignored[56]. Take a transistor-based pulse generator as an example, the physical length of a 48-stage Marx circuit is about 30 cm (along the pulse forming path), as shown in Figure 16 (b). The output pulse waveform of the pulse generator is shown in Figure 16 (a), in which the pulse based width is about 1 ns.

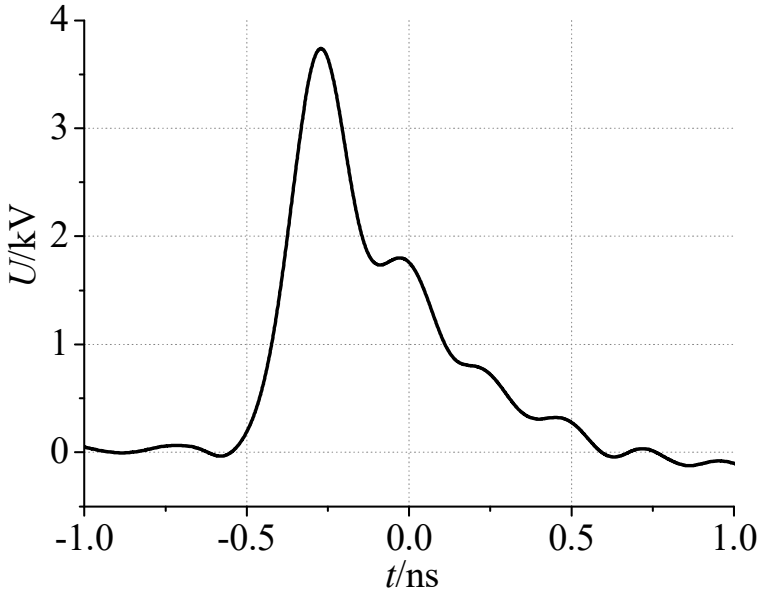

(a)

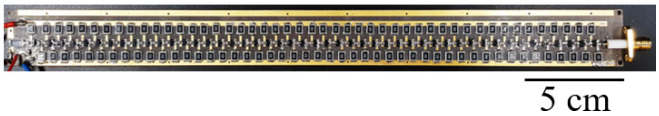

(b)

Figure 16. (a) Measured pulse waveform of the 48-stage Marx circuit. (b) Photo of the 48-stage Marx circuit with the physical length of 30 cm.

It is noteworthy that the transmission length of the pulse width is about 20 cm, which is smaller than the circuit length of the pulse generator. It means that the propagation process of the switch-closure and pulse wave forming should be considered in the generation of sub-nanosecond pulses. In this condition, the pulse forming process is no longer a process in which capacitors connect in series simultaneously and discharge at the same time, but a traveling-wave process considering the time delay and the impedance matching of every stage in the Marx circuit. In this case, techniques of high frequency circuit need to be introduced in the PCB design of the Marx circuit, e.g. introducing the microstrip lines in each stage. Thus, a more precise circuit model should be adopted for the study of the pulse forming process, which covers not only the influence from the distributed parameters, but also the time delay from the equivalent transmission lines.

Referring to the traveling-wave Marx generator proposed by Carl E. Baum, a traveling-wave Marx circuit model considering inter-stage transmission lines is adopted to analyze the pulse forming process in a transistor-based sub-nanosecond pulse generator, as shown in Figure 17. The inter-stage microstrip lines on the PCB are simulated as transmission lines in series, which are used to introduce the time delay or loss effects in each stage. Depending on the circuit structure, the inter-stage microstrip lines' impedance is usually 50 Ω or slightly smaller, and their delay time varies from tens to hundreds of picoseconds in general. As the number of stages increases, the total delay time of the equivalent transmission lines in the Marx circuit can reach several nanoseconds.

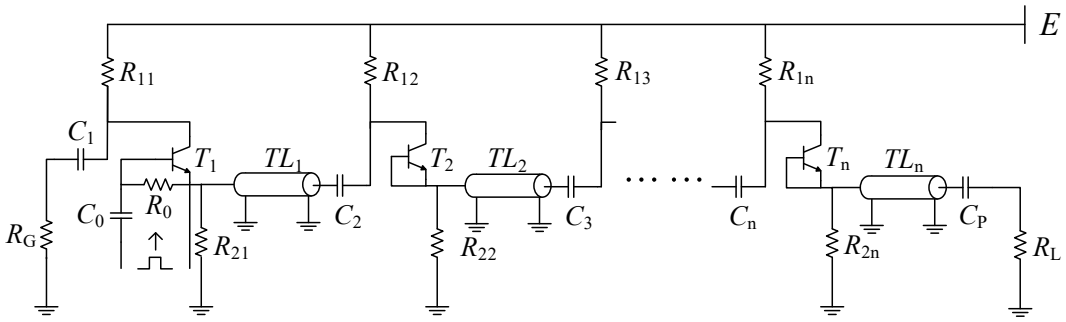

Figure 17. Traveling-wave Marx circuit model considering inter-stage transmission lines.

Based on the traveling-wave Marx circuit model, the pulse forming process can be described concretely, as shown in Figure 18. According to the circuit structure shown in Figure 18 (a), the traveling-wave Marx circuit is divided into *n* stages including inter-stage transmission lines, which are labeled as S_1 to S_n respectively. Stages with different colors

indicate different working states of capacitor and transistor. Once the first stage transistor T_1 is triggered, the capacitor in the first stage C_1 begins to discharge and the corresponding transistor enters into avalanche mode, forming a pulse travelling along the transmission line TL_1, as shown in Figure 18 (b). With the pulse triggering the subsequent transistors, the avalanche breakdown happens and the pulse amplitude can be superimposed as a result of the series connection of charging capacitors, as shown in Figure 18 (c). In this process, the inter-stage transmission lines act as the propagation medium for the generated pulse traveling-wave and the equivalent load for the triggered part of the Marx circuit. It is worth noting that, due to the delay of inter-stage transmission lines, the capacitors at different stages discharge in sequence; when the pulse wave travels far enough, the initial discharging capacitors may have been almost discharged, as shown in Figure 18 (d). On this basis, when the pulse is generated at the load R_L, the capacitors near the load terminal, rather than all capacitors, are mainly involved in the discharge process for the pulse tail forming, as shown in Figure 18 (e).

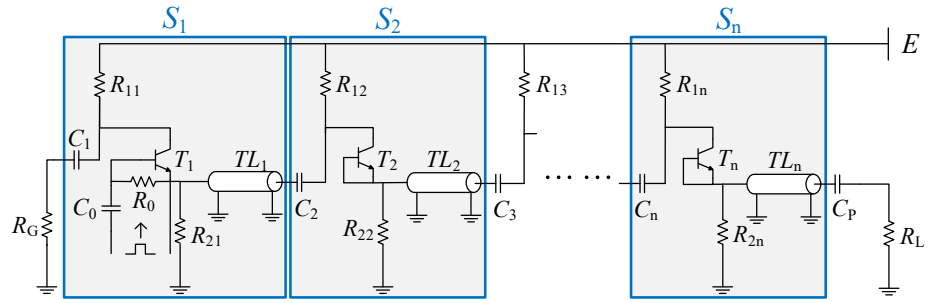

(a)

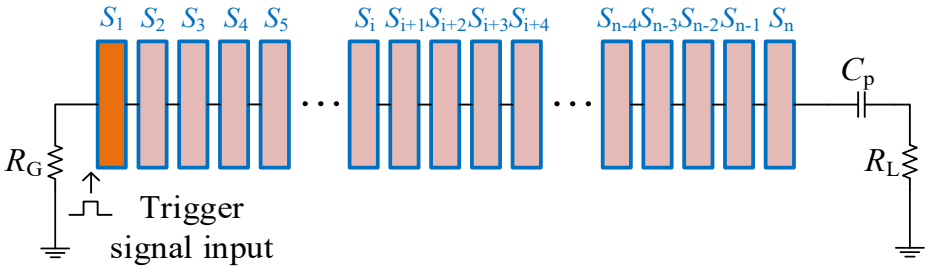

(b)

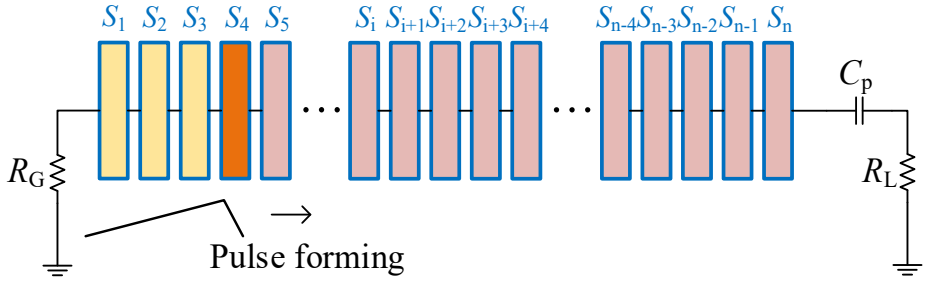

(c)

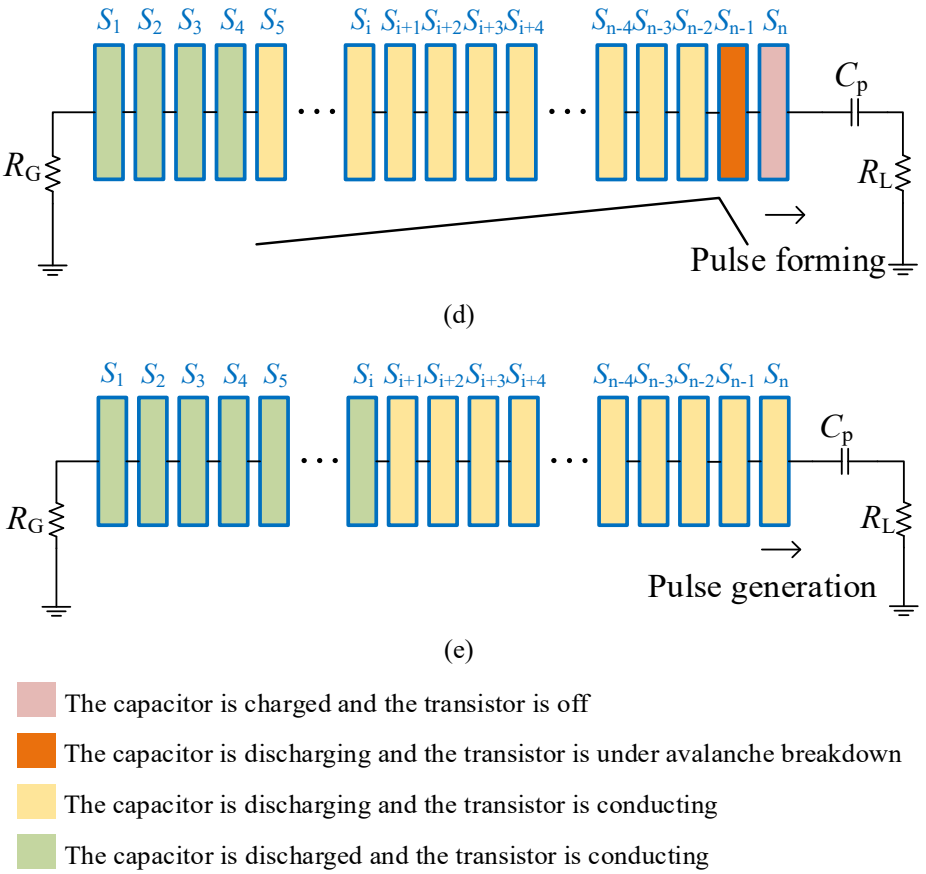

Figure 18. Pulse forming process in the traveling-wave Marx circuit model. In (a), the traveling-wave Marx circuit is simplified into the series connection of stages in blocks. From (b) to (e), the sketches of the pulse forming process is demonstrated by characterizing the different conditions of stages in Marx circuit.

3.2 Simulation Study of the Traveling-wave Marx Circuit Model

In order to analyze the impact of the inter-stage transmission lines with different parameters, the traveling-wave Marx circuit is simulated with PSpice, as shown in Figure 19. In the established 20-stage Marx circuit, the type of the avalanche transistor is FMMT415 module, whose Spice model is provided by the manufacturer[57, 58]. The inter-stage microstrip line is simplified as a lossless transmission line with adjustable parameters of delay time and impedance. The trigger signal source is a square-wave generator with the rise time of 1 ns and the amplitude of 50 V. In addition, the direct current (DC) supply voltage is 300 V and the load R_L is 50 Ω.

To analyze the pulse forming process, some voltage probes are added to measure the voltages across the 5th, 10th, 15th, 20th capacitors and the load voltage, respectively.

According to the actual circuit, parameters of the transmission line are set as 0.05 ns/50 Ω and the simulation results are depicted in Figure 20 (a). It is shown that these capacitors discharge in sequence, and the time points of discharge are directly related to the traveling-wave propagation delay during the pulse forming process. Under this condition, the pulse amplitude is more than 1.6 kV and the rise time is less than 200 ps.

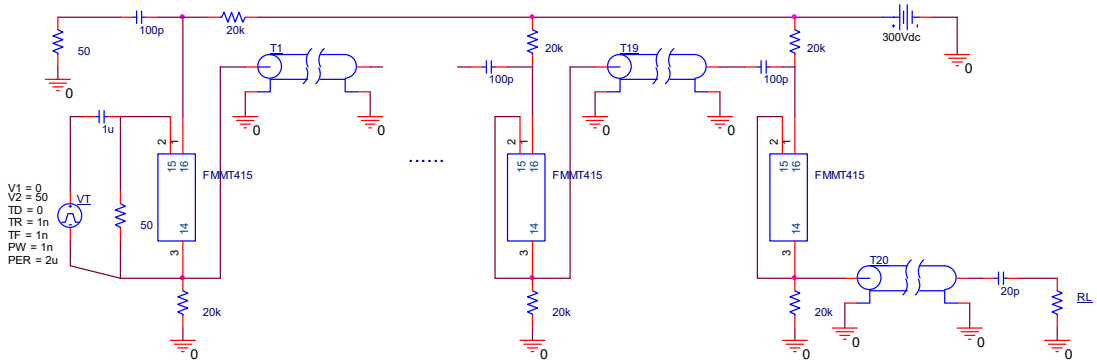

Figure 19. The simulation circuit of 20-stage Marx circuit considering inter-stage transmission lines. Some of the repeated stages in the Marx circuit are hidden for simplicity.

The delay time of the inter-stage transmission line corresponds to the length of the microstrip line, which could affect the cascade process of the charging capacitors with pulse amplitude superposition. In the simulation study, the delay time of each transmission line is adjusted to 0.1 ns, 0.15 ns and 1 ns respectively, as shown in Figure 20 (b) to (d). By increasing the delay time, the discharge start time changes significantly for capacitors in the same stage; meanwhile, the pulse amplitude decreases and the rise time is almost unchanged. As the number of stages increases, the discharge time of different capacitor is shortened, due to the reduction of the corresponding time constant after the series connection of capacitors.

Besides, the simulated working process of the traveling-wave Marx circuit has also proved the equivalent load effect of the inter-stage transmission lines mentioned in section II. With the increase of the delay time of the transmission line, the original pulse forming mode in the lumped parameter circuit has changed: capacitors discharge to the inter-stage transmission line as equivalent load, and then pulse is superimposed by next capacitor with the support of the inter-stage transmission line. Taking Figure 20 (c) as an example, these stage capacitors can be divided into two categories when the pulse is formed at the load side: the capacitors near the trigger terminal, such as the 5^{th} and 10^{th} stages, which have finished the discharge process; and the capacitors near the load terminal, such as those at

the 15th and 20th stage, which still have potential differences for pulse tail forming. A more extreme but representative example of the traveling-wave Marx circuit is shown in Figure 20 (d). When each transmission line has a delay time as long as 1 ns, almost all the charging capacitors are discharged before the pulse is formed at the load. In this situation, the pulse superposition process becomes asynchronous and the inter-stage transmission lines participate in the pulse forming and propagation process.

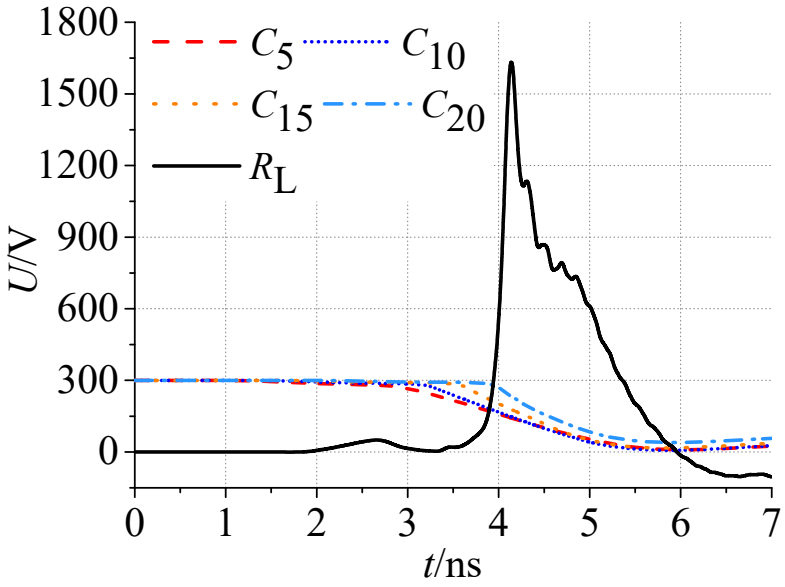

(a)

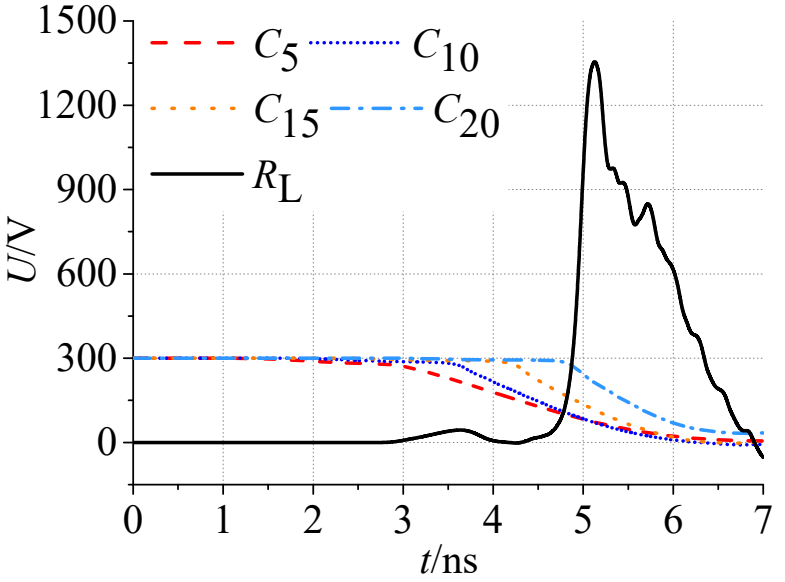

(b)

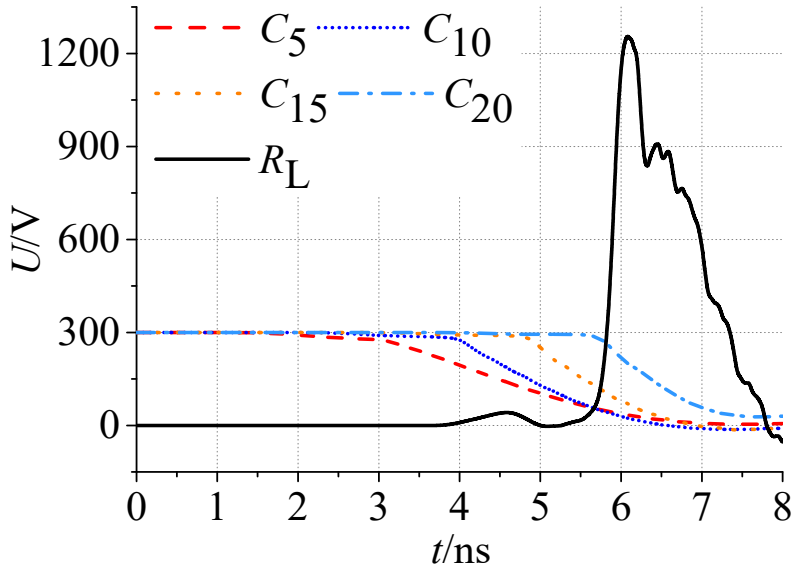

(c)

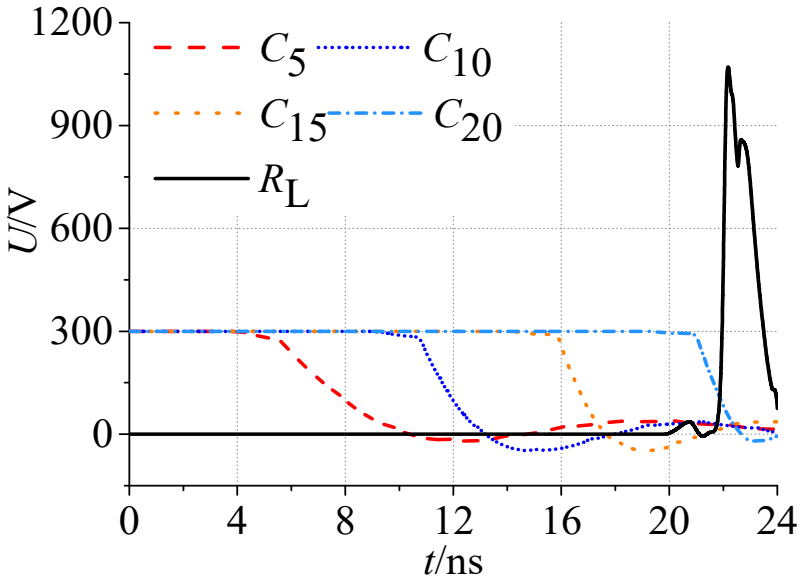

(d)

Figure 20. Simulated waveforms for the output pulse and the voltage across of capacitors at stage numbers of 5th, 10th, 15th, 20th in the traveling-wave Marx circuit considering inter-stage transmission lines. Form (a) to (d), the delay time of transmission lines is set as 0.05 ns, 0.10 ns, 0.15 ns and 1 ns respectively.

After introducing the inter-stage transmission lines, the impedance matching is another critical issue related to the output efficiency in Marx circuit. In the simulation, the impedance of the inter-stage transmission lines is changed to 25 Ω, 75 Ω and 100 Ω respectively, while the delay time of the transmission lines is fixed at 0.05 ns. As shown in Figure 21, when the impedance of the transmission lines is matched with the load

impedance 50 Ω, the amplitude of the output pulse reaches the maximum value. When the impedance value increases to 75 Ω and 100 Ω, the pulse amplitude decreases while the oscillation waveform at the pulse tail becomes remarkable. When the impedance value is set to 25 Ω, the pulse amplitude drops significantly with the reflection waveforms superimposed at the pulse tail.

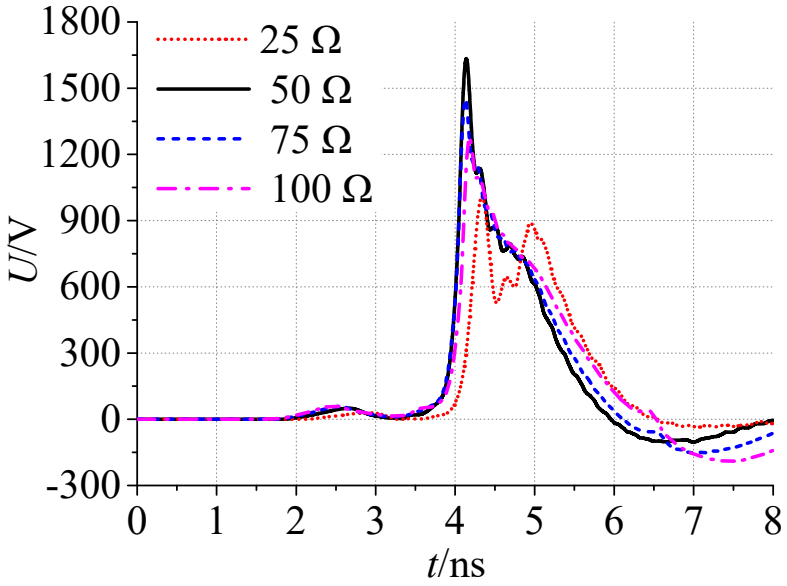

Figure 21. Simulated pulse waveforms with the impedance of inter-stage transmission lines of 25 Ω, 50 Ω, 75 Ω and 100 Ω respectively in the traveling-wave Marx circuit.

According to the above simulation results, the efficiency of the traveling-wave Marx circuit can be improved by introducing the inter-stage transmission lines with short delay time and matched impedance, which is also the key to the circuit structure design. In the time domain, the output pulse waveform will be affected or deformed due to the refraction and reflection on the inter-stage transmission lines. Along the pulse forming path, the charging capacitors and the transistors are alternately connected in series by the microstrip lines. The equivalent impedance of the microstrip line and the charging capacitor is usually small, compared with the load impedance 50 Ω. However, the equivalent impedance of the avalanche transistor is a variable in different working region: before the transistor working point enters the avalanche breakdown region, its equivalent impedance is maintained at a high-impedance state; when the avalanche breakdown starts, the equivalent impedance changes into the negative resistance condition, and the impedance value decreases rapidly until it reaches a fully conducting state. Therefore, at the connection points between the microstrip line and the transistor, the pulse waves are reflected before the complete

breakdown of the transistor. Due to the unidirectional conduction of the transistor, these traveling-waves may have multiple reflections on each inter-stage transmission line. When the length of the transmission line is close to or greater than the length of the reflected pulse wave, the traveling-wave process could result in the pulse distortion and dispersion, especially the decline of the pulse amplitude. On the other hand, the output impedance value of the pulse generator should be matched with the load impedance, to improve the output efficiency.

3.3 Microstrip Filter Effect in Traveling-wave Marx Circuit

The influence of the transmission line parameters during the pulse forming process can be also analyzed in the frequency domain by combining the theory of microstrip filters, which makes it easier to understand how the circuit PCB structure affects the pulse waveform.

3.3.1 Introduction to microstrip low-pass filter

Microstrip low-pass filters, such as stepped impedance filter and open-circuit stubs filters, are widely used in many microwave applications[59]. The low-pass microstrip filter typically consists of multiple microstrip lines with high and low impedance connected in series, which could be considered as a low-pass *L*-*C* filter based on distribution parameters. For a typical low-pass filter with series inductor *L* and parallel capacitor *C*, its cutoff frequency is $f_C = 1/(2\pi\sqrt{LC})$.

In the design of microstrip low-pass filters, the compact size and suppression of unwanted frequency components with excellent pass band characteristics are the major concerns. Generally, the design of microstrip low-pass filter can be divided into three main steps. Firstly, an appropriate low-pass filter prototype should be selected. As for microstrip low-pass filter, the filter prototype are classified according to different lumped-element prototypes, e.g. prototypes with series inductors and shunt capacitors, or prototypes with resonators in series inductors or shunt capacitors. Secondly, the filter design requires the choice of the type of response including pass band ripple and the number of reactive elements, which is the process to determine adequate design parameters of filter. Thirdly, also the most important step, we need to find an appropriate microstrip low pass filter type.

There are three commonly used microstrip low-pass filters, namely stepped impedance filter, low-pass filter with open-circuited stubs, and low-pass filter with attenuation poles.

3.3.1.1 Stepped impedance filter

The stepped impedance filter is a cascaded structure of high impedance and low impedance transmission lines. This type of microstrip low-pass filter consists of alternating sections of high-impedance and low-impedance lines which correspond to the series inductors and shunt capacitors in the lumped-element implementation. A typical stepped impedance filter and its equivalent circuit are shown in Figure 22, which is characterized in that the high-impedance lines with narrow width and the low-impedance section with wide width are sequentially connected in series.

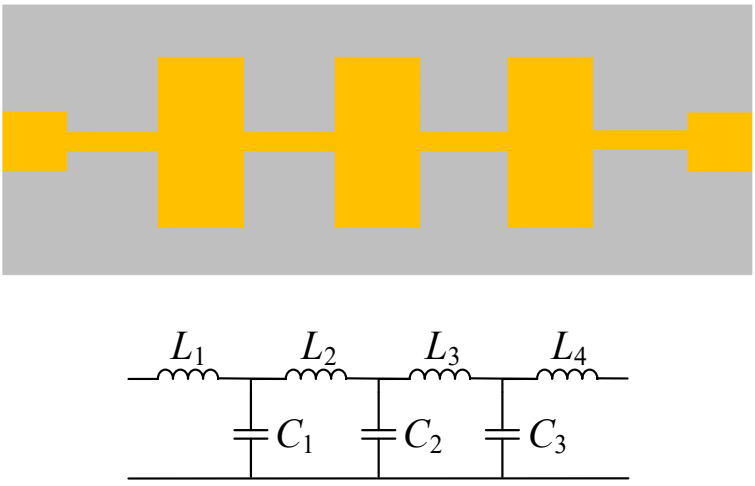

Figure 22. PCB structure of stepped impedance filter and its equivalent circuit working as a low-pass *L*-*C* filter.

There are several key points for the design of stepped impedance filter. As for the low impedance lines, lower impedance results in a better approximation of a lumped-element capacitor, but the resulting line width must not allow any transverse resonance to occur at operation frequency. As for the high impedance lines, higher impendence leads to a better approximation of a lumped-element inductor, but the impendence value must not be so high that its fabrication become difficult, or its current-carrying capability becomes a limitation. Typically, the source impedance of filter is 50 Ω, and the stepped impedance should be apparently lower or higher than 50 Ω for better performance. Theoretically, each element of the filter is $\lambda/4$ in length, where λ is the wavelength of the main-line signal to be blocked.

3.3.1.2 Low-pass filter with open-circuited stubs

The filter with open-circuited stubs is to implement the shunt capacitors as stubs with the resonant frequency set above the operating frequency so that the stub impedance is capacitive in the pass band. A typical low-pass filter with open-circuited stubs with its equivalent circuit is shown in Figure 23. For the design of low-pass filter with open-circuited stubs, the requirement is simply to make the capacitance as large as possible, for which the maximum stub width/length of $\lambda/4$ may be used. If the stub is required to be a very low impedance line, a possible solution is to connect two narrower stubs in parallel, which is similar to the PCB structure of stepped impedance filter. However, if the stubs length is too long, just like the design of low impedance lines, additional transverse resonant should be noticed and avoided as much as possible.

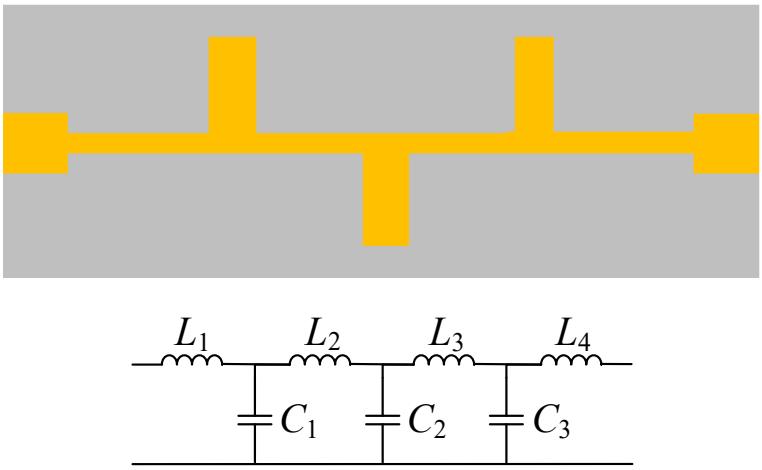

Figure 23. PCB structure of low-pass filter with open-circuited stubs and its equivalent circuit working as a low-pass *L*-*C* filter.

As for the design of open-circuited stubs, in order to get a wide stub, it's better to use radial stubs instead of linear stubs, so that the point at which they are connected to the main line is defined as shown in Figure 24. A pair of radial stubs in parallel is called a butterfly stub. And sometimes a group of three radial stubs in parallel is also used, which can be achieved at the end of a line, is called a clover-leaf stub. Commonly, low-pass filter with open-circuited stubs can exhibit a better stop band characteristic, compared with stepped impedance filter.

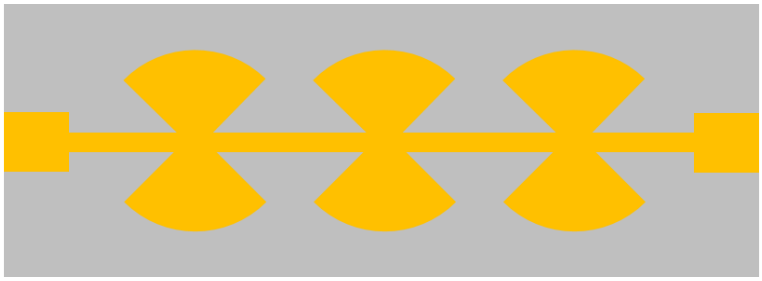

Figure 24. PCB structure of low-pass filter with open-circuited butterfly stubs.

3.3.1.3 *Low-pass filter with attenuation poles*

A more complex filter design is the low-pass filter with attenuation poles to obtain a sharper rate of cutoff and improve the stop band rejection. A typical low-pass filter with attenuation poles and its equivalent circuit are shown in Figure 25. Narrow lines are used to implement inductors and wide lines correspond to capacitors, but in this case, the lumped-element counterpart has resonators connected in shunt across the main line.

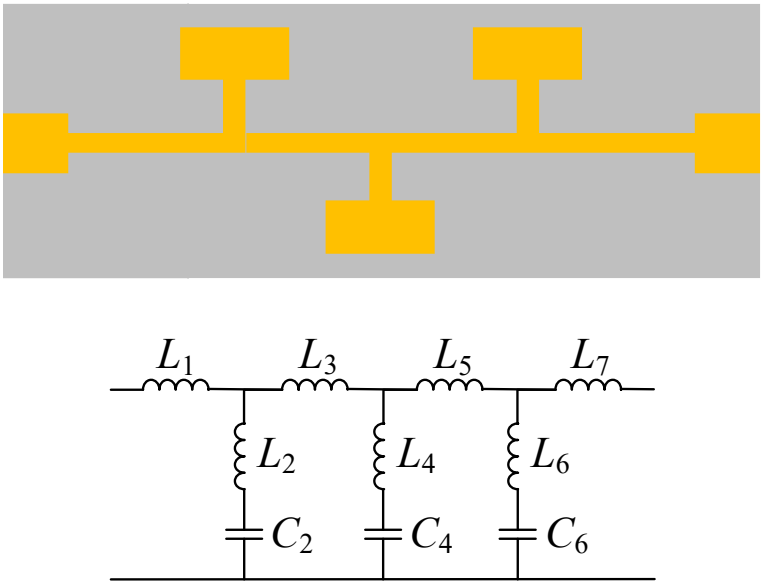

Figure 25. PCB structure of low-pass filter with attenuation poles and its equivalent circuit working as a low-pass filter with resonators.

3.3.2 Simulation study of the microstrip filter effect in Marx circuit

In order to analyze the low-pass microstrip filter effect in the Marx circuit of solid-state sub-nanosecond pulse generator, the basic circuit unit in the PCB of Marx circuit, i.e. the circuit modules with single low impedance transmission line, are simulated by comparing with corresponding experimental results. After this work, the specific microstrip filter

models with Marx circuit structure, which are closer to the real PCB of Marx circuit, are simulated to accurately study the filtering effects of different circuit configurations.

3.3.2.1 Analysis of circuit modules with single low impedance transmission line

In view of the conventional circuit design of such type of pulse generator, it is generally considered that its PCB structure can be simplified into the series connection of multiple low impedance transmission lines or open-circuited stubs in the pulse forming process. In other words, in order to connect transistors, capacitors, and resistors in the PCB of Marx circuit, the metallic pads always need to be designed as microstrip lines with low impedance, which is quite close to the PCB structure of stepped impedance filter or low-pass filter with open-circuited stubs.

Firstly, referring to the metallic pad structure in the fabricated Marx circuits, four circuit modules with different lengths of single low impedance transmission lines are modeled in Computer Simulation Technology (CST) software. In each circuit module, the main part is a 50 Ω microstrip line with a total length of 4 cm. In the center part of the microstrip line, a low impedance microstrip lines with the impedance of only 7 Ω is connected in series, and its length is set to 0, 1, 2.7, and 7 mm, respectively. These circuit modules can be used to analyze the filtering effects of sub-nanosecond pulses (transmitting on 50 Ω transmission line) caused by single low impedance transmission line on the PCB structure.

Take the circuit module with 7mm long low impedance transmission line as an example, and its simulation model is shown in Figure 26. The circuit model is a typical microstrip line circuit, and polytetrafluoroethylene (PTFE) is used as the material of dielectric medium in order to analyze its wide band filter characteristics. Both the front circuit and the back grounding plane of the PCB are made of the perfect electric conductor (PEC). Besides, at the microstrip line ports at both sides of the circuit, two discrete ports with S-parameter type are installed to analyze the frequency response characteristics of this two port circuit module.

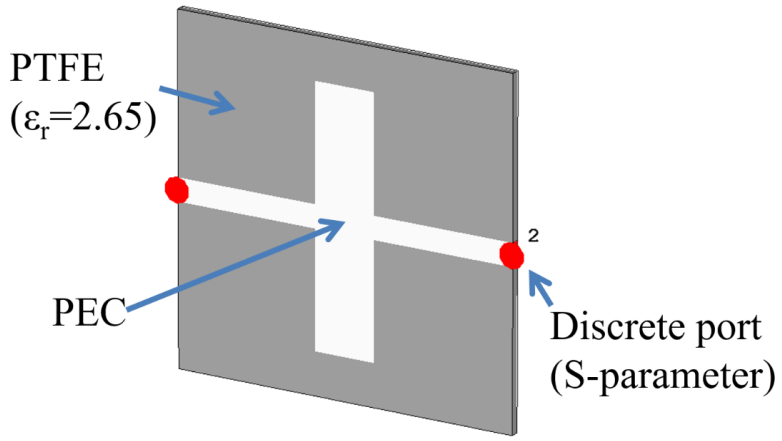

Figure 26. Simulation model of circuit module with 7mm long low impedance transmission line and discrete ports.

In the simulation, the time domain solver is used and the calculation frequency range is set to 0-3.5 GHz, which is also the main frequency component of the generated sub-nanosecond pulse. In order to analyze the low-pass filter effects of the circuit modules, the S_{21} parameter is considered as the main simulation object. As shown in Figure 27, the simulation results for the four circuit modules are plotted together to compare their different low-pass filter effects.

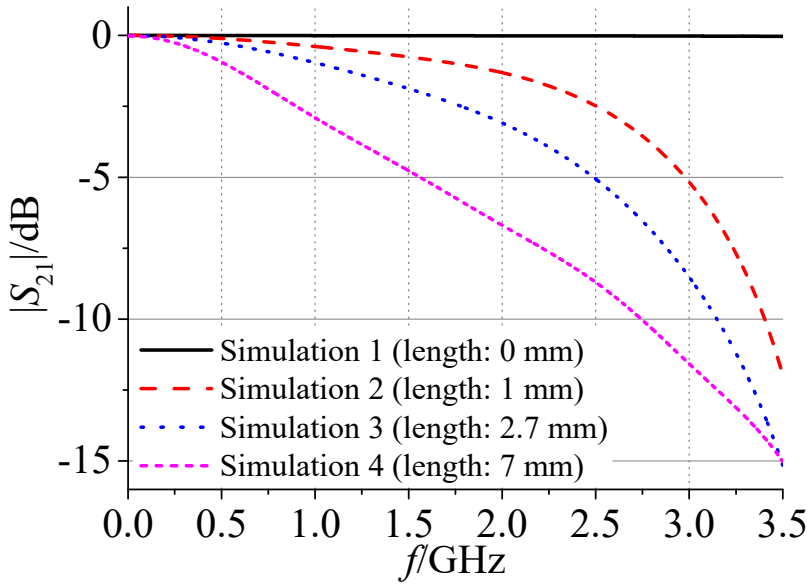

Figure 27. Simulation results of the four circuit modules with single low impedance transmission line.

In order to more accurately analyze these microstrip line circuits in simulation, we also tried to replace the excitation ports with the waveguide ports. Take the circuit module with 7 mm low impedance transmission line as an example, and its simulation model with the

waveguide ports is shown in Figure 28. Although the circuit structure is almost unchanged, the ports are replaced with waveguide ports and the boundary conditions on both sides of the ports and the back of the circuit are set to Electric (E_t=0), while the other sides are still Open (add space).

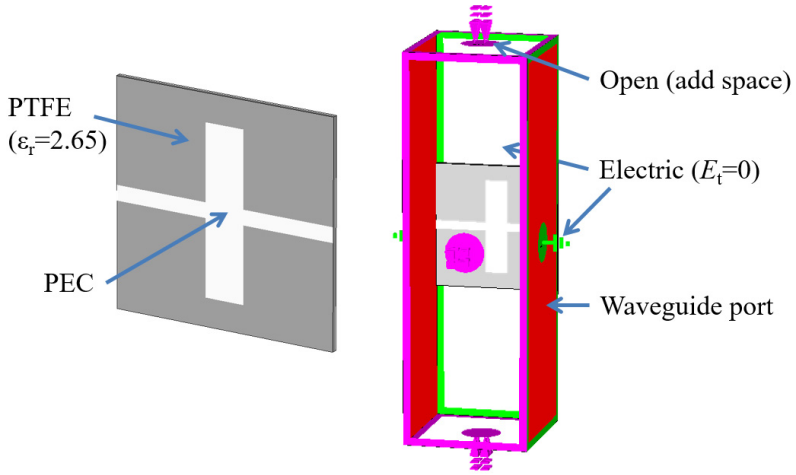

Figure 28. Simulation model of circuit module with 7mm long low impedance transmission line and waveguide ports.

The simulation results under different port conditions are shown in Figure 29. According to these results, we can get the conclusion that there is no significant difference between using the discrete ports and the waveguide ports for the models of circuit module.

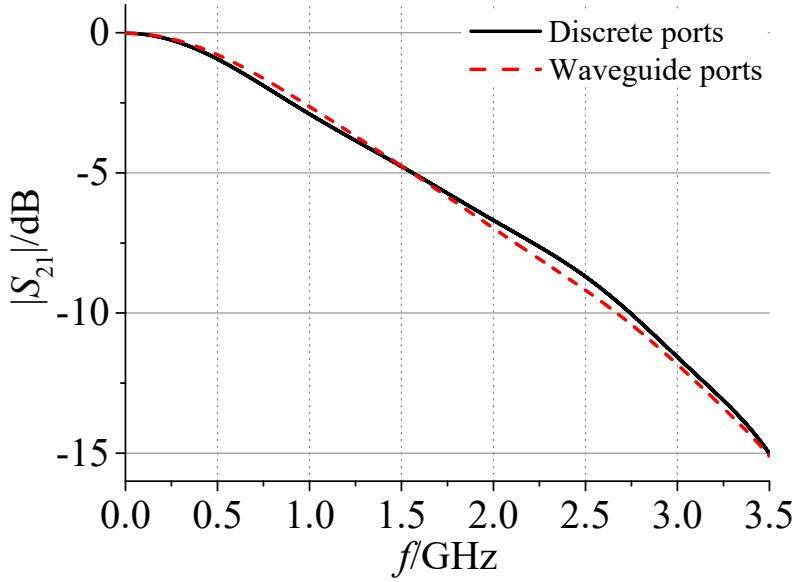

Figure 29. Simulation results of the circuit modules under different port conditions.

In order to verify the accuracy of the simulation results, the simulation model of circuit module with SubMiniature version A (SMA) connectors is also analyzed, since the

experimental circuit needs to use the SMA connectors for frequency domain measurement with the help of vector network analyzer. Once again, take the circuit module with 7mm low impedance transmission line as an example, and its simulation model with SMA connectors is shown in Figure 30. Because the geometry of SMA connector is difficult to be used for connection of waveguide port, a simplified coaxial connector is used for waveguide port excitation and simulation analysis.

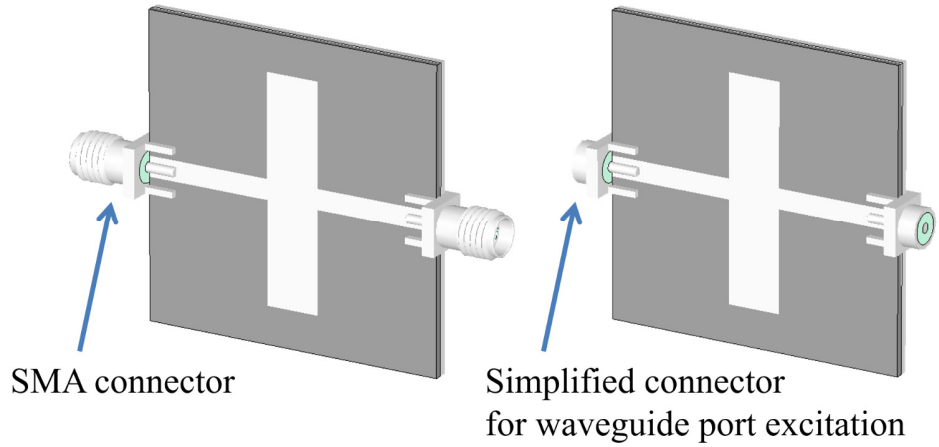

Figure 30. Simulation model of circuit modules with SMA connectors and simplified connectors.

The simulation results with and without simplified coaxial connectors are shown in Figure 31. Compared with the previous simulation result without coaxial connectors, the introduction of coaxial connectors has a very limited impact on the frequency response characteristics of circuit module, which means that the previous simulation results of the circuit modules are reliable.

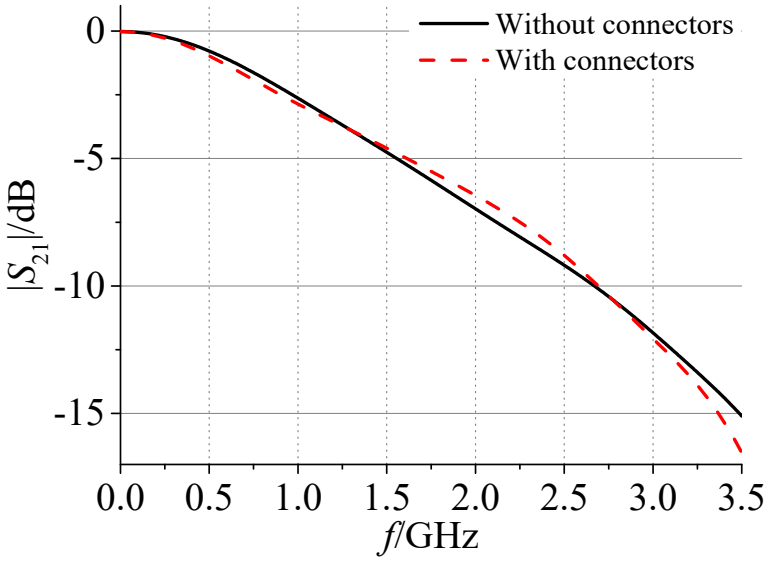

Figure 31. Simulation results of the circuit modules with and without connectors.

Based on the above simulation analysis results, circuit modules with the same PCB structure are designed and manufactured to verify the effectiveness of the simulation analysis. As shown in Figure 32, the fabricated modules are made with polytetrafluoroethylene dielectric board and SMA connectors are installed for measurements.

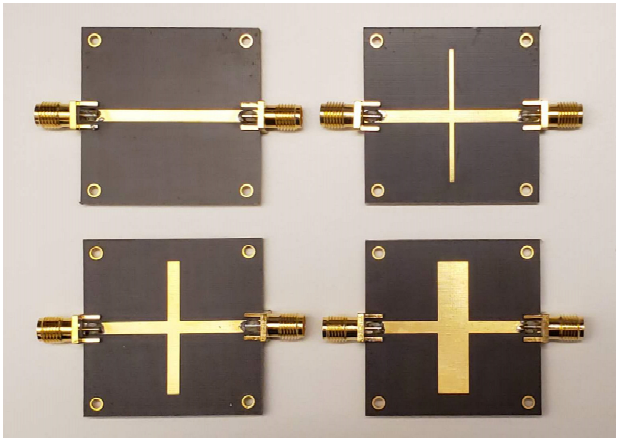

Figure 32. Fabricated circuit modules with different length of low impedance transmission line.

The experimental measurement platform is shown in Figure 33, in which network analyzer E5070B produced by Agilent technologies is used to measure the S_{21} parameters of the circuit modules in the frequency range of 300 kHz-3 GHz.

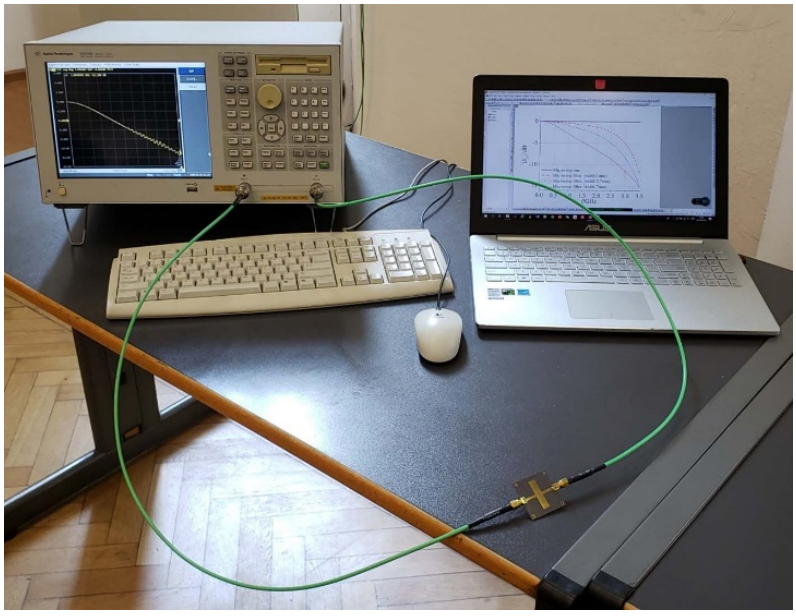

Figure 33. Experimental measurement platform with network analyzer.

As shown in Figure 34, the measurement and simulation results for the four different circuit modules are plotted in the same figure for comparison. According to both the

measurement and simulation results, with the length of the low impedance transmission line increases, the -3 dB cutoff frequency of the equivalent low-pass filter is reduced significantly, i.e. from around 2.6 GHz for 1 mm long low impedance line to around 1 GHz for 7 mm long low impedance line. This means that different pad sizes will have a very different effect on the high frequency components of the sub-nanosecond pulse. On the other hand, comparing the results from measurement and simulation, the simulation model can be considered to have good reliability and accuracy because the difference of S_{21} parameters for the same circuit module are always within 1 dB. By the way, some oscillation ripples are found in the measurement results, especially at high frequencies, which may be caused by non-ideal realization or some weak mismatching points from fabrication process like soldering.

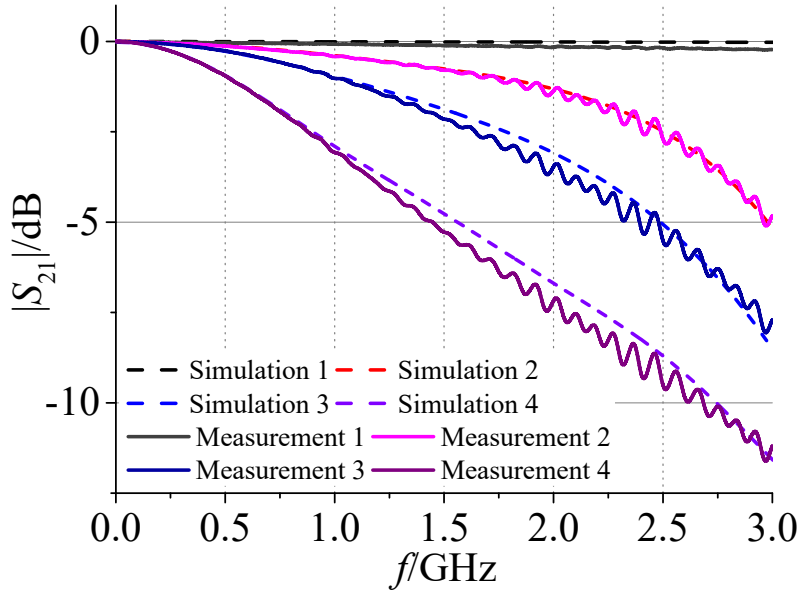

Figure 34. Measurement results of the fabricated circuit modules compared with relevant simulation results.

3.3.2.2 Analysis of microstrip filter models with Marx circuit structure

After analyzing the circuit modules with single low impedance transmission line, it's believed that the simulation results can accurately reflect the filtering effect of the PCB structure of Marx circuit. On this basis, considering that Marx circuits used in practical are always changeable, such as the number of stages and circuit configuration, simulation analysis of the PCB structure should be the best way to help the designer evaluate its low-pass filter effects.

According to the PCB design structure of the commonly used Marx circuit in solid-state sub-nanosecond pulse generator, the PCB structure can be simplified into a typical low-pass filter with periodic open-circuited stubs. The main approximation conditions for this simplification is that the transistors and capacitors are in a conducting state in sub-nanosecond pulse forming process, so these devices can be equivalent to metallic pads and be connected with the real pads on PCB. In this way, the simulation model used to analyze the Marx circuit low-pass filter effect can be easily simplified to a microstrip filter model.

Since the device package and circuit topology are fixed in circuit design process, the design of the PCB is mainly concerned with the space layout between the devices, especially the design of metallic pad structure. According to actual circuit configuration, this thesis presents an example of microstrip filter model with 4-stage Marx circuit structure, and analyzes its filter effects with different length and width of metallic pads, as shown in Figure 35.

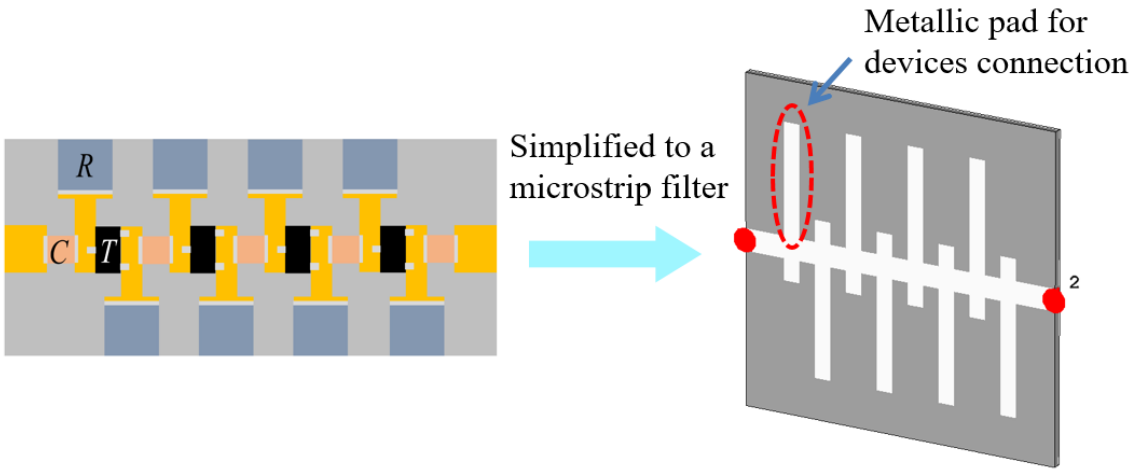

Figure 35. Microstrip filter model with Marx circuit structure after simplification.

As for the length of metallic pads, by adjusting the pad lengths to 10, 15, and 20 mm, respectively, the variation of frequency response characteristics can be simulated based on microstrip filter model. Figure 36 shows the simulation models in CST corresponding to different pad lengths.

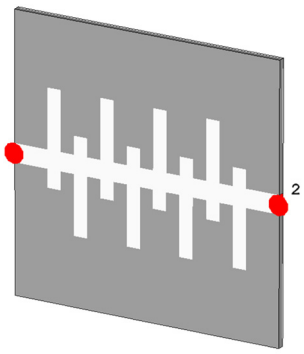

(a) Pad length=10 mm.

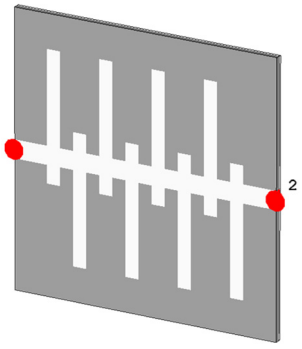

(b) Pad length=15 mm.

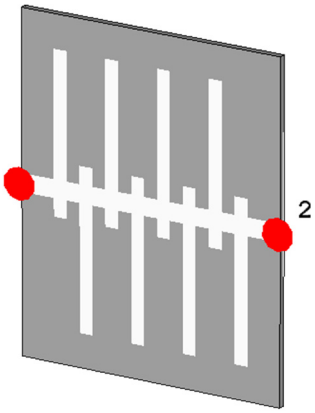

(c) Pad length=20 mm.

Figure 36. Microstrip filter models with different pad lengths.

Using the same simulation analysis settings as before, the simulation results for three different pad length conditions can be obtained in frequency domain, as shown in Figure 37. Simulation results of S_{21} parameter clearly show that the increase in pad length leads to a significant low pass filter effect of pulse high frequency components. When the pad length is increased to 20 mm, its -10 dB cutoff frequency will drop rapidly to nearly 2.5 GHz, and more seriously, its equivalent -3 dB bandwidth will be less than 1 GHz. Therefore, in order to avoid distortion of the pulse waveform, the length of the pads should be as short as possible, but some necessary conditions also need to be considered such as circuit insulation.

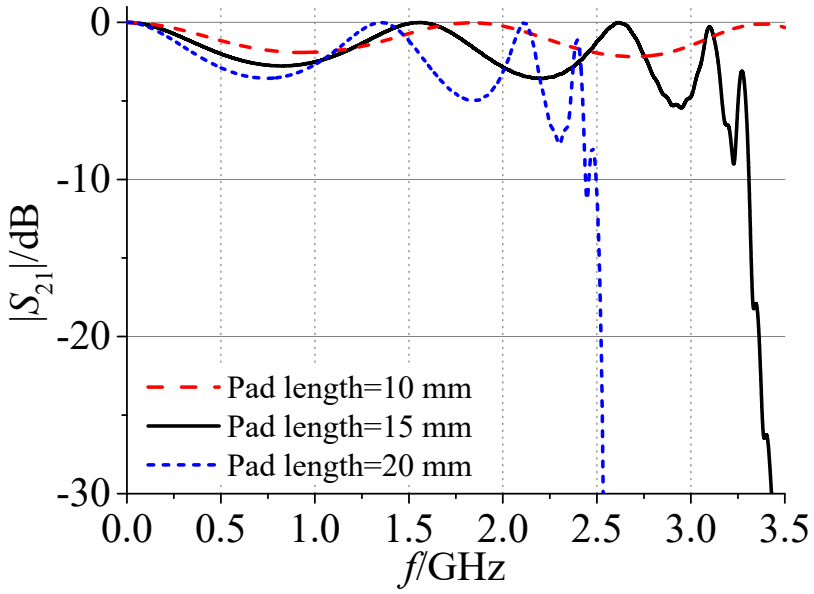

Figure 37. Simulation results of microstrip filter models with different pad length.

As for the width of metallic pads, by adjusting the pad widths to 1, 2, and 3 mm, respectively, the variation of frequency response characteristics can also be simulated. Figure 38 shows the simulation models with different pad widths.

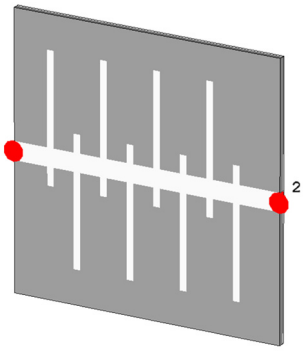

(a) Pad width=1 mm.

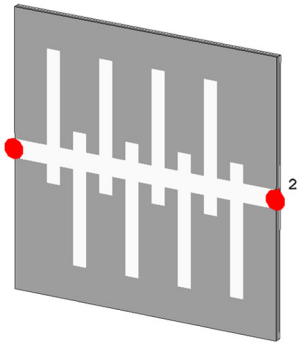

(b) Pad width=2 mm.

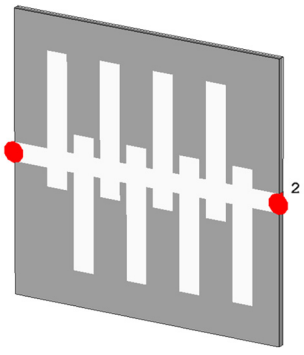

(c) Pad width=3 mm.

Figure 38. Microstrip filter models with different pad widths.

In Figure 39, the simulation results for different pad width conditions are plotted in frequency domain. Simulation results of S_{21} parameter show that there is no significant difference in their -10 dB cutoff frequency, which is around 3 GHz. However, their -3 dB band width varies widely, dropping from 3.0 GHz (pad width of 1 mm) to 2.0 GHz (pad width of 2 mm) and 0.5 GHz (pad width of 3 mm). As a result, the pad width should be as narrow as possible to increase its operating bandwidth for generating pulses with sub-nanosecond rise time.

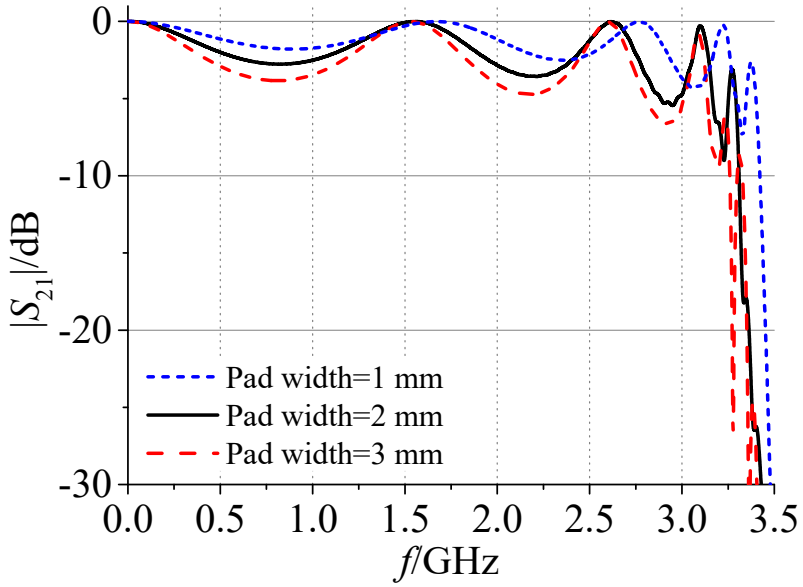

Figure 39. Simulation results of microstrip filter models with different pad width.

As a conclusion, the pulse forming path with a multi-stage periodic PCB structure can be regarded as a low-pass microstrip filter with stepped impendence or multiple open-circuited stubs due to the metallic pads act as inter-stage transmission lines. When the delay time of inter-stage transmission line increases, i.e. the increase of metallic pads width, the equivalent capacitance increases and the corresponding cutoff frequency decreases, which leads to the amplitude decrease due to low-pass filtering. When the inter-stage transmission line's impedance reduced, i.e. the increase of metallic pads length, the filtering effect of the microstrip low-pass filter could cause greater suppression of the high-frequency components, resulting in distortion of the output pulse waveform.

3.4 Applications of the Traveling-wave Marx Circuit Model

3.4.1 Modularized Marx circuits in series connection

In order to improve the output capability (especially the pulse amplitude) and the portability of the sub-nanosecond pulse generator, Marx circuits with different topologies have been studied and manufactured[60]. In addition to the series or parallel connection of transistors, modularized Marx circuits have been studied because of their advantages of higher pulse amplitude and flexibility. In the typical design, multiple Marx circuit modules are connected in parallel to generate high amplitude pulse by synchronous power combining [13, 14]. However, problems such as synchronous trigger at sub-nanosecond level and load mismatch limit the further integration of circuit modules in parallel connection. In addition, for a single Marx circuit, the increase in amplitude means a significant increase of the circuit physical length as a result of the increased stage number. For the needs of miniaturization and portability, the design of a bendable Marx circuit is required.

As shown in Figure 40 (a), based on the traveling-wave Marx circuit model, the Marx circuit modules can be connected in series through cables for adjustable pulse amplitude and compact circuit layout. The design of the traveling-wave Marx circuit model could be regarded as the increase of delay time of individual inter-stage transmission lines. To meet the impedance matching requirement, the coaxial ports for the pulse input and output are installed and connected with 50 Ω coaxial cables between the modules. The Marx circuit module can be used independently or connected in series with multiple modules to achieve a pulse generator with higher amplitude. It should be noted that if the pulse amplitude is too high, it is necessary to apply paralleled transistors in the Marx circuit at different stages or circuit modules. And the number of the parallel transistors could be calculated according to the predicted traveling-wave current and the peak collector current of the transistor. In addition to adjusting the pulse amplitude, compared with the conventional linear Marx circuit, this novel design realizes the bending property of the Marx circuit board.

A prototype of the modularized Marx circuits in series connection is developed and tested, including two 20-stage Marx circuit modules (module 1 and module 2), as shown in Figure 40 (b). And the output pulse waveforms of a single module and two modules are measured and shown in Figure 40 (c). By means of series connection of Marx circuit modules, the pulse amplitude can be adjusted, i.e. amplitude of 2.0 kV for single-module and 3.2 kV for two modules in series. Besides, the total length of the two 20-stage Marx circuit modules is

compressed to 13 cm, which is much shorter than the length of a linear 40-stage Marx circuit as 25 cm.

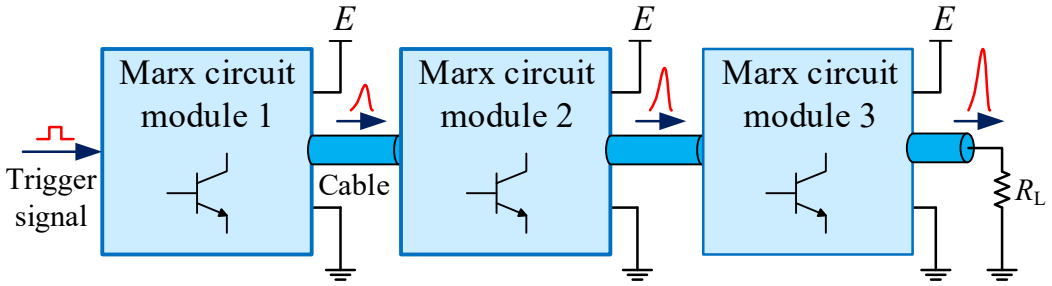

(a)

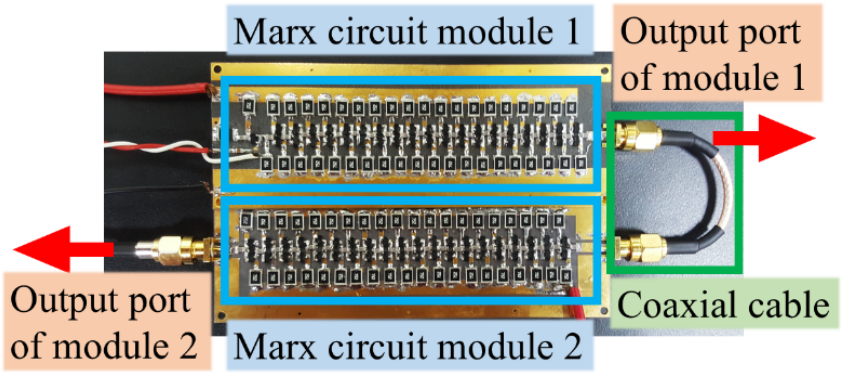

(b)

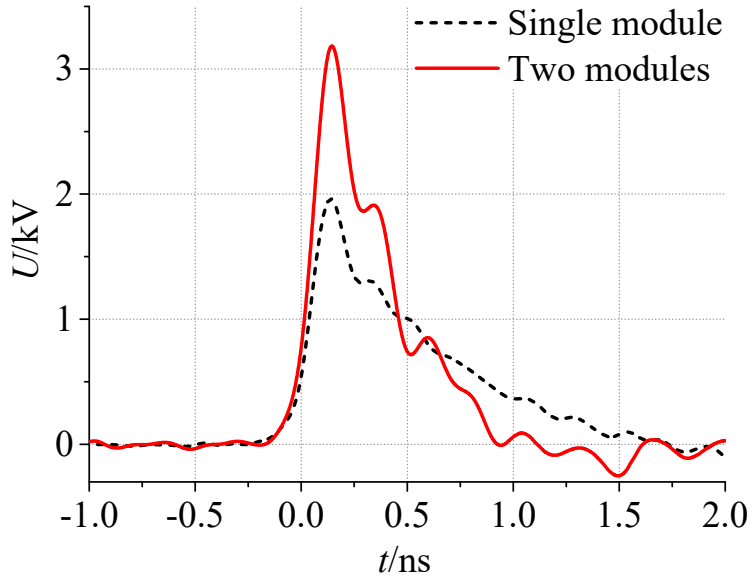

(c)

Figure 40. (a) Schematic of three modularized Marx circuits in series connection. (b) Photo of modularized Marx circuits consisting of two 20-stage Marx circuit modules in series. (c) Comparison of measured output pulses between a 20-stage Marx circuit module and two 20-stage Marx circuit modules connected in series.

Furthermore, to improve the pulse amplitude, two 50-stage Marx circuit modules are developed and connected in series with a high-voltage coaxial cable. The output pulse waveform is shown in Figure 41, in which the pulse amplitude is about 8.2 kV and the rise time is about 150 ps. To improve the peak current of the output pulse, parallel connection of two and three transistors are applied in the 1-25 and 26-50 stages of Marx circuit module 2 respectively, while the single transistor is used in each stage of Marx circuit module 1. For circuit physical size, the length of this pulse generator circuit is less than 35 cm, while the length of a linear 100-stage Marx circuit can be up to 60 cm. Pulse generators with compact size are more convenient for practical applications, such as EMC tests and biological electromagnetics experiments.

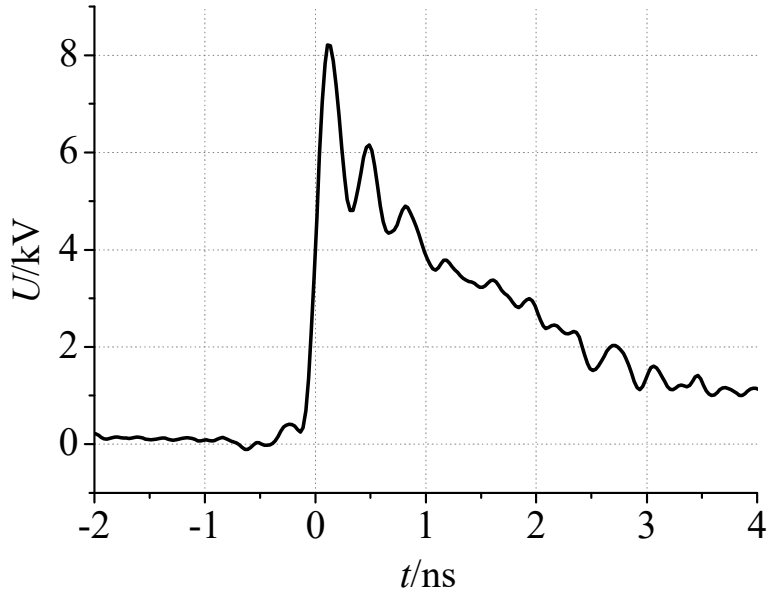

Figure 41. Measured pulse waveform of modularized Marx circuits consisting of two 50-stage Marx circuit modules connected in series.

3.4.2 Heat dissipation design considering the impedance matching of traveling-wave Marx circuit

To improve the output parameters of the pulse generator, especially the pulse repetition rate, a heat dissipation design is required due to large heating power. Let us take the design of a high-repetition-rate pulse generator with the amplitude of 1 kV as an example. In this generator, a 30-stage Marx circuit is adopted and the charging capacitor is reduced to 33 pF to improve the pulse repetition rate to 600 kHz (maximum theoretical value in circuit level). The measured pulse waveform of a testing circuit without a heat sink is shown in Figure 46 (a) as the black curve. However, in the testing process, when the pulse repetition

rate is increased to 200 kHz, the overheating of the transistors and the resistors on PCB are quite significant according to the infrared thermal image, and the highest temperature is about 60 ℃, as shown in Figure 42. With the increase of repetition rate, the heating power will continue to increase until the chip resistors fail at above 80 ℃. Therefore, it is necessary to adopt heat dissipation measures in the design of pulse generator circuit.

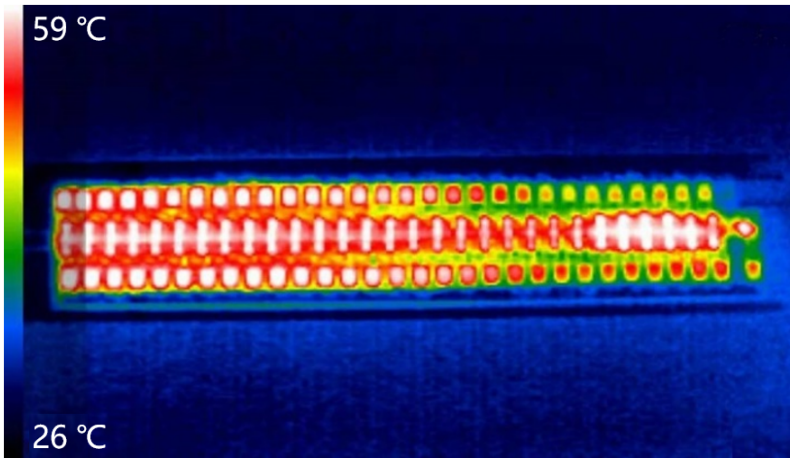

Figure 42. Measured infrared thermal image of the PCB of a 30-stage Marx circuit when the pulse repetition rate is 200 kHz.

The installing of heat sinks is a commonly used method to improve the heat dissipation capacity of the PCB[61]. The cross section of the PCB of Marx circuit is shown in Figure 43. It is noted that the transistors and the charging capacitors are connected alternately by the microstrip lines along the pulse forming path, which is designed to meet the impedance matching condition.

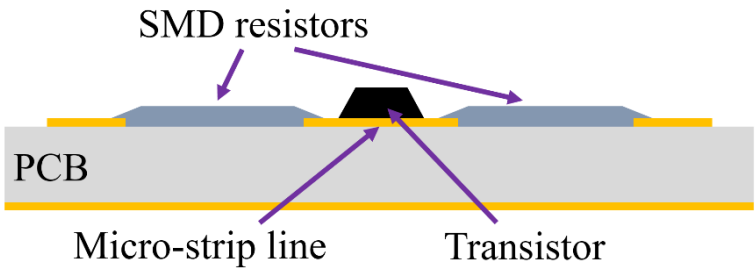

Figure 43. Cross section of the PCB of Marx circuit.

In general, the thermal pad is covered on the PCB surface and the metallic heat sinks are tightly installed above, as shown in Figure 44. This common design can effectively improve the heat dissipation capacity; however, the introduction of metallic sinks will also change the microstrip structure into strip lines, which leads to a significant reduction in the impedance and increase in the delay time. Based on this design, the measured pulse

waveform is shown in Figure 46 (a) as the red curve, in which the pulse amplitude is reduced by 40% compared with the pulse amplitude of the original design.

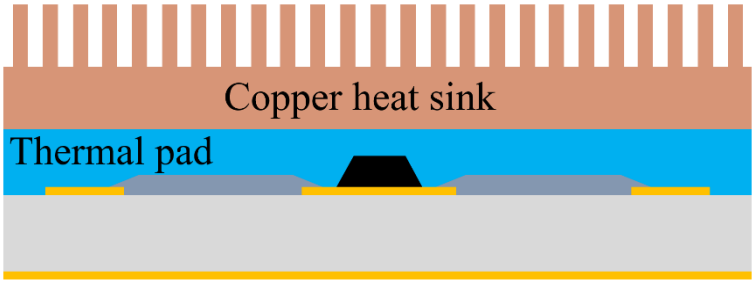

Figure 44. Common heat dissipation design of the PCB.

In order to meet the requirements of both heat dissipation and impedance matching, a novel heat dissipation design is proposed by optimizing the layout of metallic sinks on PCB, as shown in Figure 45. Specifically, in this design, the metallic heat sinks are partitioned and replaced by non-metallic heat-conducting sinks (e.g. heat-conducting ceramic sinks) above the microstrip lines. Compared with the metallic heat sink, the ceramic sinks with favorable heat conductivity have very low electrical conductivity, which has less influence on the distribution parameters of the microstrip lines. Thus, the impedance of the strip line is close to the original impedance in matching condition. As plotted in the blue curve in Figure 46 (a), the optimized output pulse amplitude reaches 80% of the original pulse. With the help of the novel heat dissipation design and forced air cooling condition, the pulse generator could work stably at the pulse repetition rate of 300 kHz and the pulse amplitude of 1.1 kV for more than 10 minutes, as shown in Figure 46 (b). Besides, its burst repetition rate could be 600 kHz within 1 minute.

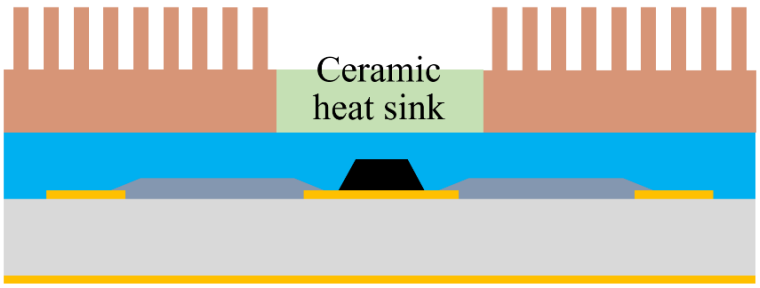

Figure 45. Novel heat dissipation design of the PCB.

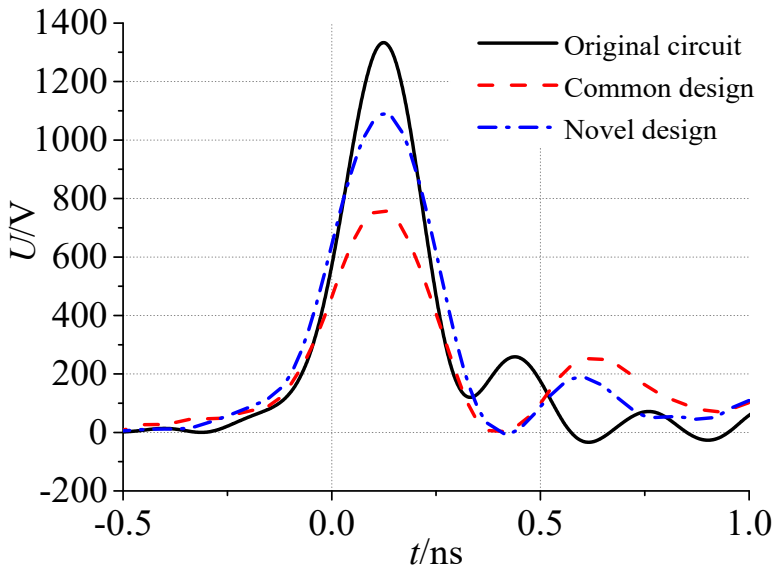

(a)

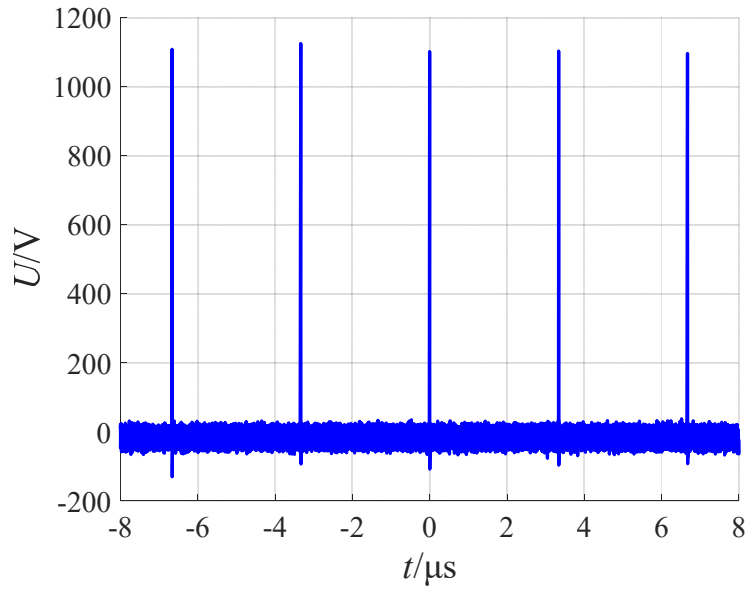

(b)

Figure 46. (a) Measured pulse waveform for Marx circuit in original, common heat dissipation design and novel heat dissipation design. (b) Measured pulse waveform with novel heat dissipation design, in which its pulse repetition rate is 300 kHz.

Thus, the electrical properties of the heat dissipation materials could affect the impedance value of equivalent inter-stage transmission lines in the traveling-wave Marx circuit. In order to improve the performance of the pulse generator, the integrated optimization of both the circuit design and the heat dissipation design is important.

4 DEVELOPMENT OF THE PORTABLE UWB ELETROMAGNETIC RADIATOR

This chapter introduces the development of the portable UWB electromagnetic radiator based on high-amplitude sub-nanosecond pulse generator, in which several new techniques are proposed for improving the pulse amplitude and a 2×2 combined antenna array is developed for UWB electromagnetic radiation.

4.1 Design of the High-amplitude Sub-nanosecond Pulse Generator

In the dsign of UWB electromagnetic radiator, a high amplitude pulse generator can generate UWB electromagnetic pulse with higher peak power, which is more likely to induce EMI effect and may produce special effects under high power condition. In order to design a sub-nanosecond pulse generator with high amplitude characteristics, the main factors that restrict the pulse amplitude increase should be analyzed first. For the transistor-based sub-nanosecond pulse generator, the limiting factors can be summarized as three main aspects: circuit working ability, transistor switching ability and circuit insulation ability.

Firstly, as for circuit working ability, pulse forming circuits should have the ability to generate high amplitude pulses in terms of circuit performance. Since the maximum breakdown voltage of the transistor is limited (around several hundreds Volts), it is necessary to increase the pulse amplitude by increasing the stage number of Marx circuit. At the same time, it is also necessary to improve the pulse isolation capability and charging rate of Marx circuit to generate high amplitude pulses while maintaining a high enough pulse repetition rate.

Secondly, in terms of transistor switching ability, the generation of high amplitude pulse is inseparable from the improvement of the switching current capacity. Although the instantaneous switching current of the avalanche transistor is quite high, excessive pulse

current or high pulse repetition rate will cause the decrease of transistor working life, which also affects the stable operation of the pulse source. In order to further improve the switching current capacity of the avalanche transistor, it is necessary to adopt the circuit design with parallel or series connection of transistors, provided that the current distribution among combined transistors is uniform and consistent.

Finally, in terms of circuit insulation, although the breakdown electric field of sub-nanosecond pulses is much higher than the breakdown electric field under DC condition, the circuit insulation design for generating high amplitude pulses is still very important. In the actual development of Marx circuits, at some impedance mismatching points, solder tips or fault points, a discharge phenomenon may occur during the high-amplitude pulse forming process, which may cause devices breakdown or even a serious circuit damage. Therefore, in the circuit design, the circuit insulation capability should be improved by means of isolation circuit optimization, device component selection, etc. In the manufacturing, test and use process, the operation of pulse generator should be strictly regulated.

4.1.1 Ferrite bead & resistor isolated Marx circuit

In the Marx circuit design of the high amplitude pulse generator, in addition to increasing the number of circuit stage, the optimization of the isolation circuit can directly affect the charging rate and the isolation capability of pulse. Although the parallel charging Marx circuit in such type of solid-state sub-nanosecond pulse generator could have a fast charging rate, there are some disadvantages also when used to generate high amplitude pulses. Compared with the conventional series charging Marx circuit (i.e. circuit with the isolation resistors connected in series between stages), the branches of paralleled isolation resistors are independent of each other. Therefore, its isolation capability of pulse is only related to the isolation resistors of the single branch, and the isolation resistors will directly withstand the full voltage of the high amplitude pulse, which may lead to potential insulation faults.

For the more commonly used series charging Marx circuit, the isolation resistors of each stage only needs to withstand the circuit charging voltage during the pulse forming process, and its isolation capability of pulse is much higher compared with the parallel charging one; however, on the other hand, the isolation resistors of each stage will be connected in series also during the charging process, which means the charging rate of the capacitors at

various stages is quite different and pulse charging rate and the pulse repetition rate will be greatly limited. Typically, as the number of series charging Marx circuit's stage increases, the charging time is proportional to the number of stages, resulting in a significant decrease in the operating efficiency, especially for pulse repetition rate. For example, for Marx circuits using the same value of isolation resistors, the capacitor's charging time of the *n*-stage parallel charging Marx circuit is set as t_{cap}, and the charging time of the *n*-stage series charging Marx circuit (regardless of the power capacity limitation of isolation resistors) should be at least $n \cdot t_{cap}$; if the circuit stage number is increased by *m* times, the capacitor's charging time will be further increased to $n \cdot m \cdot t_{cap}$, which will reduce the theoretical maximum pulse repetition rate by nearly $n \cdot m$ times in terms of circuit performance.

Based on several different types of Marx circuits introduced in the previous research, a ferrite bead & resistor isolated Marx circuit is proposed in this thesis, as shown in Figure 47, which can simultaneously satisfy the optimize requirements to high pulse amplitude and high pulse repetition rate in solid-state sub-nanosecond pulse generator.

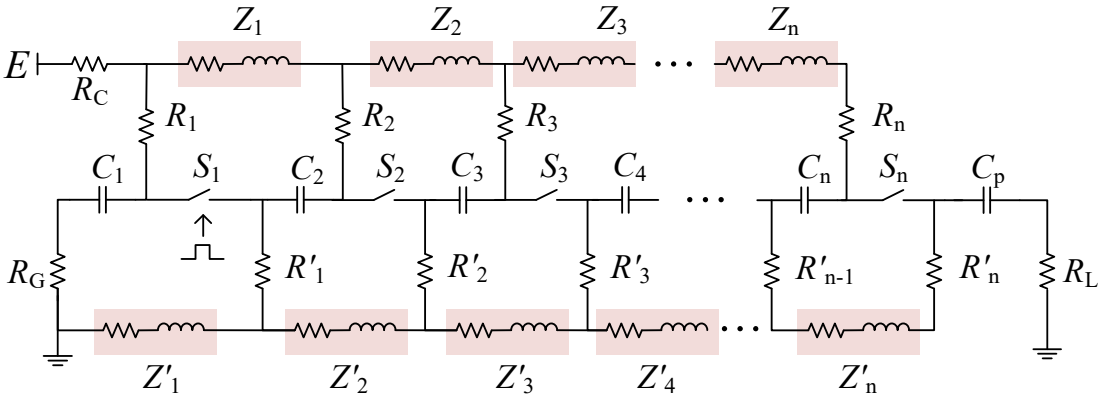

Figure 47. Ferrite bead & resistor isolated Marx circuit.

In this Marx circuit, the isolation circuit is designed by combining parallel resistors with series ferrite beads. The circuit has the advantage of the fast charging rate similar to the parallel charging Marx circuit. At the same time, the pulse isolation capability can be improved by introducing series connected ferrite beads, which avoids the isolation resistor from withstanding the full pulse voltage. The working process of the circuit can be described as follows: During the charging process of the Marx circuit, the equivalent impedance value of the magnetic beads at low frequencies is quite small and negligible. Therefore, the charging rate is basically the same as the parallel charging Marx circuit under the same isolation resistors. The only limitation is that the maximum current of

ferrite bead should less than the maximum charging current. In the pulse forming process of the Marx circuit, the isolation resistors and the ferrite beads are both used for sub-nanosecond pulse isolation, so that this novel isolation circuit can more effectively isolate high amplitude pulses, and can also alleviate possible insulation problems with multiple devices withstanding pulse voltage together.

This Marx circuit is compatible with the main advantages of isolation ferrite beads and isolation resistors for sub-nanosecond pulse isolation, particularly the use of ferrite bead with special impedance characteristics in different frequency bands. At the same time, the advantages of parallel charging Marx circuit and series charging Marx circuit are also integrated and utilized for higher pulse repetition rate. In addition, the drawbacks of some traditional Marx circuit are also avoided. For example, the charging current of each branch is more uniform because the isolation resistance is retained, and the ferrite bead also avoids the possibility of resonance in the underdamped condition. This circuit is especially suitable for Marx circuits with a large number of stages (typically more than 50 stages), because the increase of circuit stages does not significantly limit the circuit charging speed in terms of circuit performance. On the other hand, since this type of Marx circuits can be regarded as traveling-wave Marx circuit in the pulse forming process, which has been analyzed in the previous chapter, the large number of circuit stage will not cause a significant decrease in output efficiency.

4.1.2 Design of paralleled transistors with “transistor-capacitor unit”

The parallel connection of the avalanche transistors can effectively improve the peak current value of the combined switch unit, and is convenient for improving the pulse amplitude or other parameters in the Marx circuit design. In the parallel design of the transistors, the key technique to the circuit design is to achieve uniform current distribution among paralleled transistors, which is called the sharing-current design of the parallel transistors. In the power electronic switch module, the sharing-current control and compensation methods are commonly used for paralleled switches design. However, in the sub-nanosecond pulse source, the pulse rise time and duration time are both extremely short, and the circuit structure is quite sensitive to the variation of the distribution parameters. It is difficult to achieve uniform pulsed current distribution among the paralleled transistors. Therefore, the sharing-current design requires analysis and optimization of the PCB structure of paralleled transistors.

In this thesis, the design of three paralleled transistors is taken as an example to introduce the sharing-current design of the combined switch unit. The typical PCB structure of Marx circuit with three paralleled transistors is shown in Figure 48 (only the central part of the Marx circuit is plotted). According to this PCB structure, SMD components such as resistor *R*, capacitor *C* and transistors *T* are installed accordingly, and there are three transistors in parallel at each stage for large peak current. In order to install the three transistors in line, the length of the metallic pads should be increased and the transistors should be closely arranged as a combined switch unit.

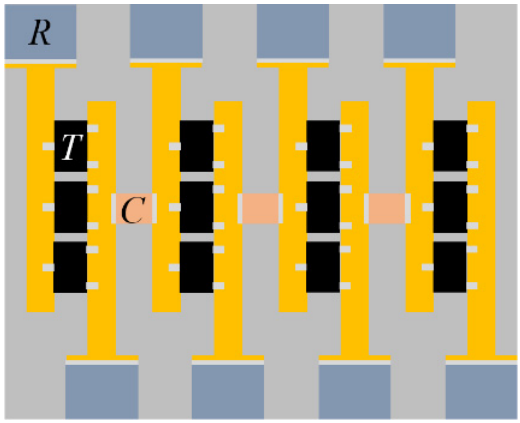

Figure 48. Typical PCB structure of Marx circuit with three transistors connected in parallel.

However, if this circuit structure is used in the practical circuit with a large number of circuit stages, the Marx circuit may generate higher amplitude pulses, but its stability is poor and some transistors is prone to damage, especially the central transistor. In order to analyze this phenomenon, the corresponding circuit model is established in CST to analyze the pulsed current distribution on circuit surface during the pulse forming process. In the modeling process, considering the working characteristics of circuit devices, the transistors and the capacitors are equivalent to the metallic pads with the same packaging, and the isolation resistors are equivalent to an open circuit due to the large resistance value. The circuit model with similar PCB structure is shown in Figure 49, where polytetrafluoroethylene is used as the material of dielectric medium and the metallic pads are made of the perfect electric conductor.

In the simulation process, in order to simulate the traveling-wave propagation of the sub-nanosecond pulse in the pulse forming process, the discrete ports are respectively added at the left side and the right side. The discrete port at the left side is used to inject a sub-nanosecond pulse with the characteristic impedance of 50 Ω. After the pulse transmitting

through the PCB, it reaches the load port at the right side, and a 50 Ω matching resistor is connected for impedance matching. In this simulation, the injection pulse is set to a normalized Gaussian pulse (0-3.5 GHz) to simulate the sub-nanosecond pulse generated Marx circuit. When the peak point of the Gaussian pulse transmitting to the paralleled transistors in the central circuit, the current density distribution on the circuit surface is shown in Figure 50.

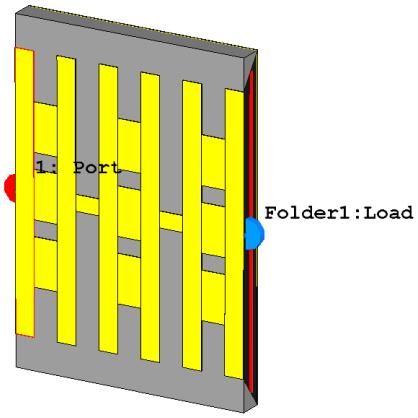

Figure 49. Circuit model of typical PCB structure with three paralleled transistors.

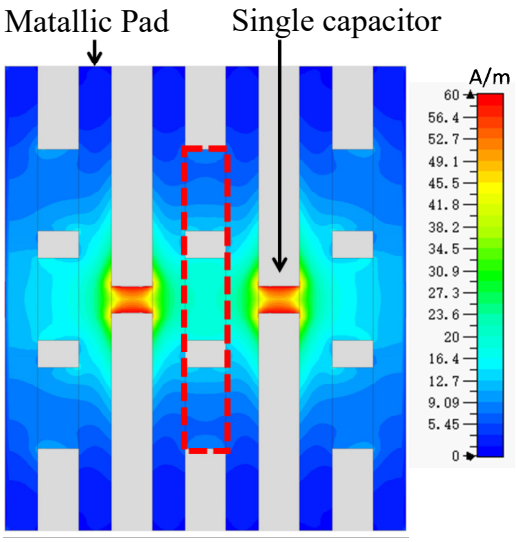

Figure 50. Surface current density distribution on the circuit model of typical PCB structure.

The simulation results show that, since the package size of each capacitors is much smaller than the package size of the parallel transistors, the PCB structure of pulsed current path is similar to the stepped impedance structure in the microstrip low-pass filter (i.e. high-impedance microstrip line is connected to the low-impedance microstrip line directly, and vice versa). Since the path length between the capacitor and each paralleled transistor is significantly different, the current density distribution is uneven among the paralleled

transistors. Specifically, for the three transistors in parallel, the current density of the central transistor is around 15 to 20 A/m, while the current density of the paralleled transistors on both sides is only 5 to 12 A/m. It is obvious that the central transistor gets a larger current density than the transistors on both sides, which explains the fact that the central transistor is prone to damage in the experimental test.

To solve this problem, this thesis proposes a design method of "transistor-capacitor unit" to meet the sharing-current requirements of the paralleled transistors, as shown in Figure 51. Compared with the previous PCB structure of Marx circuit, the capacitor in each stage is adjusted from a single capacitor to three capacitors in parallel, which means the capacitor and the transistor are connected one-to-one in the PCB structure to form the so called "transistor-capacitor unit". In this circuit, the current after passing through the paralleled transistors no longer has to flow though the central capacitor, and the parallel connection of multiple capacitors effectively expands the transmitting path of the pulsed current. At the same time, the design also alleviates the impedance mismatch problem in the pulse forming path by adjusting the circuit configuration.

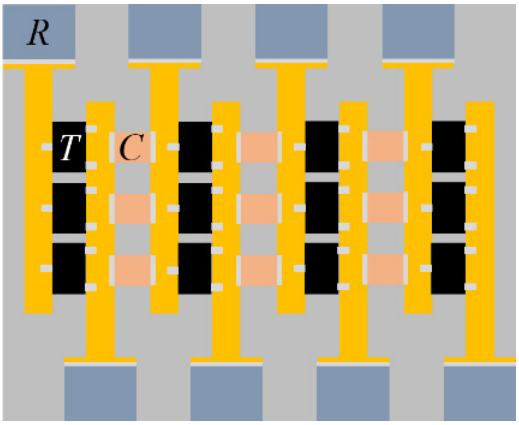

Figure 51. PCB structure of Marx circuit with paralleled "transistor-capacitor unit".

In order to analyze the effectiveness of this design, the current density distribution on the circuit surface is simulated. Figure 52 shows the modified circuit model of the circuit with paralleled "transistor-capacitor unit" in each stage. Specifically, paralleled capacitors are added by adding more metallic pads with the same package size.

By using the same simulation method, the surface current density distribution of the novel circuit model can be obtained, as shown in Figure 53. The simulation results show that the "transistor-capacitor unit" can effectively improve the uniformity of current distribution. Specifically, for the three transistors connected in parallel, their current density is about 10

A/m, which means that the sharing-current design of the transistors meets the ideal design object. Therefore, it can be considered that this design can significantly improve the peak current value of combined switch unit after the parallel connection of transistors, and will improve the working life of the pulse generator by avoiding the failure of transistors due to overcurrent damage.

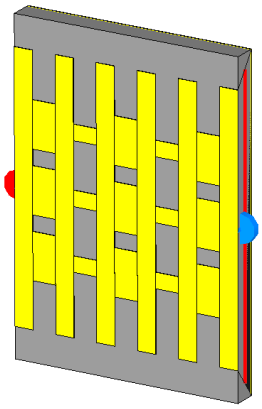

Figure 52. Circuit model of PCB structure with paralleled “transistor-capacitor unit”.

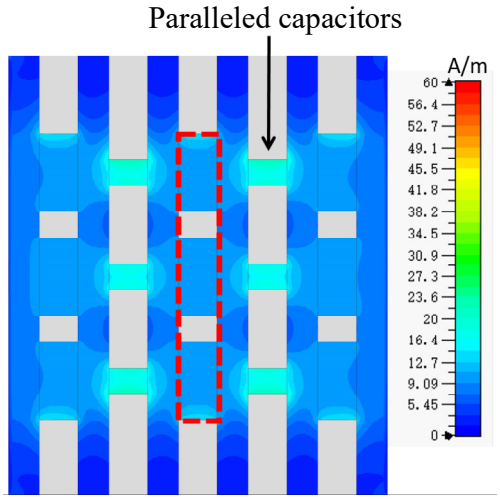

Figure 53. Surface current density distribution on the circuit model with paralleled “transistor-capacitor unit”.

4.1.3 Development of high-amplitude sub-nanosecond pulse generator prototype

To generate sub-nanosecond pulses with a higher amplitude, a 100-stage Marx circuit is developed with the stage number of 100 and the parallel connection of transistors. As the stage number increases, the number of parallelel transistors increases from one to three with a total of 200 transistors in use, as shown in Figure 54. The parallel connection of transistors could increase the peak current for pulse forming and the power capacity for repetitive pulse generation.

If the trigger signal width is much larger than the output pulse width, the triggered transistor T_1 will overheat preferentially in the generation of high-repetition-rate pulse. To generate trigger signals with the pulse width of several nanoseconds, a trigger signal shaping circuit consisting of two step recovery diodes (SRD) and a transmission line transformer TLT_1 (for signal mode conversion) is adopted, as shown in the left part of Figure 54. In this circuit, the square-wave signal is converted into a pulse signal with the sub-nanosecond rise time and pulse width of 1 ns.

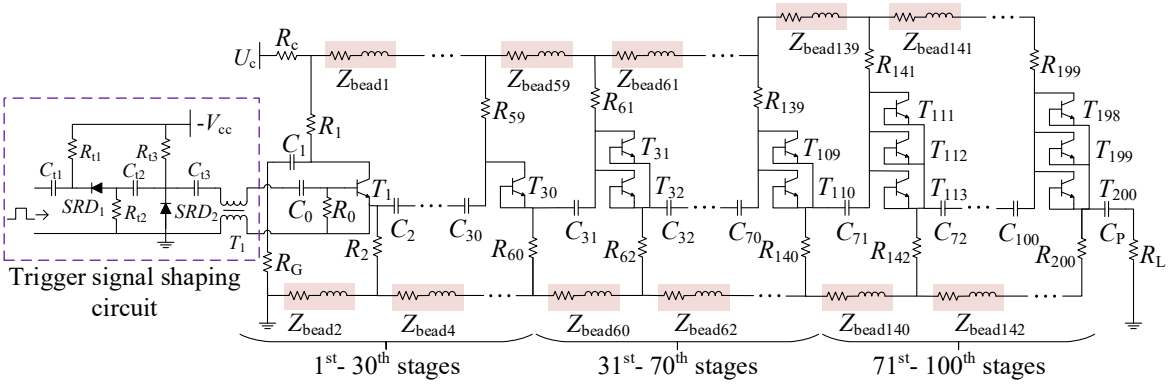

Figure 54. 100-stage Marx circuit and its trigger signal shaping circuit.

The photo of the fabricated 100-stage Marx circuit is shown in Figure 55. At each stage of the Marx circuit, the charging capacitor is 100 pF, the isolation resistor is 10 kΩ, and the equivalent resistance of the ferrite bead is greater than 1 kΩ. In order to improve the peak current of the combined switch and also save the cost of fabrication, according to the variation law of the pulse wave in the pulse forming process, the paralleled number of transistors at the 1st to 30th, 31st to 70th, and 71st to 100th stages of the Marx circuit is set as 1, 2 and 3, respectively. As for the design of PCB structure, the paralleled transistors adopts the sharing-current design with paralleled “transistor-capacitor unit”. When the pulse repetition rate reaches 10 kHz or more, it is necessary to install heat sinks and a forced air cooling system on the circuit to improve the heat dissipation capability of the pulse generator for stable operation.

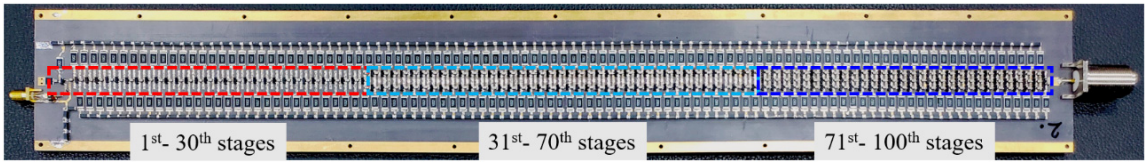

Figure 55. Photo of the 100-stage transistor-based Marx circuit.

The output pulse are measured by a 4 GHz sampling oscilloscope (Lecroy 640 Zi) via a 0-6 GHz/50 Ω attenuator, as shown in Figure 56.

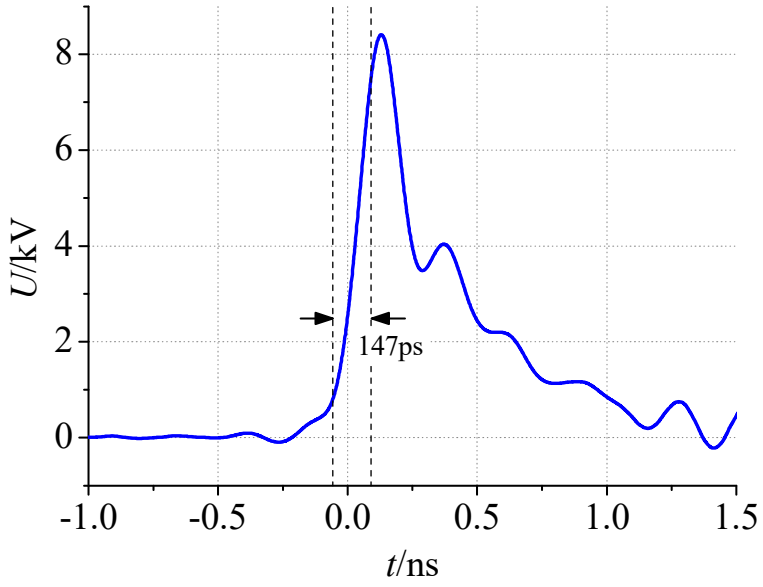

(a)

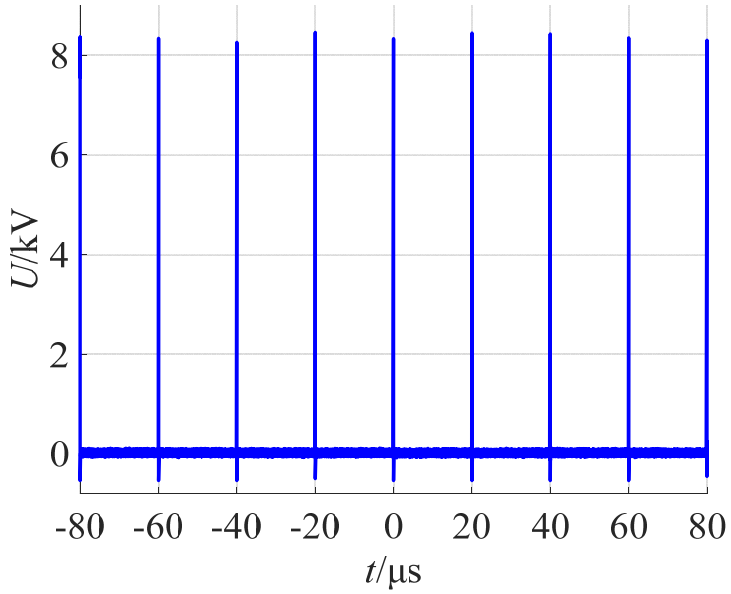

(b)

Figure 56. Measured output waveforms of the fabricated pulser. (a) Waveform of the single pulse. (b) Waveform of the pulses with 50 kHz repetition rate.

The pulse amplitude is 8.5 kV and the rise time (10% to 90% of pulse amplitude) is less than 150 ps with the load of 50 Ω. Therefore, the peak power of the generator is about 1.4 MW. The prototype of the pulser could operate at the repetitive rate of 5 kHz in the stable mode and 50 kHz in the burst mode (within 1 minute) with the installation of a forced air

cooling system. In the testing process, when the pulse repetition rate is increased to 50 kHz, the overheating of the transistors and the resistors on PCB are quite significant according to the infrared thermal image, and the highest temperature is about 45 ℃ near the output terminal, as shown in Figure 57.

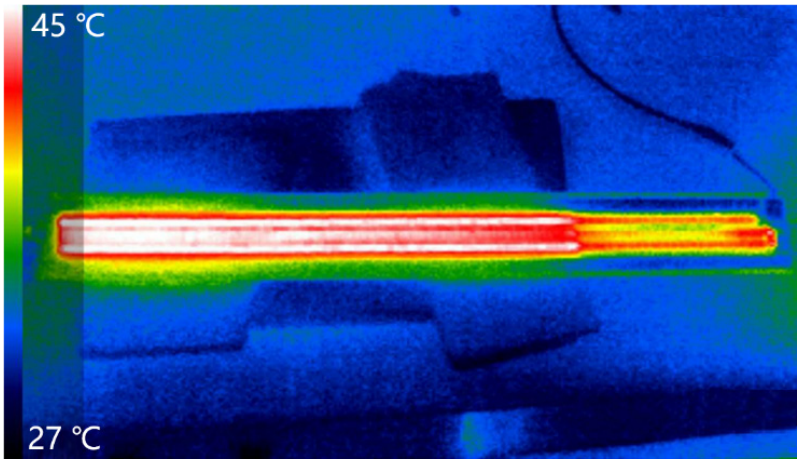

Figure 57. Measured infrared thermal image of the PCB of the 100-stage Marx circuit when the pulse repetition rate is 50 kHz.

4.2 Design of the UWB Radiating Antenna and its Array

4.2.1 Design of combined antenna

The design of UWB radiating antenna is a key technology in UWB electromagnetic radiation research, which can directionally radiate high power UWB electromagnetic pulses with the excitation of sub-nanosecond pulse generator. As for UWB radiating antennas, the combined antenna, proposed by V.I. Koshelev et al.[62, 63], is a popular design for high power UWB electromagnetic pulse radiation, especially for the realization of antenna arrays. Due to the characteristics of wide band, compact structure and high mechanical strength, the combined antenna has been widely studied and applied in recent years.

The structure diagram of a typical combined antenna is shown in Figure 58. Based on the transverse electromagnetic (TEM) horn antenna, the magnetic dipole is introduced with the short circuit at the terminal in the combined antenna, which makes up the weak low frequency radiation ability of traditional TEM horn antenna. Specifically, the combined antenna consists of a TEM horn (1 in Figure 58), an active magnetic dipole (2 in Figure 58) and two passive magnetic dipoles (3 in Figure 58). At low frequency, the active magnetic

dipole is combined with the electric dipole formed by TEM horn. By adjusting the size of the active magnetic dipole, the active magnetic dipole and the electric dipole can be used to offset the reactive power in near field, which can improve the low frequency radiation performance of the antenna and reduce its lower cut-off frequency. When the antenna is operating at high frequency, the radiation capability of TEM horn is significantly enhanced while that of magnetic dipole is weakened. At this time, the radiation characteristics of combined antenna are basically the same as that of TEM horn antenna with the same structure.

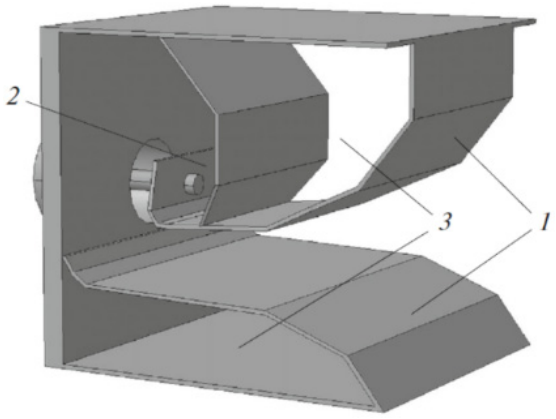

Figure 58. Diagram of a typical combined antenna[63].

In recent years, the optimization design of combined antenna and its arrays has been studied. The design of the combined antenna mainly includes antenna length, antenna aperture size, impedance transition structure, and etc. The length of the antenna is mainly related to the low-frequency characteristics of the antenna. The longer the antenna length, the lower the lower cut-off frequency. The aperture size of the antenna determines the impedance value at the antenna aperture and the radiation performance. Generally, the larger the antenna aperture area, the stronger the antenna radiation efficiency and the better the low frequency performance. The impedance transition structure of TEM horn of antenna is the key point of design. Its geometric structure and terminal impedance directly affect the broadband radiation characteristics of antenna. At present, the commonly used impedance gradient designs include exponential, multistage and Klopfenstein taper[64]. In practical design, the size of antenna aperture and impedance transition structure need to be optimized to meet different design needs.

During the design process of the combined antenna, the radiation characteristics of the antenna can be evaluated by simulating and testing the voltage standing wave ratio,

radiation pattern and radiation field intensity along the radiation direction. The voltage standing wave ratio of the antenna can be used to analyze the impedance matching characteristics of the UWB antenna in wide band and to obtain its working frequency band. Since the combined antenna is mainly used for directional radiation pulse, the radiation pattern is helpful to analyze the directivity of the antenna. The radiation field measurement in the radiation direction is the most commonly used test method. By measuring the waveform of radiating electric field in time domain, the overall performance of the UWB electromagnetic radiator can be evaluated, including far-field effective potential, antenna gain in the radiation direction and the band width of radiating pulse, etc.

4.2.2 Design of combined antenna array

In order to develop a compact UWB electromagnetic radiator with better radiation performance, it is necessary to optimize the antenna structure within the limited antenna aperture area. Therefore, it is necessary to adopt antenna array design. The working principle of antenna array and its design key points are briefly introduced as follows.

With the increase of the aperture area of single combined antenna, its antenna gain will also increase. However, due to the uneven distribution of the radiation field at antenna aperture and the mismatch between the antenna and the pulse generator, the antenna gain of single antenna with too large aperture area increases slowly. However, when the single antenna is replaced by the antenna array with the same aperture area, its far-field effective potential and antenna gain can be further increased by improving the radiation field distribution at antenna aperture, optimizing the antenna size and matching of equivalent impedance. For example, Figure 59 shows several common configurations of four-element antenna arrays, namely horizontal horizontal, vertical linear, and 2×2 rectangular arrays.

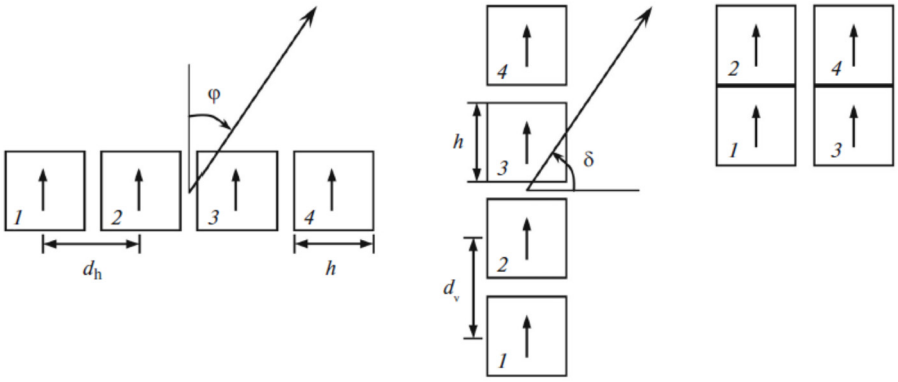

Figure 59. Common configurations of four-element antenna arrays, including horizontal horizontal, vertical linear, and 2×2 rectangular arrays[63].

Taking a 2×2 rectangular antenna array as an example[65], the schematic diagram of the UWB electromagnetic radiator with combined antenna array and feeding module is shown in Figure 60. In this schematic diagram, the 4-element antenna array consists of four combined antennas with same aperture area, which are arranged in a rectangular condiguration according to 2×2 matrix structure. In order to match the output terminal of the pulse generator with the antenna array, the feeding module is composed of a 50/12.5 Ω impedance transformer and a 1:4 power divider, which can simultaneously feed four antennas with sub-nanosecond pulse.

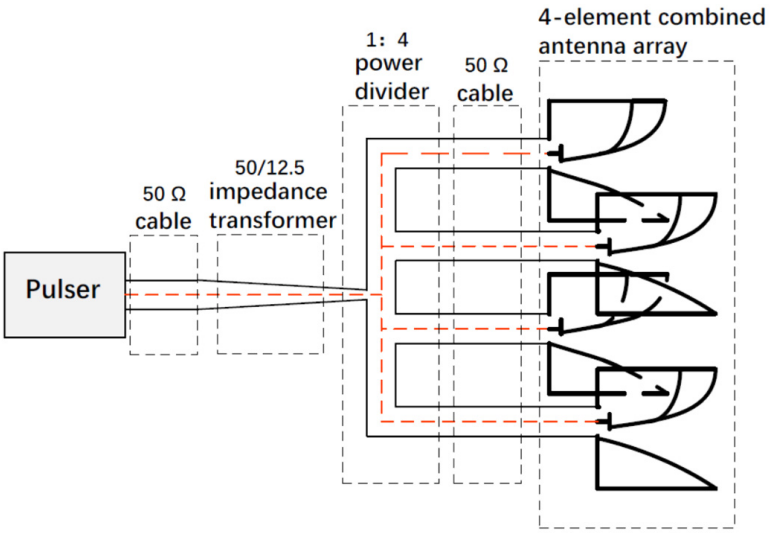

Figure 60. Schematic diagram of the UWB electromagnetic radiator with combined antenna array and feeding module[65].

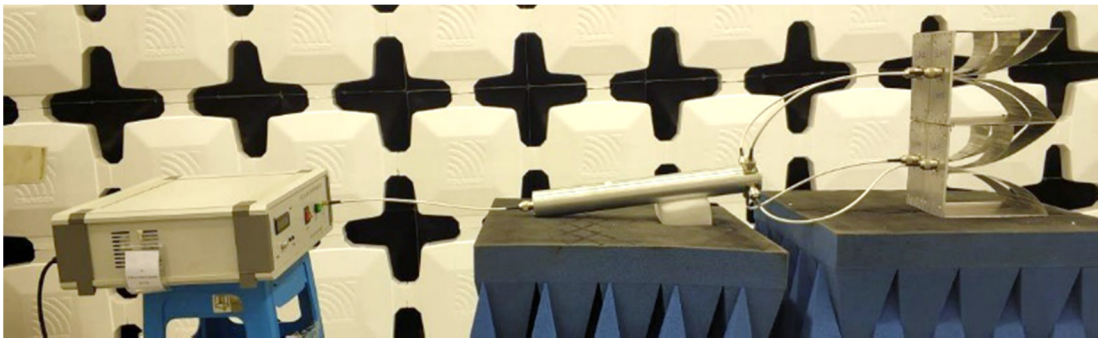

Figure 61. Photo of the UWB electromagnetic radiator with combined antenna array and feeding module[65].

In order to meet the requirements of insulation and broadband characteristics of UWB electromagnetic radiator, the impedance transformer usually adopts coaxial transmission line structure with Klopfenstein taper for impedance transition. The specific design parameters of the impedance transformer need to be calculated and simulated according to the excitation pulse waveform and the working bandwidth of antenna array. The length of

the impedance transformer is approximately proportional to the corresponding wavelength to the lower cut-off frequency of combined antenna. After the impedance transformer, the output terminal with the impedance of 12.5 Ω can be transformed into a symmetric structure with four 50 Ω impedance ports connected in parallel, which acts as a four-port wideband power divider. Figure 61 shows a typical design of the UWB electromagnetic radiator with combined antenna array and feeding module.

In order to satisfy the broadband characteristics, the antenna array design needs to focus on the matching design between the modules, i.e. pulse generator, feeding module, and antenna array. When the excitation pulse waveform is known, the working band of each module should be determined according to the spectrum of pulse waveform to obtain the best radiation performance.

In addition, in the design of antenna array, it is necessary to balance the relationship between the radiation field distribution at antenna aperture and the antenna gain of single antenna. On the one hand, more antenna elements could improve the uniformity of the radiation field distribution in order to get higher effective potential at far field; on the other hand, for the limited aperture area, more antenna elements mean that the aperture area of single antenna is reduced, so the radiation performance of a single antenna should be revalued at the same time. Besides, in order to further improve the radiation performance of the antenna array, the design of the antenna array structure, including the antenna configuration, the antenna spacing, the aperture size of a single antenna, and etc., needs to be further studied and modified according to the specific needs of radiator design.

4.3 Development of the Portable UWB Electromagnetic Radiator Prototype

Combined with the design method of solid-state sub-nanosecond pulse generator and combined antenna array introduced in this chapter, UWB electromagnetic radiators with different parameters can be developed. In this section, a portable UWB electromagnetic radiator will be taken as an example to introduce the specific manufacturing and performance testing process of the radiator.

As shown in Figure 62, a portable UWB electromagnetic radiator is developed based on a high-amplitude sub-nanosecond pulse generator with the peak power of 1.4 MW, the rise time less than 150 ps, and the pulse repetition rate of 50 kHz. A 4-element compact

combined antenna array is used as the UWB radiating antenna. Unlike the common square aperture structure, the width of the antenna aperture area is compressed to achieve higher radiation performance under the unit aperture area. The operating band (voltage standing wave ratio<2) of the single antenna is 383 MHz to 5.72 GHz measured with a 0.01-24 GHz vector network analyzer (Rohde & Schwarz ZVA 24). In addition, a feeding module is adopted between the pulse generator and the antenna array. This module consists of a coaxial impedance transformer and a power divider for impedance conversion and pulse shunting. The working band (S11<-10 dB) of the feeding module is 350 MHz to 5.3 GHz, which is similar to the operating band of the radiating antenna.

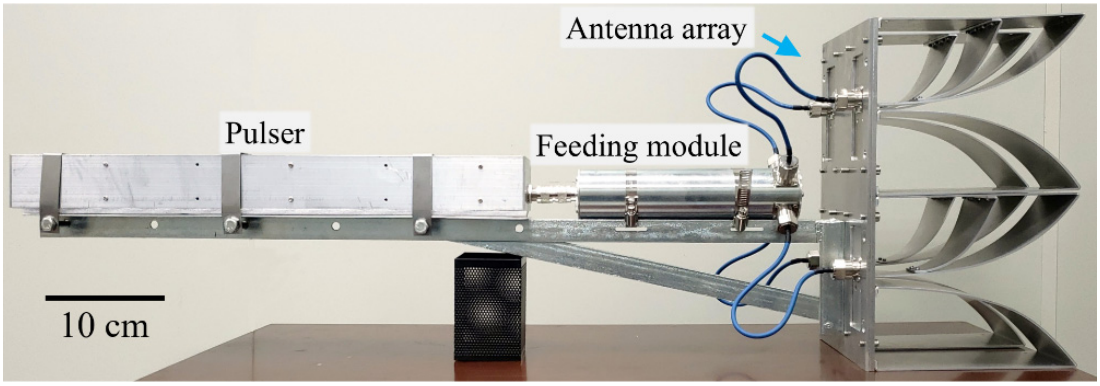

(a)

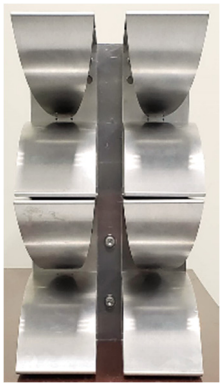

(b)

Figure 62. (a) Photo of UWB radiator consisting of a high-repetition-rate megawatt pulse generator, a compact combined antenna array and a feeding module. (b) Photo of the combined antenna array.

The radiation electric field of the portable UWB electromagnetic radiator prototype can be tested in the EMC chamber. The configuration of the measurement system is shown in Figure 63. The UWB electric field probe is located on the axis of main radiation direction, and its measurement signal is transmitted to the shielding cabinet through high frequency

cables. In the shielding cabinet, a 4 GHz sampling oscilloscope Lecroy 640 Zi and 0-6 GHz/50 Ω attenuator are used to measure the waveform of radiation electric field.

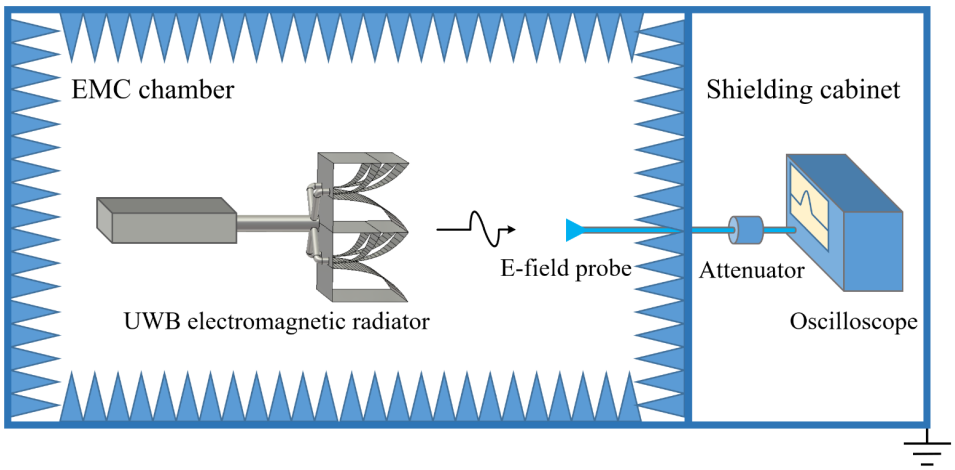

Figure 63. Configuration of the UWB electric field measurement system.

Finally, the radiation electric field is recorded by means of a TEM horn mounted at a 6 m distance in the pattern maximum direction, as shown in Figure 64, and the effective potential rE_p of the radiation system is 10.5 kV. The normalized spectrum of the radiation field is shown in Figure 64 (b), whose -10 dB band range is from 173 MHz to 2.32 GHz. Moreover, the operating mode of the UWB electromagnetic radiator can be set to either the single pulse or the repetitive pulse mode with the repetition rate up to 50 kHz. In the future, a high power radiation system could be assembled by adopting the array design of the UWB radiator.

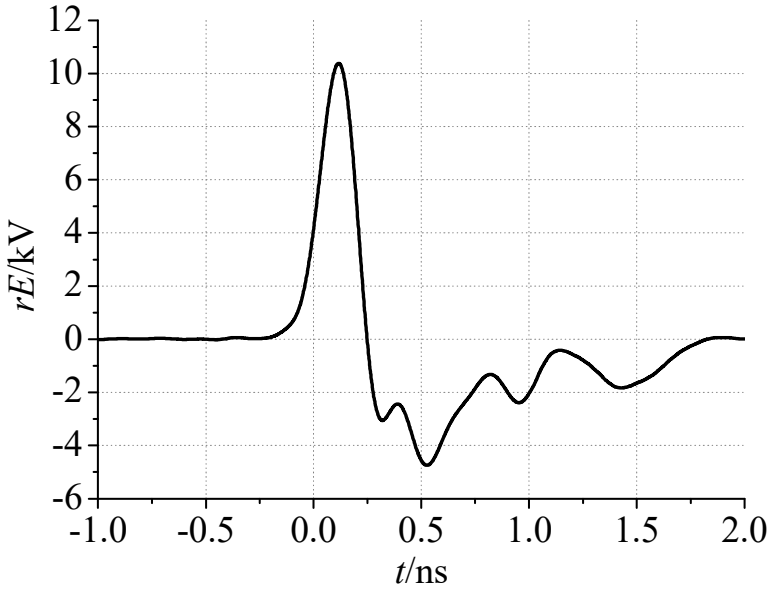

(a)

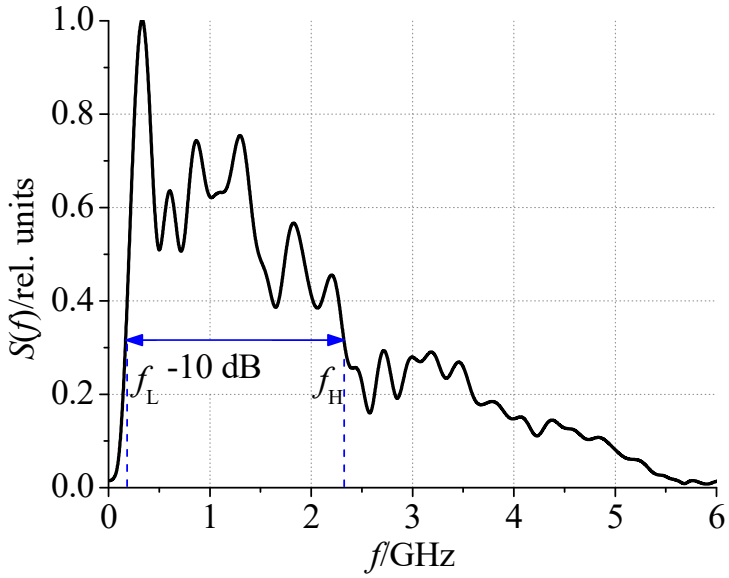

(b)

Figure 64. (a) Measured waveform of the radiation electric field, shown as the effective potential rE_p. (b) Spectrum of the measured radiation field with -10 dB bandwidth.

5 EXPERIMENTAL STUDY ON EMI EFFECTS CAUSED BY REPETITIVE UWB RADIATION

This chapter introduces the experimental study on the EMI effects caused by repetitive UWB radiation, in which a wireless communication system operating at 915 MHz is used as the EUT. In order to study the effect of pulse repetition rate on the communication process, EMI experiments are carried out under the condition of fixed radiation time and fixed pulse number.

5.1 Experimental Design on EMI Effects Caused by Repetitive UWB Radiation

UWB electromagnetic radiation environment can cause EMI effects in various communication systems, which has become an important threat to electronic communication systems. Compared with the wire communication system, the main characteristics of the wireless communication system are that the transmitted signal needs to be modulated at the transmitter and radiated as electromagnetic wave in free space, and the transmitted signal is received at the receiver for demodulation. Although the communication channel is directly exposed to the external free space, the reliability and anti EMI ability of the communication system can be effectively improved by using modulation, filtering, error correction and other technologies. However, UWB electromagnetic radiation environment may defeat the protection of wireless communication system, resulting in multilevel EMI effects or even damage effects on the system[66-69]. On the one hand, due to the wide bandwidth characteristic of UWB electromagnetic radiation environment, its spectrum can often cover different wireless communication frequencies, which means it can effectively avoid the limitations of filtering and other technologies to intrude into the communication system. On the other hand, the energy accumulation effect caused by high peak power or high pulse repetition rate may lead to saturation effect at the receiver or even the damage of the hardware

equipment of the wireless communication system, resulting in more prominent EMI effects [120-124].

In order to study the characteristics of the EMI effect caused by repetitive UWB electromagnetic radiation, especially the influence of pulse repetition rate, this thesis designs experiments with the developed portable UWB electromagnetic radiator, and the EMI effects on wireless communication system is studied qualitatively with different pulse repetition rate.

5.1.1 Design of the experimental setup

Considering the band range of the radiation field produced by the radiator and the communication frequency of commonly used wireless communication system, in order to obtain obvious EMI effects, a wireless communication system with the working frequency band of 900-925.5 MHz is established by using the wireless transceiver chip Si4464. The communication system is mainly composed of transmitter and receiver, including the wireless transceiver chip and its supporting peripheral circuit. The fabricated circuit is enclosed in a metal shielding box and can communicate wirelessly with the other terminal via a narrow band rod antenna. In order to monitor and process the communication signals in real time, besides setting the known transmitting signal and storing the receiving data, an additional photoelectric isolation module is installed at the receiver circuit, which is used to send the received signal to the logic analyzer to obtain the receiving data sequence. Through this method, it is convenient to analyze and classify different EMI phenomena according to the change of the receiving data compared with the transmitting signal data.

As shown in Figure 65, the whole experimental setup including the portable UWB electromagnetic radiator is built in the EMC chamber. The transmitter and receiver of the wireless communication system are located at the right rear side and the front of the UWB electromagnetic radiator, respectively, to simulate the UWB electromagnetic radiation to the wireless communication process. The transmitter is located at the right rear side of the main radiation direction of the radiator, which can effectively avoid the influence of UWB electromagnetic radiation. In the experiment, the wireless communication system should be able to conduct normal and stable communication without electromagnetic radiation.

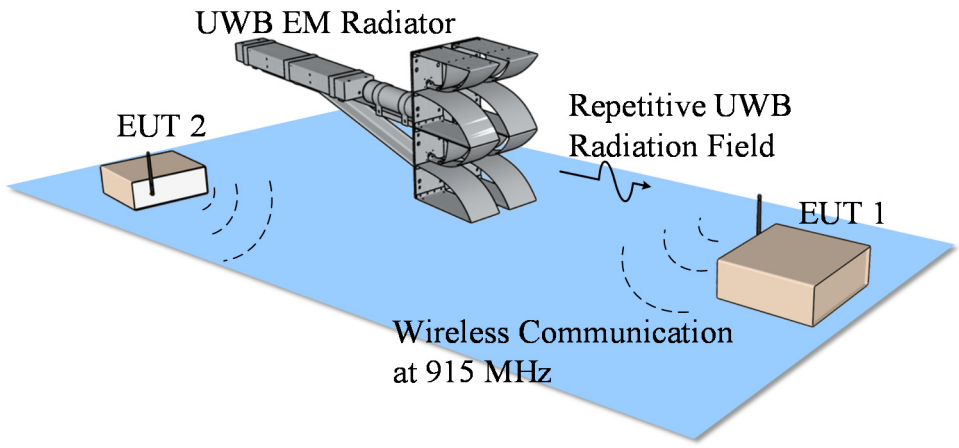

Figure 65. Schematic diagram of experimental setup including the portable UWB electromagnetic radiator.

5.1.2 Design of the experimental procedure

In order to analyze the influence of pulse repetition rate on EMI effects, especially the potential energy accumulation effect and the optimal pulse repetition rate with best utilization of pulse energy, the design of experiments should avoid the EMI effect results being affected by other possible factors. In this guidance of experimental design, the design of two experimental procedures will be briefly introduced as follows.

5.1.2.1 Experimental design on EMI effects with fixed radiation time

In order to study the energy accumulation effect of high repetition rate pulses, it is necessary to design experiments on EMI effects of wireless communication system at different pulse repetition rates. Since the wireless communication rate usually remains the same, it is necessary to fix the radiation time while changing the pulse repetition rate of UWB electromagnetic radiation, so the total number of electromagnetic pulses in the corresponding radiation time is proportional to the pulse repetition rate.

Specifically, in the experimental process, the communication rate is 19200 bps and the total length of communication data is 10k Byte. Since the data transmission time is about 10 seconds, it is necessary to ensure that the UWB electromagnetic radiator can continuously generate the UWB electromagnetic pulses at different pulse repetition frequencies. In the experimental setup, a high-repetition-rate UWB electromagnetic radiator is used to generate UWB electromagnetic pulse with repetition rate up to 600 kHz, and the frequency band of single pulse is about 200 MHz-1.9 GHz. The receiver is located at about 0.5 m from the antenna aperture of the radiator, and the peak electric field is about 3 kV/m at this point. In the experiment, the pulse repetition rate of the radiator increases

gradually from 5 kHz to 250 kHz, and each experiment is repeated three times at the same pulse repetition rate. The common EMI effect in this experiment is the data missing in the received data, that is, some short-term communication interruptions or errors caused by EMI results may be found in the received data sequence. By calculating the length of the received data compared to the total communication data, the percentage of the received data can be obtained to evaluate the level of EMI effects. According to the results of three repeated experiments, the average and standard deviation of the received data can also be calculated.

5.1.2.2 Experimental design on EMI effects with fixed pulse number

Under the condition of limited number of radiation electromagnetic pulses, different pulse repetition rates may produce distinct EMI effects. Under the condition that the same pulse energy is consumed, i.e. the fixed number of radiation pulse, the most significant EMI effect may be obtained at the appropriate pulse repetition rate, which means that the energy utilization rate of the radiation pulse is the highest. In order to analyze the influence of pulse repetition rate on the EMI effects with fixed pulse number, the pulse repetition rate of UWB electromagnetic radiator can be changed while the total pulse number is fixed. In other words, the radiation time of the radiator is inversely proportional to the pulse repetition rate. The higher the pulse repetition rate, the shorter the radiation time of the UWB electromagnetic radiator.

Specifically, in the experimental process, the communication rate is 19200 bps and the total radfiation time is 60 s. In the experimental setup, a portable UWB electromagnetic radiator is used to generate UWB electromagnetic pulse with repetition rate up to 50 kHz, and the effective potential of the radiator is 10.5 kV. The receiver is located at about 2.0 m from the antenna aperture of the radiator, and the peak electric field is about 5 kV/m at the measurement point. In the experiment, the fixed pulse number of the radiator is 200, and the pulse repetition rate can be increased from 10 Hz to 10 kHz. The common EMI effect in this experiment is the data missing in the received data, that is, some short-term communication interruptions or errors caused by EMI results may be found in the received data sequence. By calculating the number of missing data and interruptions caused by the EMI effects, it can be used to evaluate the level of EMI effects with different pulse repetition rate.

5.2 Experimental Results on EMI Effects Caused by Repetitive UWB Radiation

The experimental platform is set up in EMC chamber as shown in Figure 66, in which the wireless communication system is enclosed in the metal shielding box (including logic analyzer) with the installation of narrow band rod antennas for wireless communication. There are no obvious holes on the box and no connections with the outside via wires or cables. According to the different design of the experiments, the UWB electromagnetic radiator type and the distance between the receiver and the radiator need to be adjusted in the experimental platform. During the experiment, the position and operation state of the communication system should not be changed except for the pulse repetition rate of the radiator. In particular, the trigger circuit used in radiator can control its working mode (including the trigger start time, the repetition rate and the total number of the trigger signal) through computer instructions, which can meet the requirements of precise control of the UWB electromagnetic radiator in experiments. The experimental results of EMI effects on wireless communication system are given below with briefly analysis.

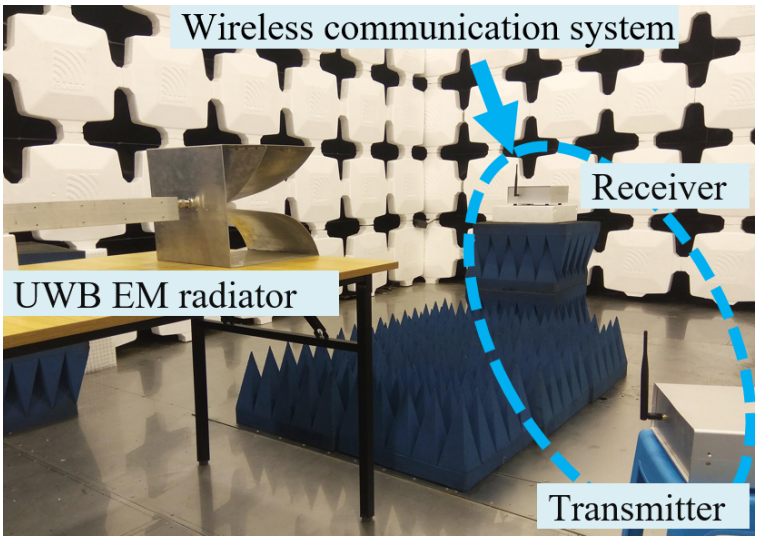

Figure 66. Photo of experimental setup in EMC chamber.

5.2.1 Experimental results of EMI effects with fixed radiation time

According to the corresponding experimental design, the pulse repetition rate of UWB electromagnetic radiator is gradually increased from 5 kHz to 250 kHz, and the experiments are repeated three times at the same repetition rate. The mean value and

standard deviation of the received data percentage under different pulse repetition rate is shown in Figure 67.

The experimental results show that with the increase of pulse repetition rate, the probability of data loss in wireless communication system increases gradually, resulting in a significant reduction in the percentage of received data. At the very beginning, when the pulse repetition rate is 5 kHz, there is almost no EMI effect. It is considered that the probability of communication error or interruption caused by radiation pulse is almost zero due to its limited energy. With the increase of pulse repetition rate to 10 kHz, the probability of EMI effect increases, which shows that the percentage of received data begins to decrease. When the pulse repetition rate reaches 100 kHz, the signal sequence recorded by logic analyzer shows that more and more short-term interruptions are appeared, but the interruption process can be recovered in a short time during the pulse action period, which means that the probability of communication interruption effect is further increased. When the pulse repetition rate reaches 200 kHz, the continuous interruption occurs in the wireless communication system, which means that the receiver cannot receive any valid data.

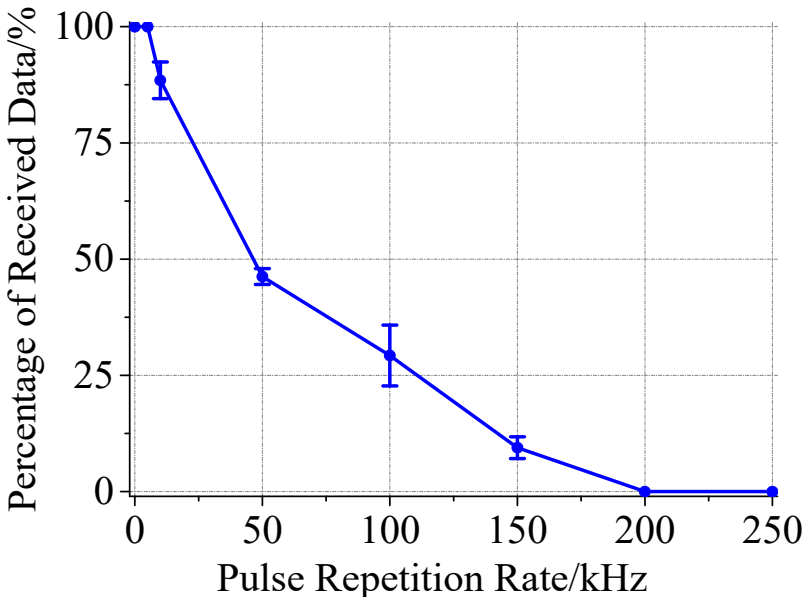

Figure 67. Measured results of EMI effects with fixed radiation time.

In this experiment, with the increase of pulse repetition rate, the increase of radiation pulse number can increase the probability of EMI effect; at the same time, the reduction of the period between pulses may further improve the probability of EMI effect through the process of energy accumulation. As the pulse repetition rate continues to increase, the

short-time communication interruption in the system gradually expands to a continuous long-term interruption, which eventually results as a complete communication breakdown. The experimental results also show that with the increase of pulse repetition rate linearly, the decline rate of percentage of received data slows down. This may be due to the different sensitivity of the wireless communication system to EMI in normal state and in interruption state. When the pulse repetition rate is low, most of the electromagnetic pulses can directly radiate on the receiver in working order, which is more likely to cause communication interruption; when the pulse repetition rate is too high, the receiver tends to be saturated.

5.2.2 Experimental results of EMI effects with fixed pulse number

According to the experimental design of EMI effects with fixed pulse number, the trigger scircuit of UWB electromagnetic radiator is set to the mode of fixed trigger signal, which satisfies the requirement of fixed radiation pulse number. In the experimental process, the pulse repetition rate of UWB electromagnetic radiator is gradually increased from 10 Hz to 10 kHz, and the number of missing data and interruptions under different pulse repetition rate is shown in Figure 68.

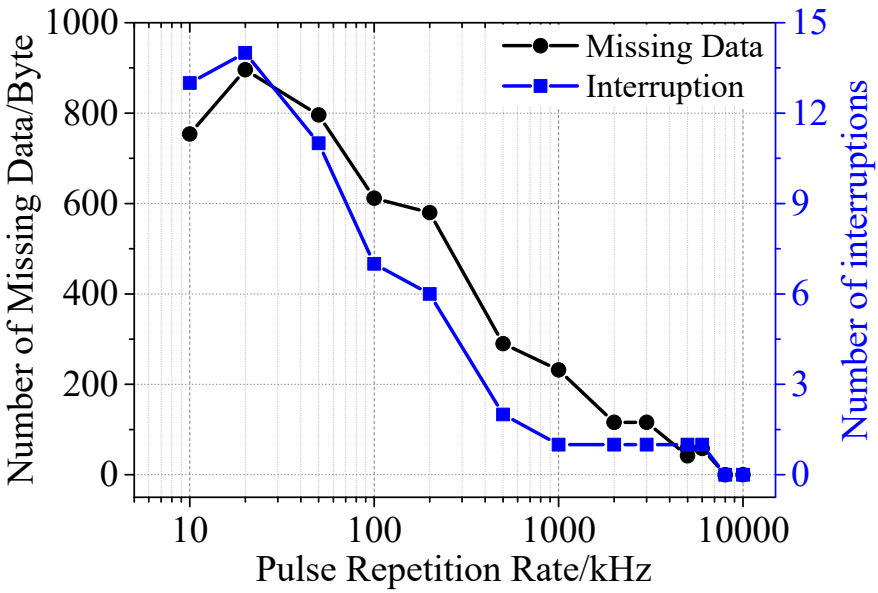

Figure 68. Measured results of EMI effects with fixed pulse number.

In this experiment, the limited number of pulses avoids the concomitant influence caused by the increase of pulse number in previous experiment. When the pulse repetition rate is quite low, it is considered that the EMI effects of each pulse on the communication system

are independent and cannot satisfy the energy accumulation condition, so the probability of the interference effects of the system remains low. With the increase of pulse repetition rate, the cumulative effect of pulse energy generated by repetitive pulses increases the probability of communication error or interruption, and the energy utilization of radiation pulse increases a lot. However, when the pulse repetition rate further increases, the radiation time decreases gradually; the limited radiation time limits the occurrence of EMI effect, and the energy utilization rate of the radiation pulses decreases also. When the pulse repetition rate is very high, the communication process of the system will not be disturbed any more, which may be caused by the limitation of system response speed, saturation of receiver terminal and/or other potential reasons. Although continually increasing the number of pulses is likely to produce the EMI effect again, it is obvious that the overall energy utilization rate remains at a low level. In the practical applications, the pulse repetition rate is often restricted by the pulse source technology and the power supply, so it is necessary to take into account the energy utilization rate of the radiation pulses while meeting the needs of EMI effects.

6 CONCLUSIONS

UWB electromagnetic environment is widely used in the fields of EMC, biological electromagnetics, and etc. Under this background, this thesis mainly focuses on the optimizations of solid-state sub-nanosecond pulse generator, and its pulse repetition rate and pulse amplitude are effectively improved by techniques like modeling of the traveling-wave Marx circuit. Based on this type of pulse generator, a portable UWB electromagnetic radiators is developed, and the preliminary experimental study on EMI effects caused by repetitive UWB electromagnetic pulse radiation is also carried out. In the course of this study, the following conclusions have been obtained.

1. To simulate the traveling-wave phenomenon in the sub-nanosecond pulse generator, the inter-stage transmission lines are introduced into the lumped parameter Marx circuit, which is called the traveling-wave Marx circuit. From the simulation results we can see, the delay time and the impedance matching of the inter-stage transmission lines are the key factors affecting the performance of the traveling-wave Marx circuit. The Marx circuit with different parameters of the inter-stage transmission lines may cause a significant reduction in the pulse amplitude; in order to improve the pulse amplitude, the delay time should be as short as possible and the impedance should be matched with the load. The influence of inter-stage transmission lines on pulse forming process in Marx circuit is analyzed in time domain and frequency domain respectively. Especially, in frequency domain, we find that the PCB structure of Marx circuit is quite similar to that of low-pass microstrip filter. This new perspective can help us understand the low-pass filtering effects of PCB design on the high-frequency components of sub-nanosecod pulse waveform, and help to optimize PCB structure with suitable circuit configuration to improve the output efficiency and parameters of pulse generator.
2. Based on the traveling-wave Marx circuit, several applications are proposed for pulse generator optimization. Different from the parallel circuit modules for power combination, the design of modularized Marx circuits in series connection is proposed where the Marx circuit modules are connected by matched coaxial cables. This design

allows changing pulse amplitude by adjusting the number of circuit modules, as well as a bendable Marx circuit for a compact circuit layout. By using this technique, a compact high-amplitude pulse generator is developed with the amplitude of 8.2 kV, the rise time of 150 ps and the PCB length of 35 cm. For higher pulse repetition rate, the heat dissipation design of PCB is necessary; however, due to the variations in the microstrip line structure, the commonly-used metallic heat sink may cause a significant decrease in pulse amplitude. Thus, a novel heat dissipation design is proposed by optimizing the layout of metallic sinks and introducing heat-conducting ceramic sinks. A high-repetition-rate pulse generator is developed with the maximum pulse repetition rate of 600 kHz, the amplitude of 1.1 kV and the rise time of 160 ps.

3. Based on a solid-state sub-nanosecond pulse generator with the peak power of 1.4 MW, the rise time less than 150 ps, and the repetition rate of 50 kHz, a portable UWB electromagnetic radiator is developed in this thesis. To generate high-amplitude pulses, a 100-stage Marx circuit with parallel connection of multiple transistors is proposed. To solve the problem of uneven current distribution on paralleled transistors, instead of using single capacitor in each stage, we adopt the connection structure with multiple “transistor-capacitor unit” connected in parallel in the PCB structure, which is proved as an effective sharing-current design of the combined switch unit. To improve pulse repetition rate, the parallel charging Marx circuit is adopted with ferrite beads connected in series between stages for high isolation of pulses, which is called the ferrite bead & resistor isolated Marx circuit. In order to radiate UWB electromagnetic pulse directionally, a compact combined antenna array is fabricated and connected with the pulse generator via a coaxial feeding module. The effective potential of the UWB radiator reaches 10.5 kV with the band range (-10 dB) from 173 MHz to 2.32 GHz.
4. By using the developed UWB electromagnetic radiators, the EMI effects caused by repetitive UWB electromagnetic pulse radiation are experimental studied on wireless communication system. The experimental setup includes two UWB electromagnetic radiators with different working parameters, a wireless communication system operating at 915 MHz, and a logic analyzer for communication data recording. Two sets of experiments were designed and carried out to study the influence of pulse repetition rate on EMI effects like data missing and communication interruptions, in which fixed radiation time and total pulse number are set respectively. According to

the experimental results with fixed radiation time and fixed pulse number, we found that the higher pulse repetition rate could cause the energy accumulation effect, which can stimulate the probability of communication interruption effect and other related EMI effects.

BIBLIOGRAPHY

[1] Baum CE. Reminiscences of High-Power Electromagnetics[J]. IEEE Transactions on Electromagnetic Compatibility, 2007,49(2):211-218.

[2] Radasky WA, Baum CE, Wik MW. Introduction to the special issue on high-power electromagnetics (HPEM) and intentional electromagnetic interference (IEMI)[J]. IEEE Transactions on Electromagnetic Compatibility, 2004,46(3):314-321.

[3] Giri DV. High Power Electromagnetic Radiators: Nonlethal Weapons and Other Applications[M]. MA, Cambridge:Harvard Univ. Press, Dec. 2004.

[4] Koshelev VI, Buyanov YI, and Belichenko VP. Ultrawideband Short-Pulse Radio Systems[M]. Artech House, 2017.

[5] Robert J. Recent system applications of short-pulse ultra-wideband (UWB) technology. IEEE Transactions on Microwave Theory and Techniques, vol.52, pp.2087-2104, September 2004.

[6] IEC 2005. Electromagnetic compatibility (EMC) – Part 2-13: Environment – High-power electromagnetic (HPEM) environments – Radiated and conducted[S]. Geneva, Switzerland: International Electrotechnical Commission, 2005.

[7] Radasky WA, Baum CE, Wik MW. Introduction to the special issue on high-power electromagnetics (HPEM) and intentional electromagnetic interference (IEMI)[J]. IEEE Transactions on Electromagnetic Compatibility, 2004, 46(3):314-321.

[8] Savage E, Radasky W. Overview of the threat of IEMI (intentional electromagnetic interference) [J]. Electromagnetic Compatibility (EMC)[C]//IEEE International Symposium on, 2012, 41(11):317-322.

[9] Nitsch D, Camp M, Sabath F, et al. Susceptibility of some electronic equipment to HPEM threats[J]. IEEE Transactions on Electromagnetic Compatibility, 2004, 46 (3):380-389.

[10] Semenov I, Xiao S, Kang D, et al. Cell stimulation and calcium mobilization by picosecond electric pulses[J]. Bioelectrochemistry, 2015, 105: 65-71.

[11] Semenov I, Xiao S, Pakhomov A G. Electroporation by subnanosecond pulses[J]. Biochemistry and biophysics reports, 2016, 6: 253-259.

[12] Xiao S, Guo S, Nesin V, et al. Subnanosecond electric pulses cause membrane permeabilization and cell death[J]. IEEE Transactions on Biomedical Engineering, 2011, 58(5): 1239-1245.

[13] Kotnik T, Frey W, Sack M, et al. Electroporation-based applications in biotechnology[J]. Trends in biotechnology, 2015, 33(8): 480-488.

[14] Camp J T. Synergistic effect of subnanosecond pulsed electric fields and temperature on the viability of biological cells[D]. Norfolk, USA: Old Dominion University,2012.

[15] Hussain MGM. Ultra-wideband impulse radar-an overview of the principles[J]. IEEE Aerospace & Electronic Systems Magazine, 1998, 13(9):9-14.

[16] Buccella C, Feliziani M, Manzi G. Detection and localization of defects in shielded cables by time-domain measurements with UWB pulse injection and clean algorithm postprocessing[J]. IEEE Transactions on Electromagnetic Compatibility, 2004, 46(4): 597-605.

[17] Khaleghi A, Zein GE, Naqvi IH. Demonstration of time-reversal in indoor ultra-wideband communication: Time domain measurement[C]//2007 4th International Symposium on Wireless Communication Systems. IEEE, 2007: 465-468.

[18] Bourqui J, Fear EC. Systems for ultra-wideband microwave sensing and imaging of biological tissues[C]//2013 7th European Conference on Antennas and Propagation (EuCAP), Gothenburg, 2013, pp. 834-835.

[19] Kshetrimayum RS. An introduction to UWB communication systems[J]. IEEE Potentials, vol. 28, no. 2, pp. 9-13, March-April 2009.

[20] Jiang W et al. Compact solid-State switched pulsed power and its applications[J]. Proceedings of the IEEE, vol. 92, no. 7, pp. 1180-1196, July 2004.

[21] Li JT, Zhong X, Cao H, et al. Development of a stereo-symmetrical nanosecond pulsed power generator composed of modularized avalanche transistor Marx circuits[J]. Review of Scientific Instruments, 2015, 86(9): 093502.

[22] Li JT, Zhong X, Li JH, et al. Theoretical Analysis and Experimental Study on an Avalanche Transistor-Based Marx Generator[J]. IEEE Transactions on Plasma Science, 2015, 43(10): 3399-3405.

[23] Li C, Zhang R, Yao C, et al. Development and simulation of a compact picosecond

pulse generator based on avalanche transistorized Marx circuit and microstrip transmission theory[J]. IEEE Transactions on Plasma Science, 2016, 44(10): 1907-1913.

[24] Jethwa J, Marinero EE, Müller A. Nanosecond risetime avalanche transistor circuit for triggering a nitrogen laser[J]. Review of Scientific Instruments, 1981, 52(7): 989-991.

[25] Baker RJ. High voltage pulse generation using current mode second breakdown in a bipolar junction transistor[J]. Review of scientific instruments, 1991, 62(4): 1031-1036.

[26] Rai VN, Shukla M, Khardekar RK. A transistorized Marx bank circuit providing sub-nanosecond high-voltage pulses[J]. Measurement Science and Technology, 1994, 5(4): 447.

[27] Krishnaswamy P, Kuthi A, Vernier PT, et al. Compact subnanosecond pulse generator using avalanche transistors for cell electroperturbation studies[J]. IEEE Transactions on Dielectrics and Electrical Insulation, 2007, 14(4): 873-877.

[28] Liu J, Shan B, Chang Z. High voltage fast ramp pulse generation using avalanche transistor[J]. Review of Scientific Instruments, 1998, 69(8): 3066-3067.

[29] Yuan X, Zhang H, Yang B, et al. 4kV/30kHz short pulse generator based on time-domain power combining[C]//2010 IEEE International Conference on Ultra-Wideband, Nanjing, 2010, pp. 1-4.

[30] Prather WD, Baum CE, Torres RJ, et al. Survey of worldwide high-power wideband capabilities [J]. IEEE Transactions on Electromagnetic Compatibility, 2004, 46(3):335-344.

[31] Burger J W, Baum C E, Prather W D, et al. Design and Development of a High Voltage Coaxial Hydrogen Switch[C]//Ultra-Wideband, Short-Pulse Electromagnetics 6, Springer, Boston, MA, 2003: 381-390.

[32] Giri DV, Lackner H, Smith ID, et al. Design, fabrication, and testing of a paraboloidal reflector antenna and pulser system for impulse-like waveforms[J]. IEEE transactions on plasma science, 1997, 25(2): 318-326.

[33] Baum CE, Baker WL, Prather DW, et al. JOLT: A highly directive, very intensive, impulse-like radiator [R]. Sensor and Simulation Note 480, Nov. 10, 2003.

[34] Baum CE, Baker WL, Prather DW, et al. JOLT: A highly directive, very intensive, impulse-like radiator [J]. Proceedings of the IEEE, 2004,92(7):1096-1109.

[35] Koshelev VI, Gubanov VP, Efremov AM, et al. High-power ultrawideband radiation source with multielement array antenna[C]//13th International Symposium in High Current Electronics. 2004: 258-261.

[36] Gubanov VP, Efremov AM, Koshelev VI, et al. Sources of high-power ultrawideband radiation pulses with a single antenna and a multielement array[J]. Instruments and Experimental Techniques, 2005, 48(3): 312-320.

[37] Koshelev VI, Plisko VV, Sukhushin, KN. Array antenna for directed radiation of high-power ultra-wideband pulses[C]//Ultra-Wideband, Short-Pulse Electromagnetics 9, Springer, New York, 2010: 259-267...

[38] Efremov AM, Koshelev VI, Kovalchuk BM, et al. High power sources of ultra-wideband radiation with sub-nanosecond pulse lengths[J]. Instruments and Experimental Techniques, 2011, 54(1): 70-76.

[39] Efremov AM, Koshelev VI, Kovalchuk BM, et al. Generation and radiation of ultra-wideband electromagnetic pulses with high stability and effective potential[J]. Laser and Particle Beams, 2014, 32(3): 413-418.

[40] Kim AA, Kovalchuk BM, Kokshenev VA, et al. Review of high-power pulsed systems at the Institute of High Current Electronics[J]. Matter and Radiation at Extremes, 2018, 1(4): 201.

[41] Tesche FM, Giri DV, Nyffeler M. Swiss Impulse Radiating Antenna (SWIRA) Characterization in the Presence of a Local Ground Plane (Earth)[R]. Sensor and Simulation Notes, 2011, 557.

[42] Rhebergen J B , Zwamborn A P M , Giri D V . Design of an ultra-wideband ground-penetrating radar system using impulse radiating antennas[C]//International Conference on Detection of Abandoned Land Mines. IET, 1998.

[43] Pécastaing L, De Ferron AS, Couderc V, et al. A Pulsed Modulator Combined With Very High PRF Photoconductive Switches to Build a Self-Scanning UWB Radiation Source[J]. IEEE Transactions on Plasma Science, 2016, 44(10): 1894-1901.

[44] Paul CR. Introduction to Electromagnetic Compatibility, Second Edition[M]. John Wiley & Sons, Inc. 2006:1-12.

[45] Brauer F, Sabath F, Ter Haseborg JL. Susceptibility of IT network systems to interferences by HPEM[C]//2009 IEEE International Symposium on

Electromagnetic Compatibility. IEEE, 2009: 237-242.

[46] Nitsch D, Camp M, Sabath F, et al. Susceptibility of some electronic equipment to HPEM threats[J]. IEEE Transactions on Electromagnetic Compatibility, 2004, 46(3): 380-389.

[47] Camp M, Gerth H, Garbe H, et al. Predicting the breakdown behavior of microcontrollers under EMP/UWB impact using a statistical analysis[J]. IEEE Transactions on Electromagnetic Compatibility, 2004, 46(3): 368-379.

[48] Hower PL, Reddi VGK. Avalanche injection and second breakdown in transistors[J]. IEEE Transactions on Electron Devices, 1970, 17(4): 320-335.

[49] Beatty B, Krishna S, Adler M S. Second breakdown in power transistors due to avalanche injection[C]//1976 IEEE Power Electronics Specialists Conference. IEEE, 1976: 247-254.

[50] Pierret RF. Semiconductor device fundamentals[M]. Pearson Education India, 1996.

[51] Baum CE, Lehr JM. Parallel Charging of Marx Generators for High Pulse Repetition Rates[C]// Ultra-Wideband, Short-Pulse Electromagnetics 5, Springer, US, 2002:415-422.

[52] Bluhm H. Pulsed Power Systems: Principles and Applications[J]. Power Systems, 2006.

[53] Pozar, David M. Microwave engineering[M]. John Wiley & Sons, 2009.

[54] Davis WA, Agarwal K K. Radio frequency circuit design[M]. New York: Wiley, 2001.

[55] Baum C E. Traveling-wave switches and marx generators[C]//Ultra-Wideband, Short Pulse Electromagnetics 9. Springer, New York, NY, 2010: 297-300.

[56] Gao M, Xie Y, Qiu Y, et al. Performance improvement for sub-nanosecond Marx generator based on avalanche transistors by considering the traveling wave process[C]//2018 IEEE International Symposium on Electromagnetic Compatibility and 2018 IEEE Asia-Pacific Symposium on Electromagnetic Compatibility (EMC/APEMC). IEEE, 2018: 925-927.

[57] Spice Model: FMMT415.spice.txt, 2003. [Online]. Available: https://www.diodes.com/spice/download/3337/FMMT415.spice.txt

[58] PSpice Reference Guide, 2nd edition[OL]. Cadence Design Systems, Inc., Portland, OR, USA, 2000, pp. 191-236.

[59] Hong JS, Lancaster MJ. Microstrip filters for RF/microwave applications[M]. New York: Wiley, 2001.

[60] Jiang W, Wang X, Yuan J, et al. Compact pulsed power and its industrial applications[C]//2009 IEEE Pulsed Power Conference. IEEE, 2009: 1-10.

[61] Shabany Y. Heat transfer: thermal management of electronics[M]. CRC press, 2009.

[62] Koshelev V I, Buyanov Y I, Andreev Y A, et al. Ultrawideband radiators of high-power pulses[C]//PPPS-2001 Pulsed Power Plasma Science 2001. 28th IEEE International Conference on Plasma Science and 13th IEEE International Pulsed Power Conference. Digest of Papers (Cat. No. 01CH37251). IEEE, 2001, 2: 1661-1664.

[63] Koshelev VI, Plisko VV. Structure of arrays of ultrawideband combined antennas[J]. Journal of Communications Technology and Electronics, 2017, 62(6): 565-568.

[64] Wang S, Xie Y. Design and optimization of high-power UWB combined antenna based on Klopfenstein impedance taper[J]. IEEE Transactions on Antennas and Propagation, 2017, 65(12): 6960-6967.

[65] Wang S, Xie Y, Gao M, et al. Optimizing High-Power Ultra-Wideband Combined Antennas for Maximum Radiation Within Finite Aperture Area[J]. IEEE Transactions on Antennas and Propagation, 2019, 67(2): 834-842.

[66] Vault WL. The damage susceptibility of integrated circuits to a simulated IEMP transient[J]. 1973,20(6):40-47.

[67] Liu Y, Chai CC, Yang YT, et al. Damage effect and mechanism of the GaAs high electron mobility transistor induced by high power microwave[J]. Chinese Physics B, 2016, 25(4): 048504.

[68] Wang Q, Chai C, Liu Y, et al. The influence of pulsed parameters on the damage of a Darlington transistor[J]. Journal of Semiconductors, 2018, 39(9): 094005.

[69] Zhou L, Chen X, Peng H L, et al. Experiments and comparisons of power to failure for SiGe-based low-noise amplifiers under high-power microwave pulses[J]. IEEE Transactions on Electromagnetic Compatibility, 2018, 60(5): 1427-1435.

PUBLICATIONS

[1] **Gao MX**, Xie YZ, Li Kejie, et al. Traveling-Wave Marx Circuit Model for Generating Repetitive Sub-nanosecond Pulses[J]. IEEE Transactions on Electromagnetic Compatibility, 2019. (Published online)

[2] **Gao MX**, Xie YZ, Wang SF, et al. A portable ultrawideband electromagnetic radiator with a 1.4 MW/50 kHz solid-state subnanosecond pulser[J]. Review of Scientific Instruments, 2019, 90(6): 066102.

[3] Wang SF, Xie YZ, **Gao MX**, et al. Optimizing High-Power Ultra-Wideband Combined Antennas for Maximum Radiation within Finite Aperture Area[J]. IEEE Transaction on Antennas and Propagation, vol. 67, no. 2, pp. 834-842, 2019.

[4] **Gao MX**, Xie YZ, Qiu YX, et al. Performance improvement for sub-nanosecond Marx generator based on avalanche transistors by considering the traveling wave process[C]. 2018 IEEE International Symposium on Electromagnetic Compatibility and 2018 IEEE Asia-Pacific Symposium on Electromagnetic Compatibility. IEEE, 2018:925-927.

[5] **Gao MX**, Xie YZ, Li Q, et al. Calculation of complex permittivity for shielding effectiveness equivalence[C]. 17th IEEE International Conference on Environment and Electrical Engineering and 1st IEEE Industrial and Commercial Power Systems Europe. IEEE, 2017:1-5.

[6] **Gao MX**, Xie YZ, Hu YH. Parameter optimization for rise time of sub-nanosecond pulser based on avalanche transistors[C]. 21st IEEE Workshop on Signal and Power Integrity. IEEE, 2017:1-3.